August Chełkowski Institute of Physics
Faculty of Science and Technology
Doctoral School of the University of Silesia in Katowice

Nuclear fragmentation cross-section measurements and development of new beam detectors for future experiments

Doctoral Thesis by
Marta Urbaniak

dr hab. Seweryn Kowalski, University of Silesia in Katowice, Supervisor

Katowice, Poland
November 27, 2024

Abstract

"Nuclear fragmentation cross-section measurements and development of new beam detectors for future experiments"

This thesis presents the results of the research tasks conducted during the PhD study of the author. The main part of the thesis presents the result of the analysis of measurements of nuclear fragmentation cross-sections conducted by the NA61/SHINE experiment. The second part focuses on the author's involvement in the upgrade of the detector system during the Long Shutdown 2 in the CERN facility.

NA61/SHINE is a fixed-target experiment located in the North Area of the CERN Super Proton Synchrotron (SPS). NA61/SHINE physics program focuses on studying the QCD phase diagram and conducting a series of reference measurements for neutrino and cosmic-ray experiments. Nuclear fragmentation measurements are part of the experiment's cosmic rays program. The aim of the project is to measure the cross-sections for the nuclear fragmentation process of the light and intermediate nuclei. These are essential parameters in modeling the propagation of cosmic rays through the Galaxy. Cross-sections calculated in this work are charge-changing cross-sections for three beam ions: boron, nitrogen, and carbon at a beam momentum of 13.5A GeV/c. Cross-sections were calculated for interaction with two types of target carbon and polyethylene, and from the results, the cross-section for interaction with proton was calculated.

The second part of the thesis focuses on the development of new beam position monitors for the NA61/SHINE experiment. Detectors were developed and tested during Long Shutdown 2. Detectors are based on the single-sided silicon strip detector (SSD). Si strips produced by Hamamatsu (S13804) were used, where the pitch has a width equal to 190 μm. The detector's readout allows for saving waveform for each strip, and it is based on DRS4 chips. The detector was successfully used during three data-taking campaigns with the lead beam at a beam momentum of 150A GeV/c.

Both tasks were necessary in the context of preparation for measurements after Long Shutdown 2, which includes fragmentation measurements planned for autumn 2024.

Keywords: nuclear fragmentation, cosmic rays, charge-changing cross-section, high-energy heavy-ion collisions, physics, NA61/SHINE, CERN

Streszczenie

"Pomiary przekrojów czynnych na proces fragmentacji i rozwój nowych detektorów wiązki dla przyszłych eksperymentów."

Niniejsza praca przedstawia wyniki zadań badawczych zrealizowanych podczas studiów doktoranckich autorki. Gówna część pracy zawiera wyniki analizy pomiarów przekrojów czynnych na proces fragmentacji jądrowej przeprowadzonych przez eksperyment NA61/SHINE. Druga część koncentruje się na zaangażowaniu autorki w modernizację systemu detekcyjnego, która odbyła się podczas Long Shutdown 2 w placówce badawczej CERN.

NA61/SHINE to eksperyment z tarczą stacjonarną, zlokalizowany w północnym obszarze Supersynchrotonu Protonowego (SPS) w CERN. Program fizyczny eksperymentu koncentruje się na badaniu diagramu fazowego QCD, a także na przeprowadzaniu szeregu pomiarów referencyjnych dla eksperymentów badających neutrina i promieniowanie kosmiczne. Pomiary fragmentycjne są częścią programu fizycznego zajmującego się badaniem promieniowania kosmicznego. Celem pomiarów, których analiza jest opisana w niniejszej pracy było zmierzenie przekrojów czynnych na proces fragmentacji jąder o lekkich i średnich masach. Przekroje czynne są kluczowymi elementami przy modelowaniu propagacji promieniowania kosmicznego przez Galaktykę. Przekroje czynne obliczone w tej pracy to przekroje czynne na zmianę ładunku dla trzech typów jonów wiązki: boru, azotu i węgla o pędzie wiązki 13.5A GeV/c. Podczas pomiarów użyto dwóch tarcz węglowej i polietylenowej, ze zmierzonych wartość został także wyznaczony przekrój czynny na interakcję z protonem.

Druga część pracy koncentruję na opisie budowy nowych detektorów pozycji wiązki dla eksperymentu NA61/SHINE. Detektory zostały opracowane i przetestowane podczas Long Shutdown 2. Detektory są zbudowane z krzemowych detektorów paskowych (SSD), użyto matryc wyprodukowanych przez firmę Hamamatsu (S13804), gdzie szerokości przerwy pomiędzy paskami wynosi 190 μm. Odczyt detektora opiera się chipach DRS4, które umożliwiają zapis przebiegu czasowego dla każdego paska osobno. Detektory zostały z powodzeniem wykorzystane podczas trzech kampami zbierania danych z wykorzystaniem wiązki ołowiowej o pędzie 150A GeV/c.

Oba zrealizowane zadania badawcze były kluczowe w przygotowaniach do pomiarów odbywających się po 2022 roku, w tym do drugiej kampanii pomiarowej przekrojów czynnych na fragmentację jądrową, która odbędzie się jesienią 2024 roku.

Acknowledgments

I would like to thank all members of the "Heavy Ions Collision" group at the University of Silesia, of which I'm a member, for all the interesting discussions about analysis and everything not related to it. I would also like to thank the members of the NA61/SHINE collaboration, especially members of the neutrino and cosmic rays research working group and members of the software working group, for their substantive support.

Last but not least, I would like to express my gratitude to all my loved ones who supported me, tried to understand what I was actually doing, and boasted about my achievements at every step.

Contents

Chapter 1

Introduction

This thesis presents the results of the research conducted during the author's PhD studies. The main part of the thesis focuses on the analysis of nuclear fragmentation cross-section measurements conducted by the NA61/SHINE experiment in 2018. The second part focuses on the author's involvement in the upgrade of the detector system during the Long Shutdown 2 in the CERN facility. A detailed description of the experiment physics program and detector system[1] can be found in chapter 3.

The aim of the nuclear fragmentation measurements was to measure the cross-sections for the nuclear fragmentation process of the light and intermediate nuclei. These are essential parameters in modeling the propagation of cosmic rays through the Galaxy. Precise values of cross-sections are used to test and develop the propagation models. Detailed motivation is presented in chapter 2.

Cross-sections calculated in this work are charge-changing cross-sections for three beam ions: boron, nitrogen, and carbon at a beam momentum of 13.5A GeV/c. Cross-sections were calculated for interaction with two types of target carbon and polyethylene, and from the results, cross-sections for interactions with proton were derived. A description of the analysis steps can be found in chapter 4 as well as the theoretical introduction to concepts such as the fragmentation process, charge-changing cross-section, and the derivation of used formulas. Results with statistical and systematic error discussion are placed in chapters 5 and 6.

Chapters 7 and 8 focus on the detector system upgrade, which took place during Long Shutdown 2, and preparation for measurements after 2022, which includes second data taking campaign of nuclear fragmentation measurements planned for autumn 2024.

---

[1]With emphasis on the description of the system used during fragmentation measurements in 2018.

Author's contribution

The author has been a member of the NA61/SHINE collaboration since 2019, participating in three working groups related to software/calibration, hardware development, and neutrino and cosmic-ray analysis. During Long Shutdown 2 at CERN, the author contributed to upgrading the detector system, specifically in the development of new beam position detectors. Two types of detectors were considered: a scintillating fiber detector and a silicon strip detector. The author actively participated in both projects.

The detector described in this thesis is a silicon strip detector. A scintillating fiber detector is still considered and will be tested in the future. The detector is constructed using two perpendicular ribbons, each made of two layers of scintillating fibers. Saint-Gobain, round shape, double cladding scintillating fibers (BCF-60) with $250 \ \mu m$ diameter were chosen. The end of each ribbon is connected to the 256-channel multianode Hamamatsu photomultiplier (H9500) [1]. The author contributes to every step of constructing the detector, from choosing the scintillator and readout type to constructing the ribbons with the use of equipment projected by the author.

The detector that was finally used is a silicon strip detector for which new readout and reconstruction software was developed. The author prepared the software and integrated it with the NA61/SHINE framework. The algorithm processes raw data from the detector to reconstruct the hit positions of beam particles. The reconstructed positions are used for beam monitoring, including measurements of beam width, emittance, and position on the target. The author also developed a beam monitoring module that functioned during measurements. During three data-taking campaigns after the detector system upgrade, the author served as a BPD expert.

During doctoral studies, the author presented her work at three conferences: the Particles and Nuclei International Conference (PANIC), the International Beam Instrumentation Conference (IBIC), and the Mazurian Lakes Conference on Physics.

For the charge-changing cross-section analysis, the author prepared the necessary algorithms and code herself. The results and algorithms were presented at NA61/SHINE collaboration meetings at CERN and discussed in working group sessions.

Beyond her doctoral research, the author actively participated in the broader scientific community. She is an active member of the ECFA panel for young scientists, where she is a part of the group dedicated to young researchers working with software and machine learning for instrumentation. Currently, the group has conducted a study of the quality and availability of training for early career researchers, which prepares them for their future work.

Chapter 2

Nuclear fragmentation cross-section measurements essential for understanding primary cosmic ray propagation process through the Galaxy

Every second, a flux of cosmic rays hits the Earth's atmosphere with an intensity of about 1,000 particles per square meter. They are 90% protons, 9% helium nuclei, and 1% nuclei of heavier elements; most of them have relativistic energies and come from outside the solar system but from within the Galaxy [2]. However, sometimes, particles with ultra-relativistic energy (up to 10^{20} GeV) reach the Earth's atmosphere, in such cases, scientists predict that they may have an extra-galactic origin. Cosmic rays can be divided into primary ones, those that, during their propagation from the source (e.g., supernova explosions), do not undergo processes that change a particle of one type into another one (like fragmentation or decay), and secondary ones that are formed as a result of the mentioned processes. Cosmic ray studies are based on space and ground detectors (like AMS-02 [3], CALET [4], DAMPE [5]) that measure the cosmic rays fluxes, the propagation models that help interpret measured data and the experiments that measure the crucial parameters needed for modeling (like nuclear fragmentation cross-sections measured by NA61/SHINE [6]).

One of the important parameters measured by detectors and studies in experimental collisions is the ratios of secondary to primary particles, especially ratios when the secondary element is Li, Be, B. Because these elements are mostly secondary (like Sc, Ti, V, Cr, and Mn) which can be seen in figure 2.1, which shows the abundance of the elements in measured cosmic rays fluxes (black line) in comparison to the abundance of elements in the solar system (grey line). The graph shows that the two groups of elements differ in their abundance by several orders of magnitude, these are the ones mentioned (Li, Be, B) and (Sc, Ti, V, Cr, Mn). The conclusion drawn is that if they

3

are absent as the end products of nucleosynthesis (grey line) but are present in measured cosmic rays fluxes, they must originate from processes that undergo primary cosmic rays during their propagation, that is, the fragmentation process of primary cosmic rays on the interstellar medium. For this reason, primary to secondary particle ratios described above, together with cross-section values for the spallation process, constitute very good parameters for estimating propagation components such as the diffusion coefficient or column depth of material traversed by cosmic rays.
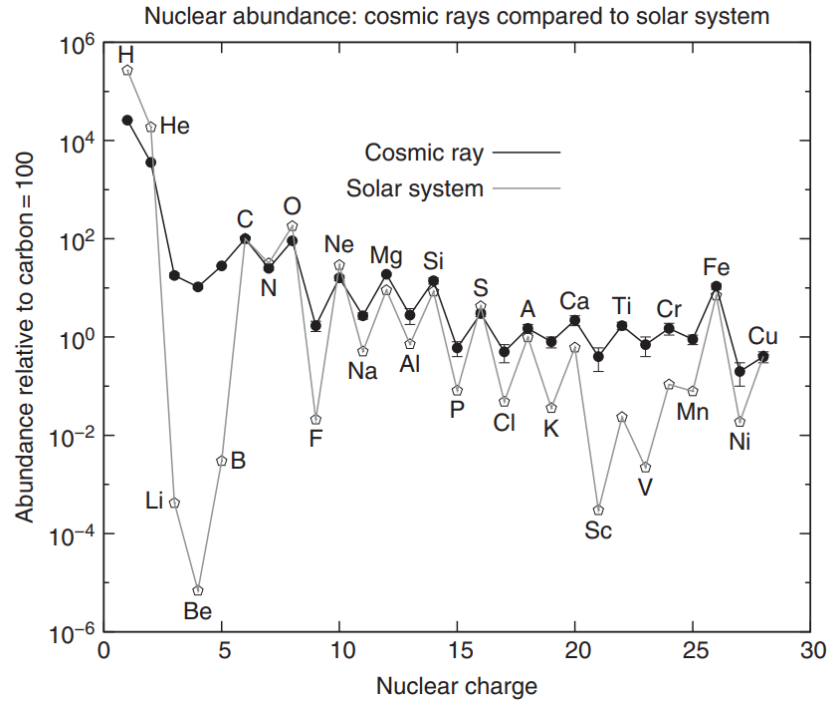
Figure 2.1: Comparison of elemental abundances measured on Earth in cosmic ray fluxes with elemental abundances in the solar system [2]. The values shown are relative values (relative to carbon = 100).

The diffusion coefficient D(E)[1] and the mean amount of matter traversed by a particle X(E) are related by relation $D(E) = \frac{1}{X(E)}$ and are essential parameters when it comes to modeling the transport of charge particles between production and observation under the influence of the Galaxy magnetic field. Besides, the fragmentation process and movement in magnetic field models take into account other important phenomena that particles undergo during their propagation, like acceleration, re-acceleration, convection, and decay. However, different models differ from each other by threatening these processes. The general concept of the modeling propagation of cosmic rays can be discussed with the use of a transport equation 2.1[2] for a particular particle species, which is often a starting point for different models.

---

[1] Diffusion coefficient depends on particle energy.

[2] For simplification, the provided equation is written as if the interstellar medium was made from hydrogen atoms.

$$\frac{\partial N_i(E,x)}{\partial t} + V \cdot \bigtriangledown N_i(E,x) - \bigtriangledown[D(r) \bigtriangledown N_i(E,x)] =$$

$$Q_i(E,x,t) - p_i N_i(E,x) + \frac{v\rho_{ism}(x)}{m_p} \sum_{k \geq i} \int \frac{d\sigma_{i,k}(E,E\prime)}{dE} N_k(E\prime,x) dE\prime \quad (2.1)$$

Here, the left side of the equation describes how the particle distribution evolve due to diffusion and convection, where $N_i(E,x)$ is a particle (of type i), D(r) is the diffusion constant, and V is the convection velocity. The right side represents the particle density gains and losses due to the different processes. The first term represents an injection of particles of type i from source $Q_i(E,x,t)$, and the second term $p_i N_i(E,x)$ represents the loss of nuclei of type i by spallation and decay. The last term of the equation describes the particle production of type i by the fragmentation of heavier nuclei of variety k on the interstellar medium, where ρ_{ism} is the density of the interstellar medium (ISM), m_p is the proton mass, and $\sigma_{i,k}$ is the effective cross-section for the reaction $k + p_{ism} \rightarrow i$.

An example of how diffusion coefficient and the mean amount of matter traversed by a particle can be calculated from measured B/C spectrum[3] will be made with the use of a simplified leaky box model. In this model, it is assumed that particles propagate through a given volume with a constant probability of escape. The mean time spent in the contaminated volume is called escape time (τ_{esc}), and it can be used to reformulate diffusion and convection part form equation 2.1[4] by replacing it with term $\frac{N_i}{\tau_{escp}}$, and to calculate the mean amount of matter traversed by a particle λ_{escp}, see equation 2.2.

$$\lambda_{escp} = \rho_{ism}\beta c\tau_{esc} \quad (2.2)$$

Additional simplifications can be made to determine the propagation equation for boron species, which nicely shows the reason why the B/C ratio is one of the most common ones to measure and use. With the use of the fact that boron is stable and is not produced in cosmic ray sources, the source part can be set to zero Q(E)=0, and the decay part can be omitted, which leads to the transport equation in the form 2.3[5].

$$\frac{N_B(E)}{\tau_{esp}(E)} + \frac{\beta c\rho_{ism}}{\lambda_B} N_B(E) = \frac{\beta c\rho_{ism}}{m_p}[\sigma_{C\rightarrow B}N_C(E) + \sigma_{O\rightarrow B}N_O(E)] \quad (2.3)$$

---

[3]Ratio of the measured boron to carbon flux.

[4]The reformulation is only possible when the condition $c\tau_{escp} >> h$ is met. In simplification, the region of cosmic ray propagation in the Galaxy is treated as a thin cylinder of thickness 2 h = 200 pc and radius equal to 15 kpc.

[5]In leaky box model it is assume that N(E,x) is constant in time.

where $\frac{\beta c \rho_{ism}}{\lambda_B} N_B(E)$ is the equivalent of $p_i N_i(E, x)$ term from equation 2.1 without part connected to decay[6]. For the production of boron, we assume two main channels: the Oxygen and Carbon fragmentation process. Then, because the measured fluxes of carbon and oxygen are nearly equal, we get the formula for B/C fluxes in the form 2.4[7].

$$\frac{N_B}{N_C} = \frac{\lambda_{escp(E)}}{1 + \lambda_{escp(E)}/\lambda_B} + \frac{\sigma_{C \to B} + \sigma_{O \to B}}{m_p} \qquad (2.4)$$

The cross-section values are $\sigma_{C \to B} \approx 73mb$ [7], $\sigma_{O \to B} \approx 30mb$ [8], and the $\lambda_B \approx 7g/cm^2$, calculated with the use of cross-section value for boron fragmentation on hydrogen $\sigma_{B+p} \approx 236$ mb[8]. The B/C ratio values from figure 2.2 [2] will be used in the provided example. Finally, the mean amount of matter traversed by the particle can be calculated for three chosen values[9]: $\lambda_{escp} = 8.5g/cm^2$ for B/C = 0.239 and $E_k = 5A$ GeV, $\lambda_{escp} = 6.0g/cm^2$ for B/C = 2.000 and $E_k = 10A$ GeV, and $\lambda_{escp} = 3.9g/cm^2$ for B/C = 0.155 and $E_k = 20A$ GeV.
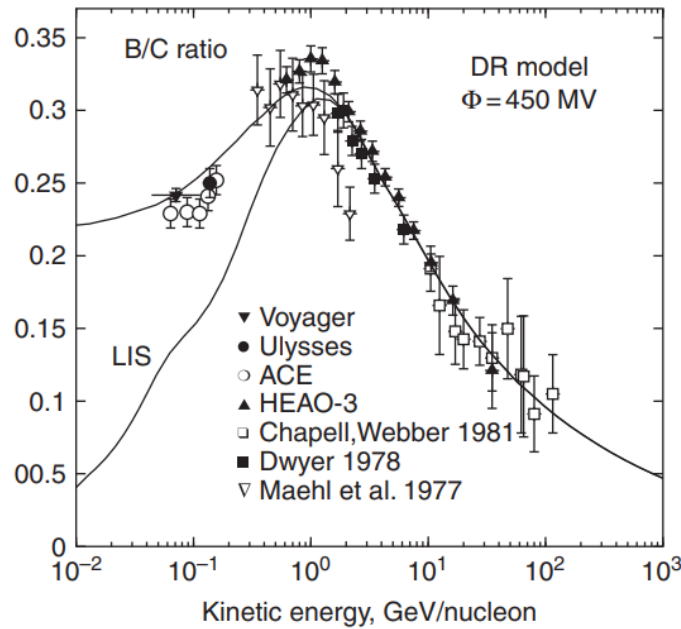
Figure 2.2: Measured B/C ratio spectrum fitted with the function 2.5 [9] reproduce in permission by Thomas K. Gaisser et al. [2]. Reference to the measurements can be found [10–14].

---

[6]In equation 2.1 $p_i N_i(E, x) = \frac{\beta c \rho_{ism}}{\lambda_i} + \frac{1}{\gamma \tau_i}$. The $\gamma \tau_i$ is the particle Lorentz dilated lifetime, and λ_i is the particle mean free path.

[7]Additionally, relation form equation 2.2 was used.

[8]Calculated with use of the equation $\sigma_{inel}^{pA} \cong 45mbA^{0.691}$ [2].

[9]Values were chosen randomly only for example reason.

The measured B/C ratio can be described by power law behavior $\tau_{esc}(E) = R^{-\delta}$. Distribution in figure 2.2 for high energy region ($R > 3GV$) was fitted with function 2.5, with $\delta = 0.6$.

$$\lambda_{escp} = 19\beta^3 \frac{R}{3GV}^{-\delta} \tag{2.5}$$

The above example of the analysis of the measured B/C spectrum was provided mainly to illustrate the inherent relationship between experimental measurements and the development of theoretical models. These measurements and their precise interpretation allow for development in a broad spectrum of astrophysics and astroparticle physics studies, like identifying specific sources of cosmic ray acceleration or studying the nature of the interstellar medium and fields that fill them. However, they are also very necessary when an anomaly is measured, especially if spectra exhibit behaviors that the models used for fit cannot describe. Even the slight derivation from the model's prediction can be the signature of the new phenomena like the search for exotic particles or finding signatures of dark matter annihilation in the Galaxy [15–17].

Unfortunately, currently, propagation characteristics are dominated by large cross-section uncertainties in parallel experiments that measure the cosmic ray fluxes (like AMS, CALET, and DAMPE [18–20]) doing it with increasingly better precision, which requires that the uncertainty associated with cross-sections for fragmentation processes be as small as possible (less than 5%). There is a greater need for measurements of reactions at high energies ($> 10A$ GeV) due to a small number of measurements at such energies. To our knowledge, NA61/SHINE and the SPS are worldwide, the only facilities that allow for this measurement are at a beam momenta higher than 10A GeV/c.

To respond to these needs, the NA61/SHINE collaboration planned new measurements for the nuclear fragmentation cross-sections at beam momentum 13.5A GeV/c, which are scheduled for autumn 2024. Planned activities take into account compressive analysis made by Y.Genolini et al. [21, 22], whose main purpose was to make a ranking of reactions relevant to the production of a given isotope, which new high statistic measurements gradually reduces the influence of the total production cross-section uncertainty for a given isotope. Figures 2.3 and 2.4 present the result of the analysis for the production cross-section uncertainty for twelve elements Li, B, C, N, O, F, Ne, Na, Mg, Al, Si. The first bin presents the current uncertainty. On the x-axis, there are ranked reactions, and on the y-axis is their influence on reducing the total production cross-section uncertainty for a given isotope. Correlated uncertainties are shown in blue, uncorrelated in red, and a combination of correlated and uncorrelated relative uncertainties in green. The gray dashed line indicates the desired precision. The described analysis is a useful guide for experiments planning cross-section measurements for the development of cosmic radiation propagation models like NA61/SHINE. Further discussion about planned activities is include in chapter 8.
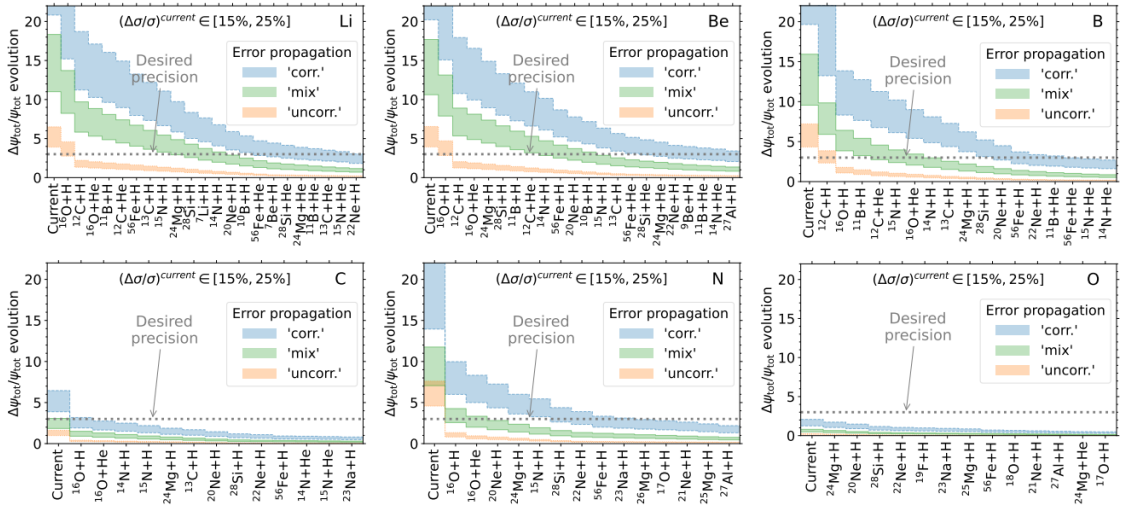
Figure 2.3: Ranked Li, Be, B, C, N, O production reactions in a function of their influence on reducing total production cross-section [22].
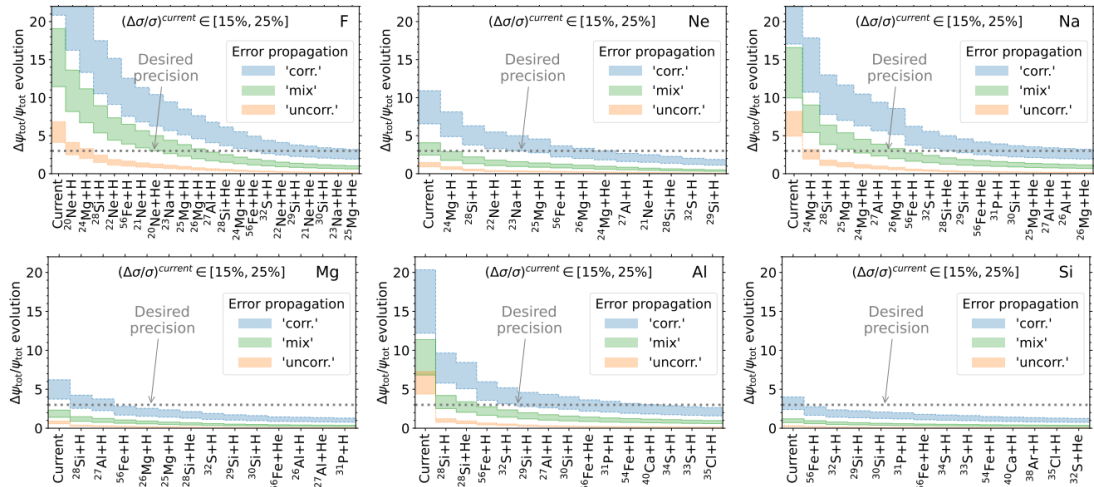
Figure 2.4: Ranked F, Ne, Na, Mg, Al, Si production reactions in a function of their influence on reducing total production cross-section [22].

Chapter 3

NA61/SHINE experiment

NA61/SHINE is a fixed target experiment located at the CERN Super Proton Synchrotron (SPS) [23]. The experiment studies the collision of proton-proton, hadron-nucleus, and nucleus-nucleus systems at relativistic energies. NA61/SHINE uses a broad spectrum of beam momentum as well as beam particle type, from hadrons to lead ions, with a momentum range of 13A GeV/c to 150A GeV/c for ions and 13 GeV/c to 400 GeV/c for hadrons.

In this chapter, the physics program of the experiment and the detector setup will be discussed. The detector setup is optimized before each data taking. The description in the following chapter will be based on a setup from 2018 (including a description of the acceleration chain), which is the year when data was taken for the pilot run for cosmic ray fragmentation studies. The following section also includes a detailed description of the beam and target used during fragmentation measurements, a discussion of collected statistics, and the results of the analysis conducted so far.

3.1   NA61/SHINE physics program

NA61/SHINE physics program focuses on the following topics [24, 25]:

- Study of strong interactions, which includes study of phase transition between hadron gas and quark-gluon plasma. An experiment performed a complex scan in two-dimensional space: beam momentum and system size, which allows for a broad study of phase diagrams of strong interacting matter.

- Measurements of open charm production. Test data, taken in December 2016 on Pb+Pb collisions at 150A GeV/c, proved the general concept of D^0 meson detection via $D^0 \rightarrow \pi^+ + K^-$ decay channel [26], currently under analysis are data taken in 2022/2023 on Pb + Pb collisions at 150A GeV/c.

- Precise measurements of hadron production in p + C collisions for long-baseline neutrino experiments (T2K, NOvA, MINERvA, DUNE) to better estimate neutrino fluxes.

- Measurements of cross-sections and hadron production in $\pi + C$ collisions in order to improve the simulation of the propagation of cosmic ray showers in the atmosphere.

- Nuclear fragmentation cross-section measurements to better understand the propagation of cosmic rays in the Galaxy.

Figure 3.1 shows a summary of collected data in function of beam momentum on the horizontal axis and system size on the vertical axis.
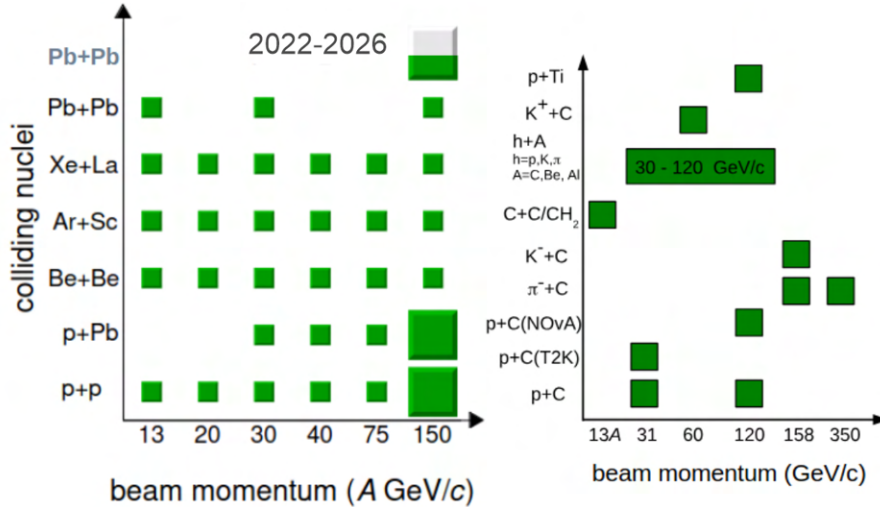
Figure 3.1: Summary of data collected within system size – beam momentum scan performed by NA61/SHINE.

3.2 Experimental system setup

3.2.1 Ion source and accelerator chain

The source of primary lead ions used during data taking was Electron Cyclotron Resonance (ECR) [23]. In that kind of source to create plasma, microwaves are used with a combination of magnetic field to operate on resonance electron frequency, which allows the removal of electrons from deeper layers and traps plasma in a magnetic field to not allow for recombination. The lead gas is made by the evaporation of a solid lead source. Then, an ion beam is formed with the use of electromagnetic optics, accelerated to energy 250A keV by RFQ, analyzed by sets of spectrometers to choose the wanted charge of ions, and injected into the first linear accelerator LINIAC3. In LINIAC3, it reaches energy 4.2A MeV and is stripped from electrons up to charge +54. Then, it is injected into a Low Energy Ion Ring (LEIR), where it is formed into bunches, each containing 2.2×10^8 lead ions. In LEIR, the beam reaches energy 72A MeV. The next step is the proton synchrotron (PS), which accelerates the beam

to 5.9A GeV. The last step before extraction into the H2 beamline[1], is the Super Proton Synchrotron (SPS). Before the beam is injected into SPS, it is stripped of all electrons, and finally, in SPS, it is accelerated to final energy in the range of 13A GeV to 158A GeV.

The layout of the CERN accelerator chain is shown in Figure 3.2.
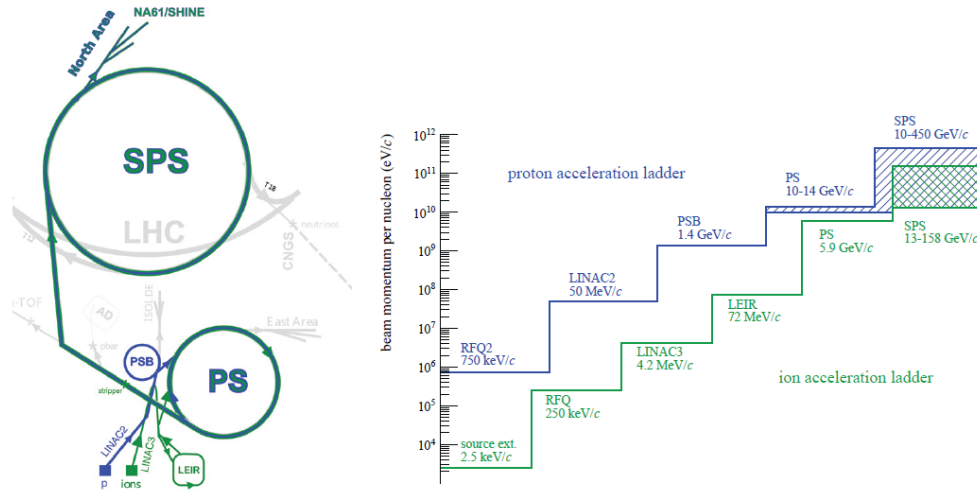
Figure 3.2: CERN acceleration chain layout (left) relevant to NA61/SHINE experiment. Visualization of steps in reaching top beam energy in individual acceleration steps (right).

3.2.2 H2 beam line and secondary ion beam

To the NA61/SHINE experimental hall, the beam is delivered through the H2 beam line. During the fragmentation measurements in 2018, a secondary 13.5A GeV/c beam was used[2]. The beam was formed from the product of the interaction of primary ^{208}Pb ions from the SPS on 160 mm beryllium target T2. Spectrometers were set to pass to experimental hall fragments with a rigidity equal to 27 GV. The layout of the target T2 and beam optic location can be seen in figure 3.3.

The main goal of the measurements was to measure the fragmentation of the ^{12}C beam, so the spectrometers were set to select ions with a mass-to-charge ratio of 2. However, this means that all other ions with this mass-to-charge ratio are also passed into the secondary beam. Then, selecting a specific ion for measurement is done using a trigger system.

Additionally, the particles formed during the fragmentation of the Pb ions exhibit some momentum smearing due to the Fermi motion of the fragments. This smearing causes leakage to the transported beam particles with A/Z != 2, which additionally allows for the analysis of different isotopes of a given ion. Fermi motion depends on the mass and can blur the fragment's momentum distributions by about 3-5%[27].

---

[1]Which is the beamline providing the beam to the NA61/SHiNE experiment.
[2]Momentum accuracy equal to $\Delta p = \|2\%\|$
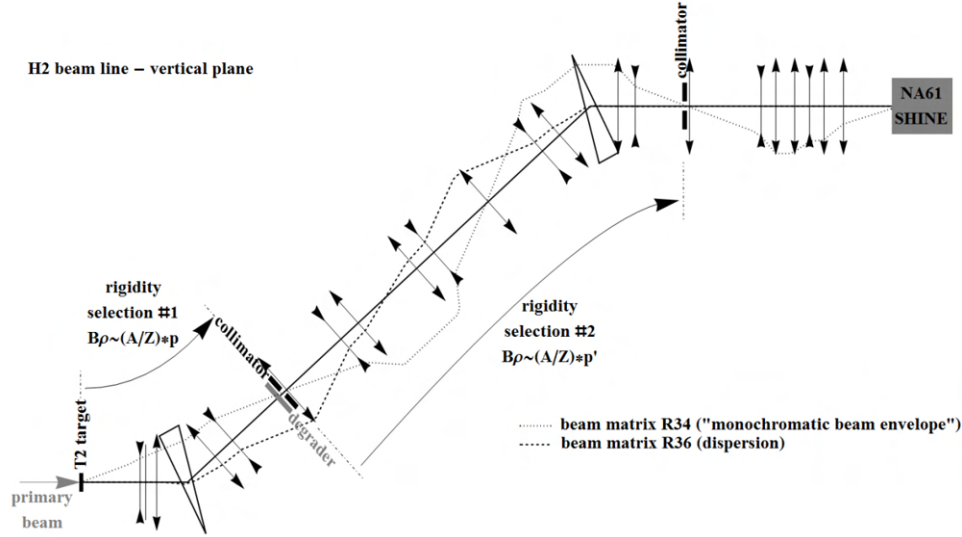
Figure 3.3: Schematic view of H2 beamline.

3.2.3 Nuclear fragmentation cross-section measurements - detector system

The detector system setup consists of two main parts: a set of beam detectors placed before the target (showed in figure 3.5) and a system of time projection chambers (TPCs) placed after the target (showed in figure 3.4)[3].

The set of beam detectors consists of scintillating detectors (S1, S2, V0, V1, V1p) and gaseous detectors (BPDs). Scintillating detectors measure beam divergence (veto detectors), identify the charge of the ion (S1 detector), identify the mass of the beam particle based on the time of flight measurements (A and S1 detector), and are part of the trigger system. Three gas detectors (BPDs) are part of the telescope detector, which measures beam position and reconstructs beam track in the x-z and y-z planes. With the use of this detector, the main vertex of beam interaction with the target is estimated. For the 2018 data-taking campaign, a proportional chamber was used with gas composition Ar/CO_2 85/15 and an active area of 48x48 mm^2. Each BPD consists of two planes of orthogonal readout strips, which allow the measurement of the position of the beam particles in x–y plane. The schematic layout of the BPD plane is shown in figure 3.6.

Parameters of the beam detectors used during fragmentation measurements are placed in table 3.1. A detector and an S1 detector were connected to the DRS4 readout, and they were connected to each other through a 160 m-long cable.

Behind the target, there are detectors that measure the products of the interaction. The main tracking devices are Time Projection Chambers. Two Vertex TPCs (VTPC-

---

[3]The presented detector configuration describe the set up for the 2018 fragmentation measurements. Detector configuration after the Long Shut Down 2 will be discussed in more detail in the section 7 dedicated to a detector system upgrade.
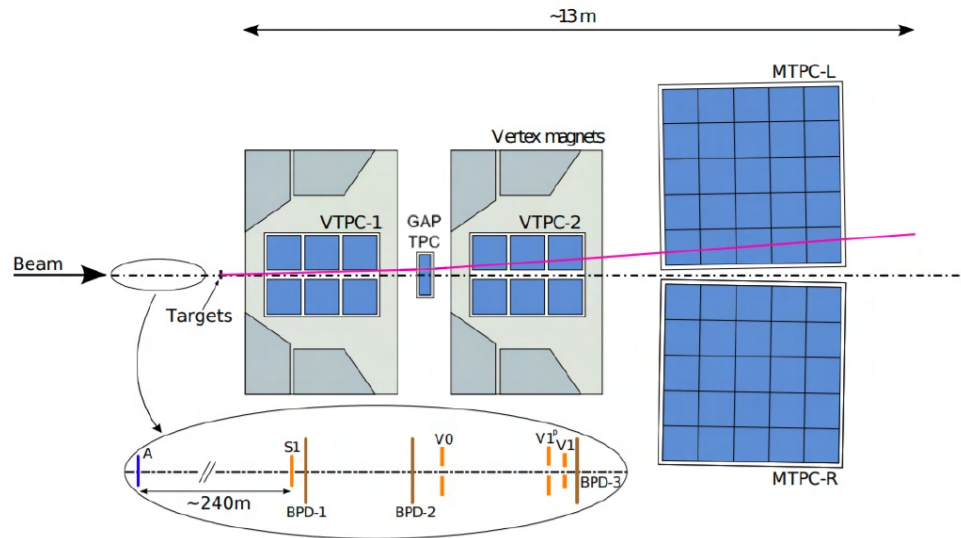
Figure 3.4: Schematic layout of the detector system setup during the 2018 data-taking campaign.
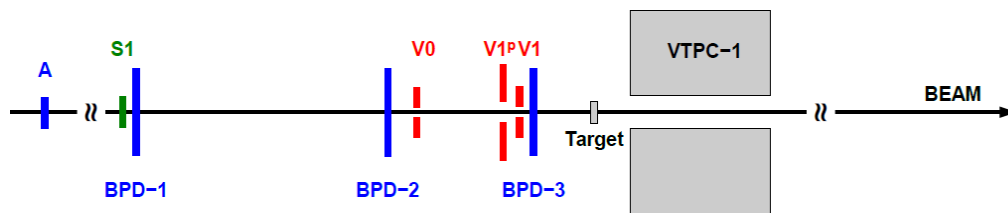
Figure 3.5: Schematic layout of the beam detectors setup.
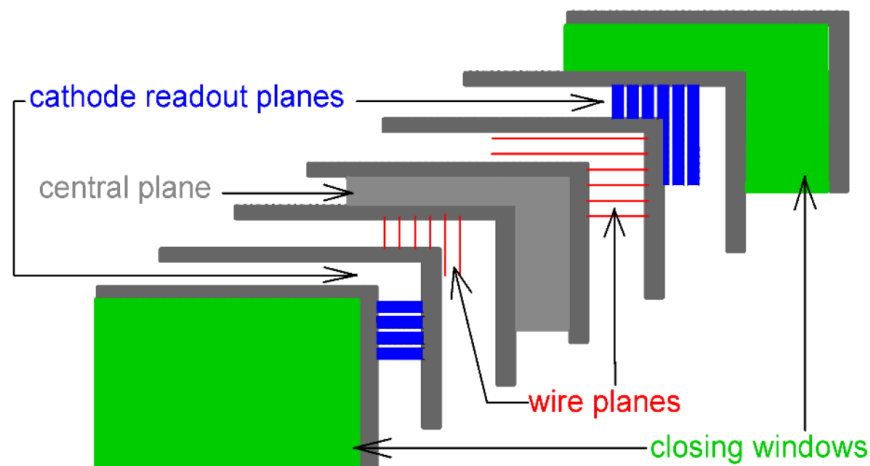
Figure 3.6: Schematic layout of the plane of Beam Position Detector - proportional chamber.

1 and VTPC-2) are placed in a magnetic field, with a smaller GAP TPC chamber between them, which records particles tilted by a small angle from the position at x equal to zero. At the end, there are two main TPCs chambers (MTPC-L and MTPC-R), which serve as two main spectrometers due to the fact that products deflected in a magnetic field are best visible in these chambers and also due to the fact that they have the largest number of measuring electrodes and, therefore, the best resolution. Information on energy losses (dE/dx), together with measurements of the particle's deflection in the magnetic field, allows for a broad identification of interaction products. Parameters of Time Projections Chambers used to analyze the interaction products are placed in table 3.1.

Table 3.1: (Top) Parameters of used beam detector with position along the beam line. The last line contains the target Z position on the beam line. (Bottom) Parameters of used Time Projection Chambers.

Beam detector	Dimensions [mm]	Hole [mm]	Z position [m]
A	60 x 60 x 5		$\approx$ -270
S1	60 x 60 x 5		-36.42
V0	$\circ$ = 80 x 10	$\circ$ = 10	-14.16
$V1^p$	300 x 300 x 10	$\circ$ = 20	-6.74
V1	$\circ$ = 100 x 10	$\circ$ = 8	-6.72
BPD-1	48 x 48 x 32.6		-36.20
BPD-2	48 x 48 x 32.6		-14.90
BPD-3	48 x 48 x 32.6		-6.70
Target			-5.81
TPC dtector	Dimensions [cm]		Gas mixture
VTPC	250 x 200 x 98		Ar/CO_2 (90/10)
MTPC	390 x 390 x 180		Ar/CO_2 (95/5)
GTPC	30 x 81.5 x 70		Ar/CO_2 (90/10)

3.2.4 Nuclear fragmentation cross-section measurements - trigger configuration

The purpose of the trigger system is to save only the events that are interesting according to the goal of the measurements. The selection is made online, which optimizes the amount of storage data for future analysis. The trigger system uses analog signals from different detectors along the beamline; they need to be recorded in the proper time window and are used in coincidence or anti-coincidence. Signals are discriminated by a Constant Fraction Discriminators, and if the amplitude is high enough, they are passed to the core of the trigger logic – unit based on a Field Programmable Gate Array (FPGA). Then, the main trigger is generated, and data are

passed to the data acquisition system. The trigger system allows the operation of four different triggers in parallel. It needs to be mentioned that the scaling factor is used for different triggers, which allow to decide during measurement what ratio of different types of events will be stored. Two types of trigger were used during fragmentation measurements: T1 and T3. The logic formula for each trigger is described by the equation 3.1 and 3.2.

$$T1 = S1 \wedge \overline{V1} \tag{3.1}$$

$$T3 = S1_C \wedge \overline{V1} \wedge S1_{delayed} \tag{3.2}$$

Here, the notation $\overline{V}$ means that there was no signal measured in the veto detectors. Veto detectors measure the divergence of the beam; this allows not to save events from beam halo. The T1 trigger was set to register all beam particles. Trigger T3 fulfills an online preselection of ^{12}C based on the signal of the S1 detector. The signal in the scintillation detector is proportional to Z^2 of the ion, $S1_C$ means that the signal in S1 (after calibration) corresponds to $Z^2 = 36$. $S1_{delayed}$ is the delayed signal from the S1 detector, which is used to check whether two particles have been registered in a given time window. For the T3, the trigger scaling factor was equal to 1, and for the T1, the trigger scaling factor was equal to 0.18.

3.2.5 Nuclear fragmentation cross-section measurements - target parameters, beam composition, and measurements statistic

During nuclear fragmentation measurements in 2018, two types of targets were used: graphite (C) and polyethylene target (C_2H_4). Parameters of each target can be found in table 3.2. Additionally, measurements were made without the target to examine the influence on the cross-section values interaction of the beam particles with detector material. The targets photo can be seen in figure 3.7.

Table 3.2: Graphite (C) and polyethylene (C_2H_4) target parameters.

	volume density	thickness	molar mass	density
target type	n $[\frac{1}{cm^3}]$	d [cm]	M $[\frac{g}{mol}]$	$\rho[\frac{g}{cm^3}]$
C_2H_4	1.99x 10^{22}	1.5	14	0.924
C	9.23x 10^{22}	1	12	1.84

Beam composition can be seen in figure 3.8[4]. Beam composition measurements are conducted with the use of S1 and A detectors (scintillation detectors). With the use of these types of detectors, ions can be separated according to their charge, the signal generated in scintillating material is proportional to Z^2. Isotope separation is

---

[4]The Y-axis is calibrated to show the difference in time of flight according to the ^{12}C isotope as a main data-taking isotope.
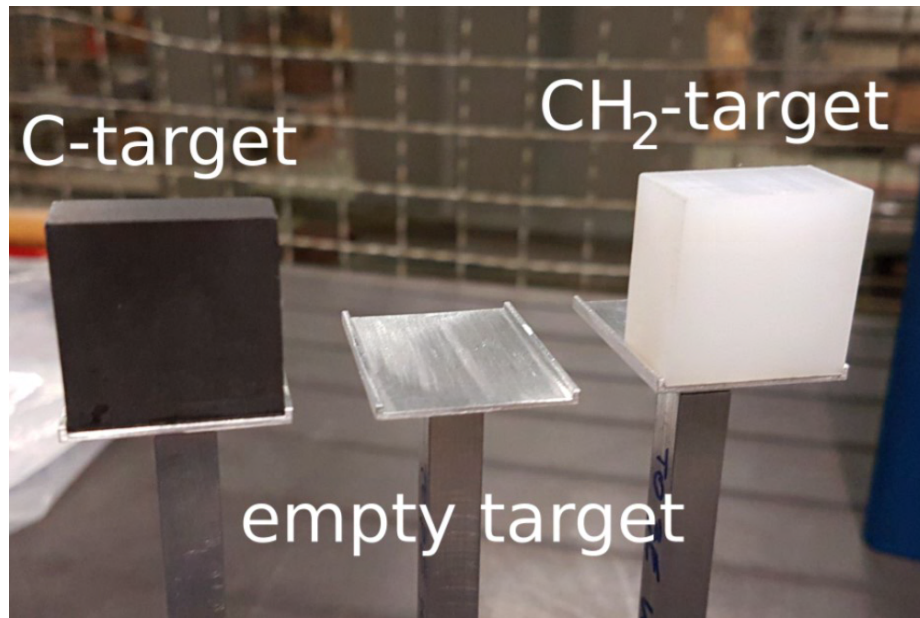
Figure 3.7: Target used during measurements: graphite target, empty holder (for no target measurements), and polyethylene target.

made based on time of flight measurements between A and S1 detectors. The statistic of the measurements is shown in table 3.3.
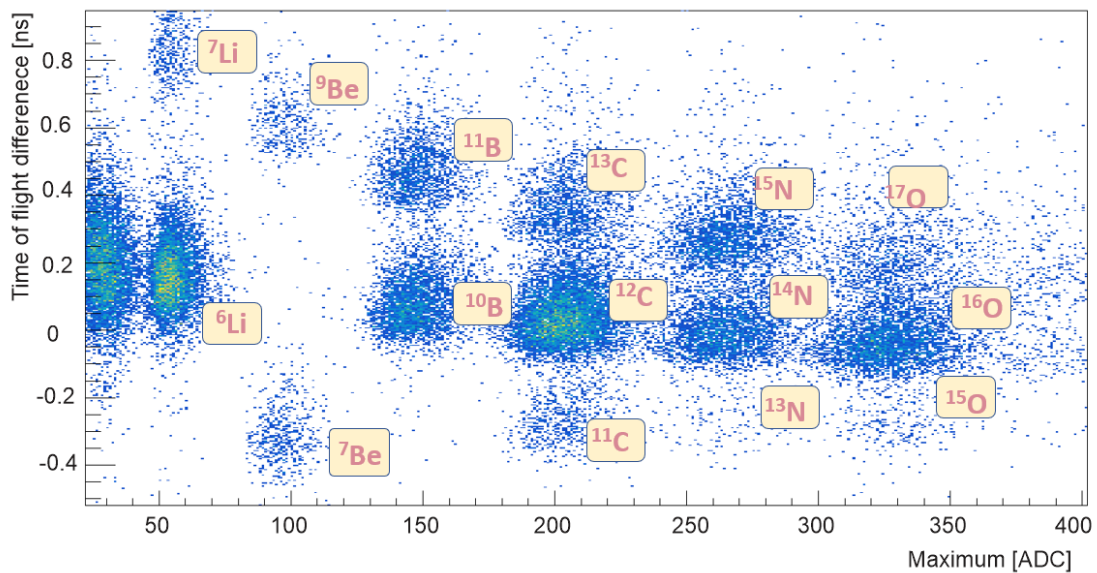
Figure 3.8: Beam composition obtained by measuring S1 signal (proportional to Z^2 of the ion) and time of flight between A and S1 detector (proportional to $\frac{1}{m}$, where m is the isotope mass).

Table 3.3: Statistic of the 2018 pilot run. OUT refers to measurements without target insert.

target type	statistic in percentage	number of events
C_2H_4	46.5 %	553 131
C	43.5 %	517 311
OUT	10 %	119 067
SUM		1 189 509

3.2.6   Nuclear fragmentation cross-section measurements - summary of the current results

The analysis conducted so far was mainly focused on the calculation cross-sections of ^{11}B and ^{10}B production in the fragmentation process, as well as on studies of contribution to the mentioned cross-sections decay of ^{11}C isotope. As was mentioned in the previous subsection, data were taken with carbon and polyethylene targets, and with the use of calculated cross-sections, cross-sections for the reaction with the proton were derived. The results of the analysis completed so far are listed below:

- ^{12}C mass changing cross-section for reaction $^{12}C + p$, results can bee seen on figure 3.9 [28],

- ^{11}C production cross-section for reaction $^{12}C + p$, results can bee seen on figure 3.10 [28],

- ^{10}B and ^{11}B production cross-sections for reaction $^{12}C + p$, results can bee seen on figure 3.10 [28].

Both the listed results of the pilot-run data analysis and the results presented in this work prove that the NA61/SHINE facility is able to make these types of measurements with high quality and give the members of the collaboration experience to continue studies with high statistics.
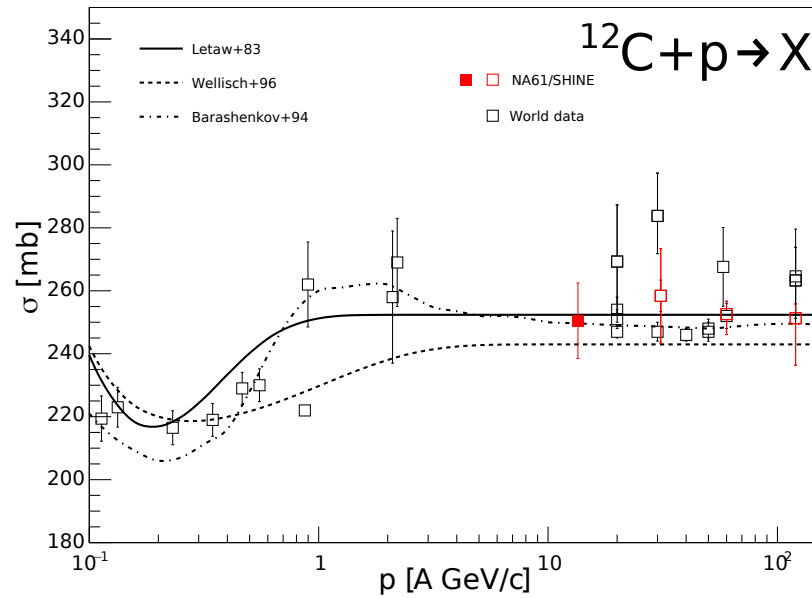
Figure 3.9: ^{12}C mass changing cross-section for reaction $^{12}C + p$ (red solid square). Red empty squares present previous measurements in p+C interactions conducted by NA61/SHINE [29, 30]. The lines represent various momentum-dependent parametrizations of the mass-changing cross-section, detailed description as well as reference to the presented world data (empty back squares) can be found in [28].
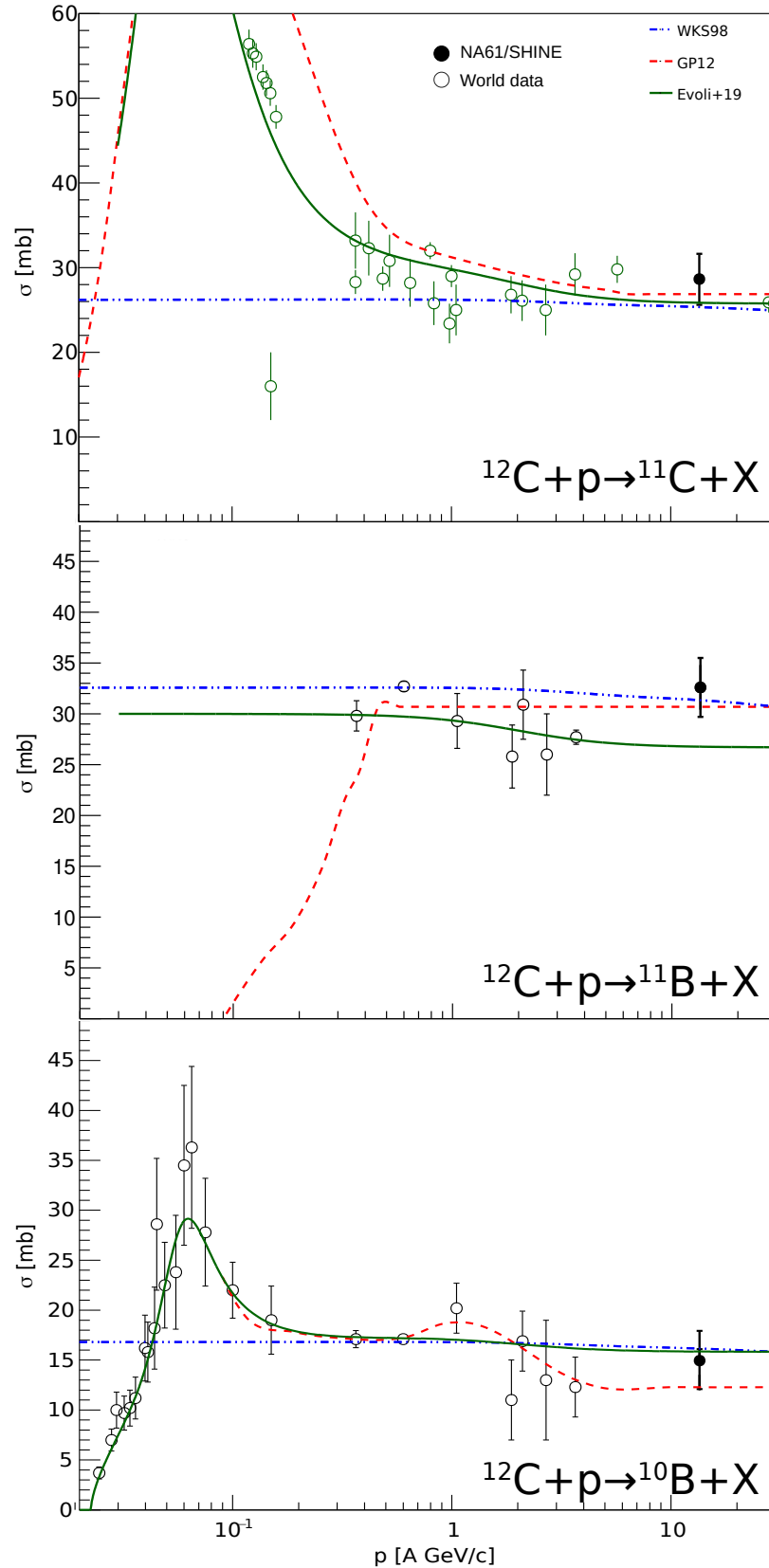
Figure 3.10: ^{11}C, ^{10}B and ^{11}B production cross-sections for reaction $^{12}C+p$. The lines represent various momentum-dependent parametrizations of the mass-changing cross-section, detailed description as well as reference to the presented world data can be found in [28].

Chapter 4

Charge-changing cross-sections: analysis

The main goal of the analysis is to calculate charge-changing cross-sections for the fragmentation process of four types of projectile. In this chapter, the workflow of the analysis will be described. Every step of the study will be discussed. First is the beam composition analysis, followed by the analysis of the product of the interaction of the selected beam particle with the target. The description will be pressed by the theoretical introduction of cross-section (with an emphasis on charge-changing cross-section), the probability of interaction definition, and the derivation of the used equation.

4.0.1 Definition of cross-section and probability of interaction

The cross-section is a quantity that determines the probability of interaction between two colliding particles [2, 31]. In case fixed target setup cross section for the certain process σ_j can be described in simple terms as the rate of this process divided by the flux of incoming particles ϕ_a 4.1.

$$\sigma_j = \frac{1}{\phi_a} \frac{dN_j}{dt} \tag{4.1}$$

The flux of the particles ϕ_a can be described as a rate at particles cross area A in a given unit time dt 4.2.

$$\phi_a = \frac{dN_a}{dAdt} \tag{4.2}$$

Properties of the crossed area dA are determined by the thickness of the target d_T and target volume density $n = \frac{N_A \rho}{M}$, where N_A is the Avocadro constant, ρ is the density of the material, and M is material molar mas 4.3.

$$dA = \frac{1}{nd_T} \tag{4.3}$$

To estimate the correlation between interaction probability and cross-section for a given reaction σ_j, interaction probability P_j must be determined. Interaction probability is commonly defined as the ratio of the number of reactions N_j to the number of incident beam particles N_a. This relationship can be used to transform formula 4.1 into form 4.4 where the relationship between cross-section and probability is clearly defined.

$$\sigma_j = dAP_j = \frac{1}{nd_T}P_j \tag{4.4}$$

In the course of data analysis, the probability of interaction will be estimated with the use of the number of particles left in the beam without the interaction N(d), described by the relation $N(d) = N_a e^{-nd\sigma_j}$, then the the formula for probability of interaction is describe by equation 4.5.

$$P_j = 1 - \frac{N(d)}{N_a} = \frac{N_j}{N_a} = 1 - e^{-nd_T\sigma_j} \tag{4.5}$$

All the above derivations lead to the cross-section formula, which is used in the estimation of charge-changing cross-sections 4.6:

$$\sigma_j = -\frac{ln(1 - P_j)}{nd_T} \tag{4.6}$$

4.0.2 Definition of fragmentation process and charge-changing cross-section

Fragmentation process. The nuclear fragmentation process in heavy ion collision can be described with the use of the Abrasion-Ablation model 4.1. It is a macroscopic model that describes well peripheral collision at high energies when the relative velocity of the reaction partners is bigger than the Fermi velocity of the nucleons. The model was introduced by Bowman et al. [32], then it was examined in later works of the scientific community, and further corrections were introduced [33–36].

The Abrasion-Ablation model describes the fragmentation process in two steps, characterized by two different time scales: the abrasion phase (phase 1) is a fast process with an order of magnitude approximately 10^{-23}s, and the ablation phase (phase 2), which involves the de-excitement of the excited fragment, is relatively slow. According to the statistical model, the time of de-excitement is dependent on excitation energy and varies in the range $10^{-16}s - 10^{-21}s$.

In the model, nucleon-nucleon collisions predominantly occur within the overlap zone[1]. Meanwhile, the spectators, such as the parts of the projectile and target that lie outside the overlap zone, continue to travel at nearly the same velocities as the initial ones. Collision participants form the so-called "fireball." Then, the first

---

[1]Assuming that the project moves in a straight line even after the interaction, an overlap or interaction zone can be defined.

evaporation takes place, which is emission almost isotropically in the center-of-mass system of nucleus: pions and nucleons.

In the ablation phase, the secondary participants of the projectile nucleus form a preliminary pre-fragment. This is only slightly excited by the interaction with the target nucleus and moves on in a beam direction with approximately the same velocity as the projectile. By absorption of the emitted particles from the "fireball," the excitation energy of the pre-fragment increases until, finally, the second evaporation process of nucleons and particles occurs. The evaporation sequence halts when the excitation energy drops below the minimum particle emission threshold. In this way, a stable final state is reached, and the final fragment is formed.
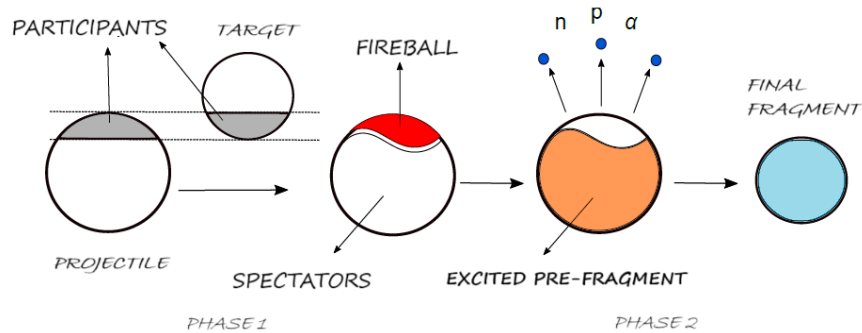
Figure 4.1: Graphical description of the fragmentation process of a projectile in the two-phase model.

Charge-changing cross-sections. For a given interaction of the projectile with the target, the total cross-section can be estimated. The total cross-section is a sum of cross-sections for elastic and inelastic processes [2]. This work is focused on the inelastic process, wherein the initial and the final states are different, and the collision energy is partially converted into a certain nuclear transformation.

For the fragmentation process, several types of inelastic cross-sections are under investigation: production cross-sections, neutron removal cross-sections, mass-changing cross-sections, and charge-changing cross-sections. The charge-changing cross-section describes the likelihood of an incident nucleus losing protons in the interaction with the target nuclei, and they are the topic of interest in this work. In high energy regions[2][3], the total reaction cross-section can be described as a sum of neutron removal cross-section and charge-changing cross-section. Results of the conducted experiments show that charge-changing cross-sections constitute 90% of the total reaction cross-section [37]. The most common models used in estimating the charge-changing cross-section are based on the Glauber model. However, past and current research described in these sections have shown that corrections must be applied to describe phenomena that the Glauber model does not include. An example is the neutron

---

[2]When in an inelastic reaction cross-section, inelastic scattering can be negligible.

[3]This work is focused on analyzing data of the projectile energy above 1A GeV region.

contribution to the charge-changing cross-section proved by several studies and estimates that this influence could be on a level at least 10% [38]. This causes the need for the development of the models and the introduction of corrections. One of the proposed and examined solutions was to, instead of using only the proton densities of the projectile in the calculations, take neutron densities into account as well. The proposed correction factor by T. Yamaguchi et al. coincided well with the experimental data [37]. Most recent works prove the influence of the projectile neutron contribution to the charge-changing cross-section [39] and investigate more deeply the possibility of the contribution of the charged-particle evaporation process from the intermediate pre-fragments, which is not included in the Glauber model. The presented detailed description of these processes is that stripping neutrons from the projectile during collisions at relativistic energies causes the excitation of the remaining nucleus to states above the charged-particle emission threshold. During the de-excitation, charged particles like protons or alpha particles are emitted, which contributes to the value of a charge-changing cross-section.

Simultaneously, the dependencies of charge-changing cross-section values on projectile mass, as well as the mass number of the target nucleus and collision energy, are continuously being studied. Both theoretical and experimental data show that the charge change increases almost monotonically with the mass number of the target nucleus [38]. For total reaction cross-section in nucleus-nucleus collision at high energies[4] in a simplified geometric approximation, dependencies on projectile and target mass number can be described with the use of formula 4.7 proposed by Bradt and Peters in 1950 [40].

$$\sigma_r = \pi r_0^2 (A_p^{1/3} + A_t^{1/3} - b_0)^2 \qquad (4.7)$$

where A_P is the projectile mass number and A_T is the mass number of the target nuclei, b_0 is the impact parameter and r_0 represents the average radius of a nucleon and is equal to 1.2 fm. Because of significant energy dependencies, the simplification can not be used for lower energies, and additional effects should be taken into account, like the influence of the Coulomb screening.

Total reaction cross-section energy dependence is shown in schematic view in figure 4.2 [41]. At low energy below 200A MeV, the cross-section value decreases because of the Coulomb shielding effect; at higher energies, the shielding effect starts to decrease, which causes an increase in reaction cross-section values. Above 280A MeV, non-elastic channels start to be open for nucleon-nucleon interaction, which slightly increases the cross-section value (280A MeV is the threshold for π^0 production). Above a couple of GeV, it is assumed that cross-section values can be approximated by a simple geometrical formula 4.7 and remain constant. Dependence of the total reaction cross-section on the projectile energy with the comparison of seven models along with experimental data are shown in figures 4.3 for reaction $^{12}C + C_2H_4$ and 4.4 for reaction $^{12}C + C$. The open triangles reference charge-changing cross-sections[5].

---

[4]Above 1.5 GeV.

[5]Cause of choosing this example is because these two reactions are also examined in this work.
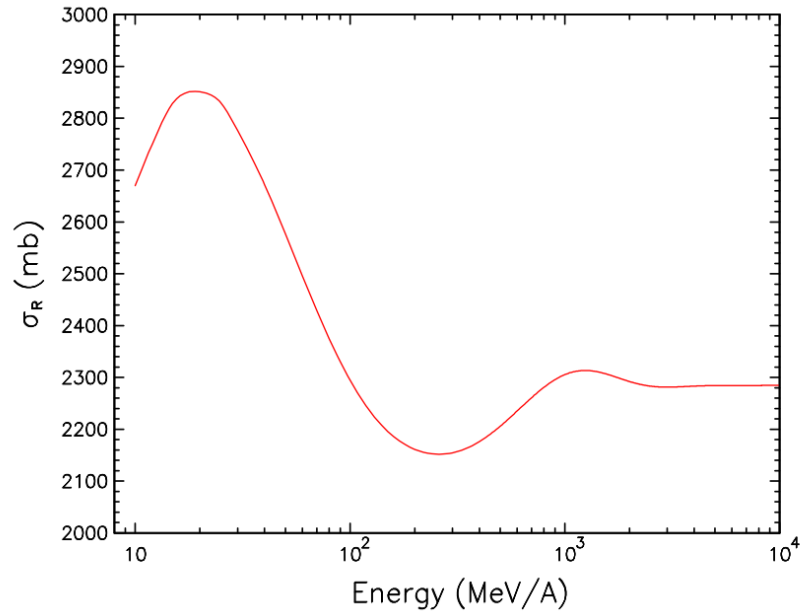
Figure 4.2: Schematic view of dependency of total reaction cross-section on projectile energy [41].
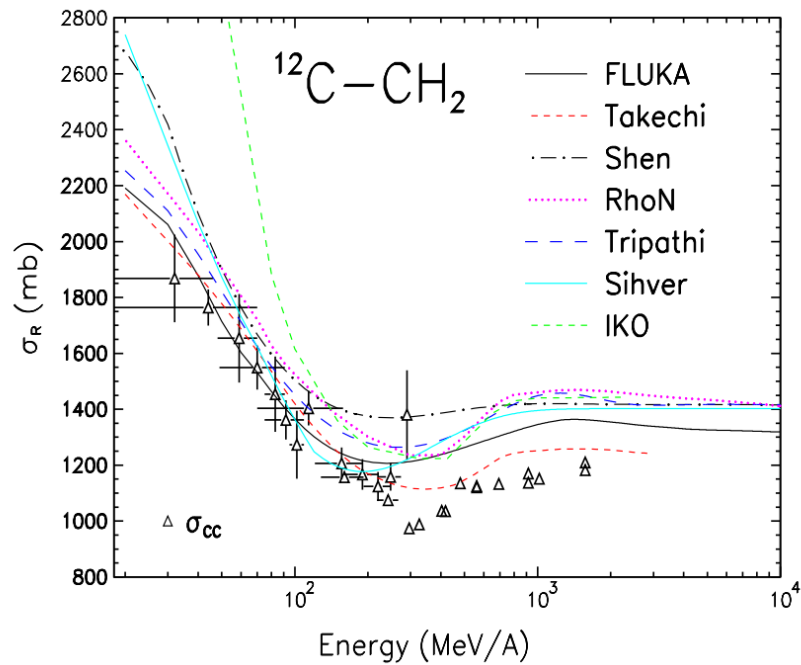
Figure 4.3: Total reaction cross sections calculated with the use of seven different models for reaction $^{12}C + C_2H_4$ compared with experimental data, where triangles represent the charge-changing cross-section values [41].
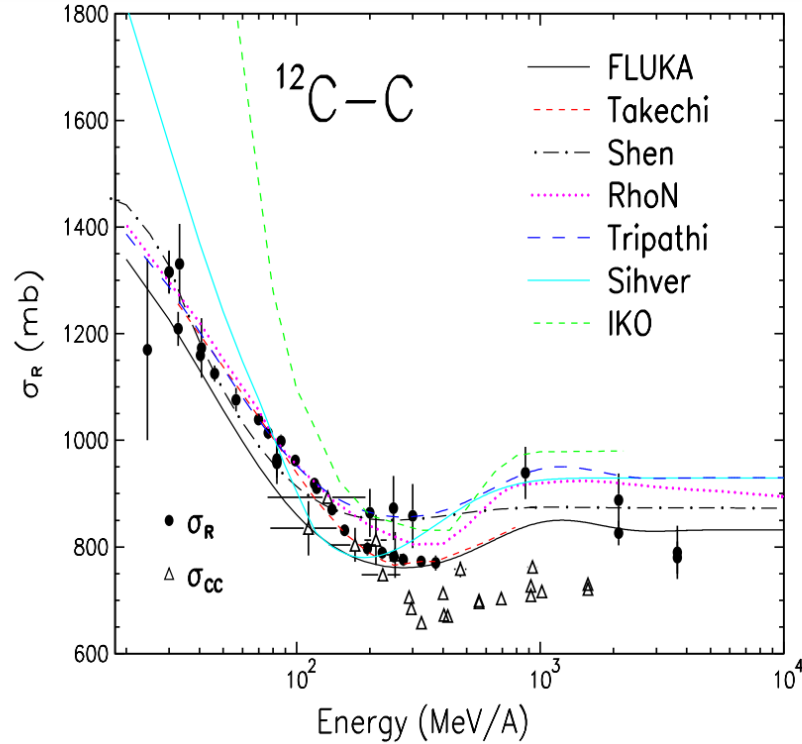
Figure 4.4: Total reaction cross sections calculated with the use of seven different models for reaction $^{12}C + C$ compared with experimental data, where triangles represent the charge-changing cross-section values [41].

It is clearly visible that the models vary from one another. All current models assume that after the resonance energies (above a couple of GeV), the cross sections are independent of the projectile energy. Therefore, more experimental data are needed to examine this assumption. At lower energy levels, the notable differences between the models are caused by the distinct approaches to handling Coulomb effects. Additionally, different models have different prediction power, which depends on the energy region and system size on which it was optimized. However, a general comparison of presented models and available data shows that models developed by Tripathi et al. [42], Andersen et al. [43] and Takechi et al. [44], appear to fit the observed data more accurately than the other models. The model developed by Tripathi et al. is a modified version of Bradt–Peters formula [40], and it was future developed by Andersen et al. and used in heavy ion transport code FLUKA [45].

4.0.3 Probability of interaction - description of the mathematical formulas used during calculations

To calculate the cross-section for a given process, the first probability of interaction must be estimated, as mentioned in subsection 4.0.1. Considering measurement with the target, the probability of interaction consists of three parts, as is shown in the equation 4.8 and figure 4.5. The probability of beam particles interacting upstream of the target P_{int}^{up}, the probability that particles interact in the target P_{int}^{T}, and the probability that beam particles interact downstream of the target P_{int}^{down}.

$$P_{int} = P_{int}^{up} + P_{int}^{T}(1 - P_{int}^{up}) + P_{int}^{down}(1 - P_{int}^{up})(1 - P_{int}^{tar}) \quad (4.8)$$
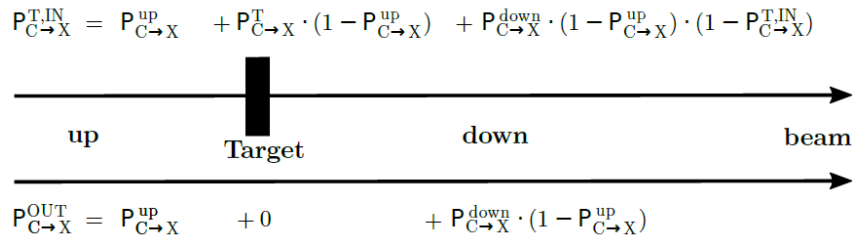
Figure 4.5: Schematic view of three types of interaction which adds up to total probability of interaction.

In the case of measurement without the target (target-out) probability of interaction is described by the equation 4.9 and bottom side of the figure 4.5.

$$P_{int} = P_{int}^{up} + P_{int}^{down}(1 - P_{int}^{up})(1 - P_{int}^{tar}) \quad (4.9)$$

The solution of this system of equations is a formula for the probability of interaction in the target P^{T} with the correction for target-out interaction P^{OUT} 4.10.

$$P_{c}^{T} = \frac{P^{T} - P^{OUT}}{1 - P^{OUT}} \quad (4.10)$$

In this analysis, the probability of interactions P^{T} and P^{OUT} are calculated with the use of equation 4.5. For target-out and target-in data, individual equations are described by formulas 4.11 and 4.12.

$$P^{T} = 1 - \frac{N(d)}{N_a} \quad (4.11)$$

$$P^{OUT} = 1 - \frac{N(d)}{N_a} \quad (4.12)$$

where the N(d) and N_a are calculated according to the following scheme:

- N(d) is the number of beam particles left the target without the interaction; this quantity is calculated with the use of so-called downstream cuts (described in subsection 4.0.6), and the main recording device is MTPC.

- N_a is the number of beam particles hitting the target; this quantity is calculated with the use of so-called upstream cuts (described in subsection 4.0.4), and the main recording devices are two scintillating detectors S1 and A detector, which measures particles charge and time of flight between detectors.

For each probability 4.11 and 4.12, uncertainty is calculated with the use of the error propagation method 4.13.

$$\delta P_{int} = \sqrt{\frac{P_{int} - P_{int}^2}{N_a}} \qquad (4.13)$$

4.0.4 Upstream analysis - beam composition analysis

Beam composition measurements were made using two scintillating detectors: A and S1 detectors. The S1 detector was used to identify ion charge. In scintillating detectors, when a charged particle passes through detector material, it loses its energy in the process of electron material ionization. When electrons return to their stable state, they emit photons. The emitted light signal is proportional to the square of the ion charge. Photo-multipliers are used to convert light signals into an electrical current. In the S1 detector, four photomultipliers (pmt) are used, and the signal is averaged according to the formula 4.14, where A is the amplitude of the signal, and i corresponds to the part number.

$$A_{S1} = \frac{1}{4} \sum_{i=1}^{4} A_i \qquad (4.14)$$

The beam composition measured by the S1 detector with the T1 trigger is shown in figure 4.6. Analysis was made for three beam ions: boron, carbon, and nitrogen. Each peak is clearly visible on the 1D spectrum. To each peak, the Gauss function 4.20 is fitted with asymmetric sigma values (sigma left σ_L and sigma right σ_R) 4.21. The intersection of the fitted functions was determined and used in later analysis steps to determine the cut values[6]. Additionally, beryllium and oxygen were fitted to estimate cuts for boron and nitrogen. The intersection values and fit results can be found in table 4.1.

---

[6]In table 4.1 intersection with neighboring distributions are labeled as cross down and cross up.
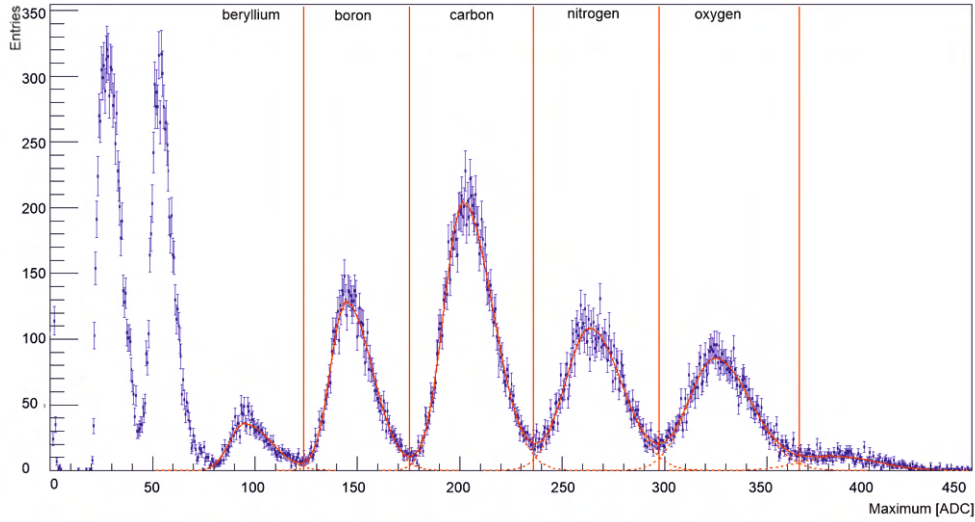
Figure 4.6: Beam composition for T1 trigger, on the x-axis is ADC signal from S1 detector.

Table 4.1: Beam composition T1 trigger - fit results.

Projectile	mean [ADC]	σ_L	σ_R	cross down	cross up
Boron	144.32	7.48	12.75	124	175.5
Carbon	201.68	9.28	14.42	175.5	236
Nitrogen	263.37	12.05	15.73	236	297.5

Isotope separation was made with the use of the time of flight measurements between A detector and S1 detector. The time of flight between two detectors at the distance L is given by the formula 4.15.

$$t = \frac{L}{\beta c} \tag{4.15}$$

Where $\beta = \frac{p}{E}$. Longitudinal momentum p can be expressed by rigidity and isotope atomic number $p = RZ$, and total relativistic energy can be expressed by rigidity, isotope atomic, and mass number $E = \sqrt{p^2 + m^2} = \sqrt{(RZ)^2 + (Au)^2}$. Then the expression for difference (Δt) in time of flight at a distance L for two isotopes with the mass number A_1 and A_2 is given by expression 4.16. This clearly shows that mass separation can be done with the use of the time of flight measurements.

$$\Delta t = \frac{L}{c}\left(\sqrt{1 + (\frac{A_1 u}{RZ})^2} - \sqrt{1 + (\frac{A_2 u}{RZ})^2}\right) \tag{4.16}$$

A detector had a similar setup as the S1 detector with one difference: the signal is read out by two photomultipliers, which are put in front of each other. The timing point is calculated with the constant fraction discrimination method both for S1 and

A detector, then for each detector, the mean value is calculated with the use of equations 4.17 and 4.18, where the i represent the pmt number. Finally, the time of flight between two detectors is calculated with the use of the formula 4.19.

$$t_{S1} = \frac{1}{4} \sum_{i=1}^{4} t_{S1i} \tag{4.17}$$

$$t_A = \frac{1}{2} \sum_{i=1}^{2} t_{Ai} \tag{4.18}$$

$$ToF = t_{s1} - t_A \tag{4.19}$$

The time of flight distributions for three analyzed ions are shown in figures 4.7, 4.8 and 4.9. Distribution for carbon is shown for high statistics (trigger T3); the rest of the distributions are shown only for the T1 trigger to get better resolution. The x-axis is calibrated to show the difference in time of flight according to the ^{12}C isotope as a main data-taking isotope. To each distribution, the Gauss function 4.20 is fitted with asymmetric sigma values (sigma left σ_L and sigma right σ_R) 4.21, results of the fit are shown in table 4.2.
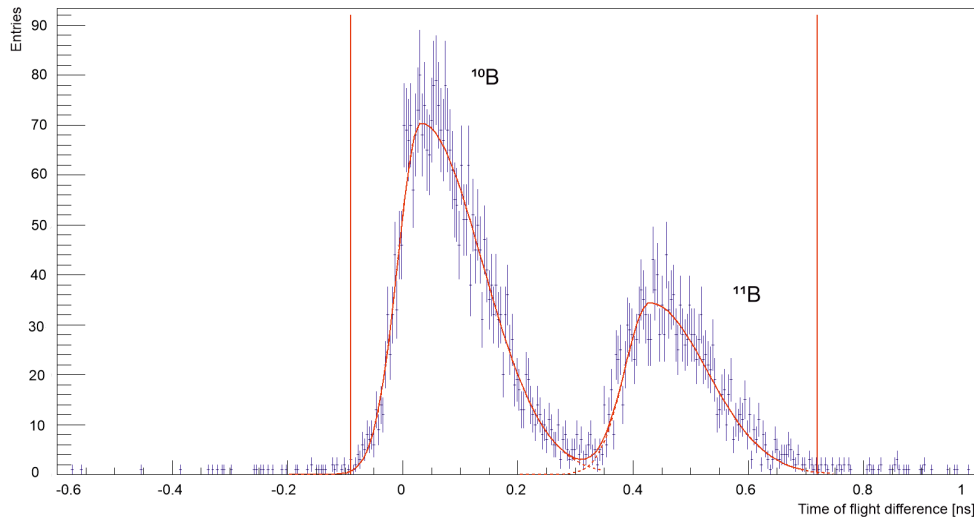
Figure 4.7: Time of flight distribution for ^{10}B and ^{11}B isotopes.
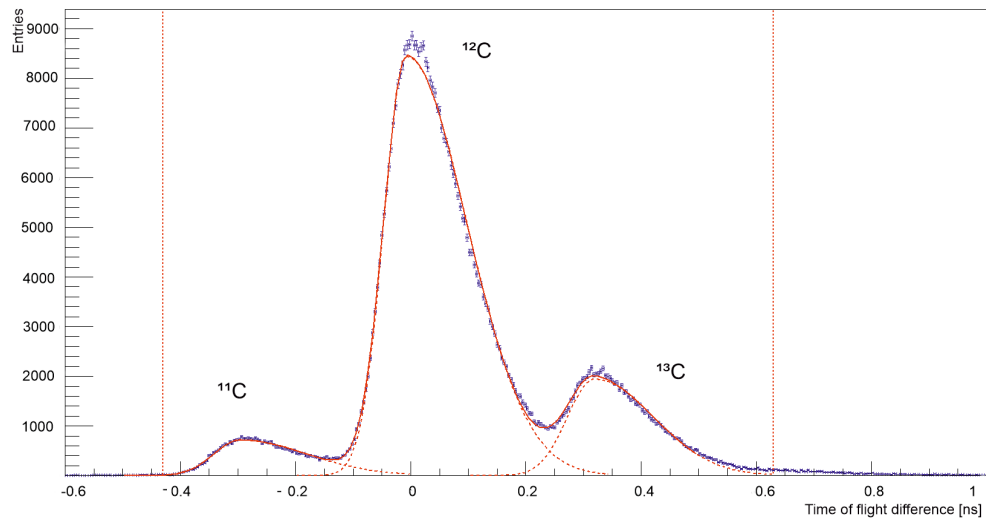
Figure 4.8: Time of flight distribution for ^{11}C, ^{12}C and ^{13}C isotopes.
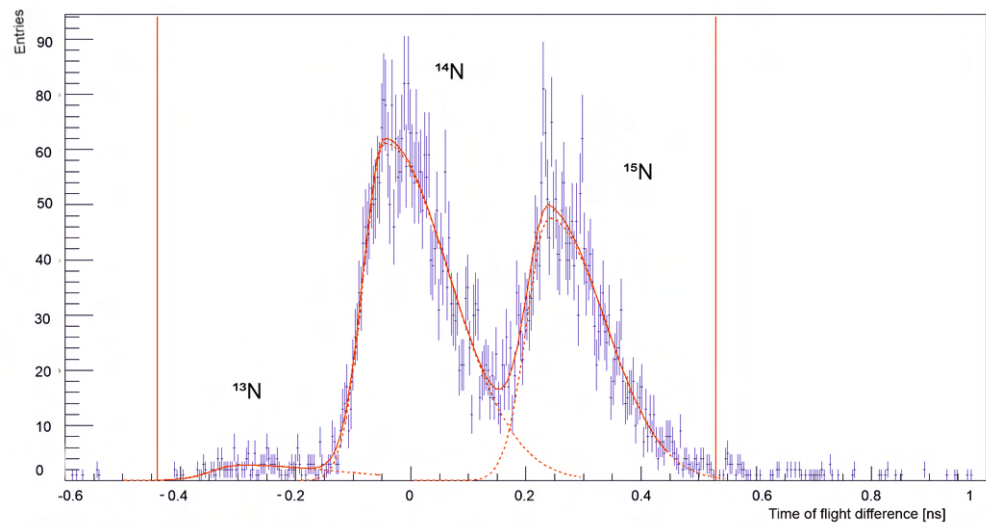
Figure 4.9: Time of flight distribution for ^{13}N, ^{14}N and ^{15}N isotopes.

Table 4.2: Beam composition - time of flight distribution fit results.

Projectile	mean [ns]	σ_L	σ_R	$3\sigma_L$	$3\sigma_R$
^{10}B	0.03	0.04	0.11	-0.09	0.35
^{11}B	0.43	0.04	0.10	0.30	0.73
^{11}C	-0.30	0.05	0.12	-0.43	0.05
^{12}C	-0.01	0.04	0.10	-0.12	0.31
^{13}C	0.32	0.05	0.10	0.18	0.63
^{13}N	-0.30	0.05	0.17	-0.44	0.22
^{14}N	-0.05	0.04	0.11	-0.15	0.29
^{15}N	0.24	0.04	0.10	0.13	0.53

The Gauss function used for fitting charge and time of flight distributions is shown in the equation 4.20.

$$f(x) = Ae^{-\frac{1}{2}(\frac{x-\bar{x}}{\sigma})^2} \tag{4.20}$$

To describe the asymmetry of sigma values, the function with logic selection was used in setting the sigma value, described in formula 4.21.

$$(x < [\bar{x}])?[\sigma_L] : [\sigma_R]) \tag{4.21}$$

The beam composition for the T1 trigger in 2D dimension (ToF vs S1 signal) is shown in figure 3.8. The beam composition for trigger T3 is shown in figure 4.10[7]. To increase statistics for boron and nitrogen analysis, additionally, data from the T3 trigger were used, as can be seen in figure 4.10 the signals from neighboring ions to carbon are also passed through the trigger discriminator. Analysis for boron and nitrogen isotopes was made with the use of the logic statement that the trigger must be T1 or T3. For boron and nitrogen, no isotope separation was made, charge changing cross-section values were calculated for the sum of $^{10}B + ^{11}B$, and for the sum of $^{13}N + ^{14}N + ^{15}N$. The cause of this decision was to not decrease statics, and according to theory and current knowledge described in 4.0.1, we would not spot the difference with low statistics and what goes with it with high statistical error. The carbon charge-changing cross section was calculated both for the sum of $^{11}C + ^{12}C + ^{13}C$ and for ^{12}C and ^{13}C separately.

The values of applied cuts for projectile type selection can be found in table 4.3. Cuts values were estimated based on fits, which results can be found in tables 4.1 and 4.2. For selecting an ion based on the signal in S1, the first cross of the fitted functions was chosen as a cut value. Then, for selected boron and nitrogen, because of big contamination from carbon, it was decided to narrow the cut from the side of the

---

[7]The Y-axis is calibrated to show the difference in time of flight according to the ^{12}C isotope as a main data-taking isotope.
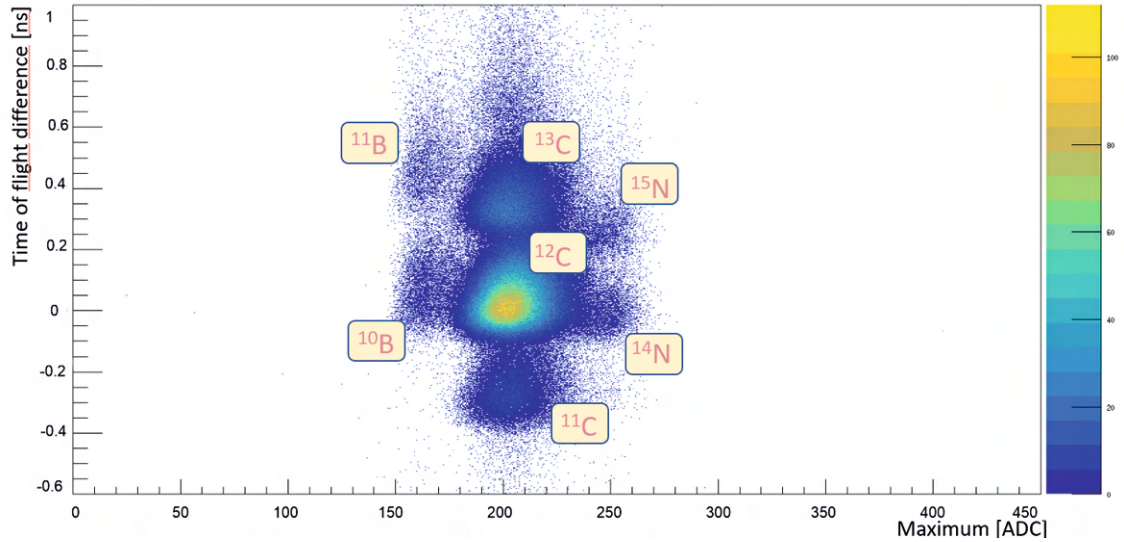
Figure 4.10: Beam composition for trigger T3, obtained by measuring S1 signal: x-axis and time of flight between A and S1 detector: y-axis.

tails neighbor with carbon[8]. To choose a new value, first Gauss function was fitted to the carbon peak in S1 signals distribution registered for the T3 trigger (which can be seen in figure A.2), then 3σ value was calculated and set as a new cut value for upper cut for boron and bottom cut for nitrogen[9]. For the time of flight, fit results from table 4.2 were used. To calculate the bottom cut, the left sigma value for the lightest isotope was taken (σ_L), and for the uppercut right sigma value (σ_R) for the heaviest isotope, was taken. Then cut value was set to 3σ from (σ_L) and (σ_R).

Table 4.3: Beam composition analysis - selected cuts.

Projectile	S1 dwon [ADC]	S1 up [ADC]	ToF down [ns]	Tof up [ns]
Boron	124.0	172.5	-0.09	0.73
Carbon	175.5	242	-0.43	0.63
Nitrogen	242.0	297.5	-0.44	0.53

---

[8]To increase the statistic for charge-changing calculation for nitrogen and boron, a combination of T3 and T1 triggers was used. The T1 trigger registered all beam particles, and the T3 trigger was set to preselect carbon ions. A big disproportion between the number of registered particles of carbon and neighboring ions causes the large contamination from carbon into the distribution of nitrogen and boron.

[9]Fit result: $\mu = 202.34$, $\sigma_L = 9.95$, $\sigma_R = 13.38$. Fitting procedure is described by equations 4.20 and 4.21

Beam analysis - ^{12}C and ^{13}C selection. Charge-changing cross-section values for carbon isotopes are calculated with the use of a pure T3 trigger. High statistics allow for isotope separation and calculation cross-section for ^{12}C and ^{13}C separately. Distribution in 2D space (ToF vs S1 signal) with marked selected cut for ^{12}C and ^{13}C are shown in figures 4.11 and 4.12.
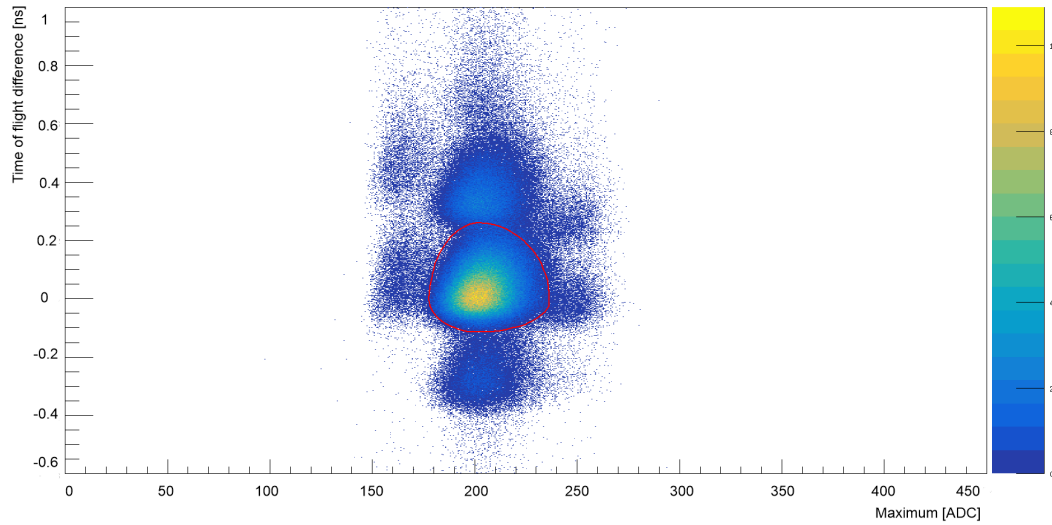
Figure 4.11: ^{12}C selection for T3 trigger.
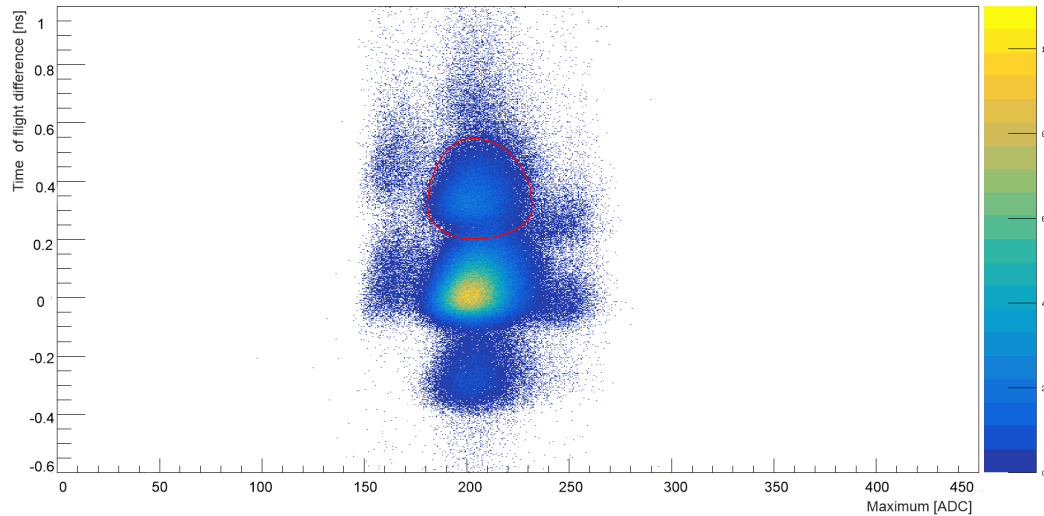
Figure 4.12: ^{13}C selection for T3 trigger.

Cut was set based on a two-dimensional Gauss function with asymmetric sigma values fitted to the wanted isotope. Then, the cut area was chosen based on the

statement that values in cutted area can not be lower than 3% of function maximum for ^{12}C and 10% of function maximum for ^{13}C. 3% and 10% values were chosen based on the efficiency and purity analysis. To calculate these values, several steps were done[10]:

- fit 2D Gauss function with asymmetric sigma values to ^{12}C peak (step 1),

- fit 2D Gauss function with asymmetric sigma values to ^{11}C and ^{13}C peaks (step 2),

- estimation parameters of the full distribution[11] of ^{10}B and ^{14}N peaks based on fit parameters from Tof vs S1 signals distribution for T1 trigger[12] (step 3),

- calculation contamination from ^{11}C and ^{13}C (based on step 2) and from ^{10}B and ^{14}N (based on step 3) for different cut values,

- analysis efficiency and purity of the ^{12}C selection for different cut values.

Histograms with fitted functions can be seen on figure 4.13 for optimization cut for ^{12}C selection, and in figure 4.14 for optimization cut for ^{13}C selection. Analogous histograms with z logarithmic scale can be seen in figures 4.15 and 4.16.
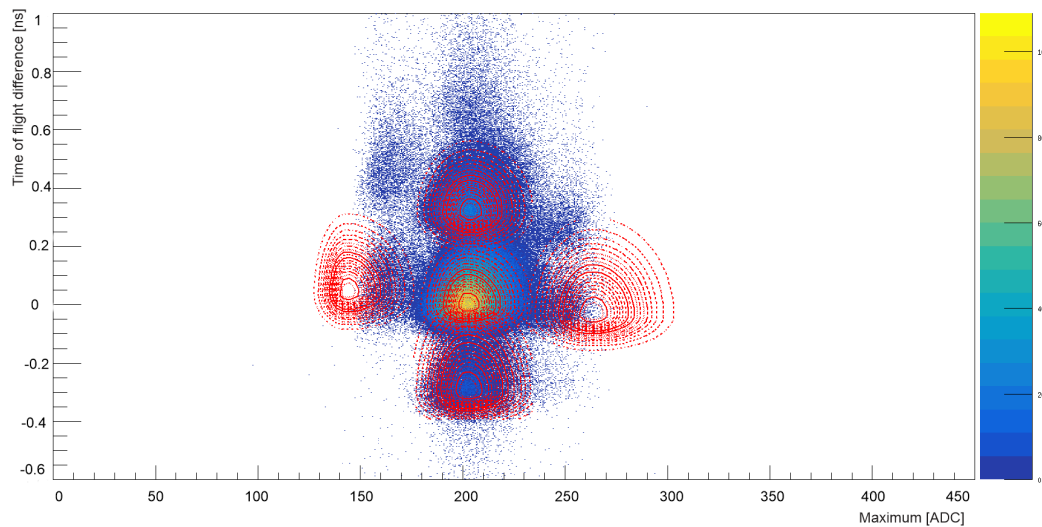
Figure 4.13: Fitted (^{12}C and ^{13}C) and estimated (^{10}B and ^{14}N) 2D Gaussian distributions for purity 4.23 and efficiency 4.22 calculations purpose.

---

[10]The procedure will be described for choosing a cut for ^{12}C selection, for ^{13}C analogous procedure was used.

[11]It is clearly visible on figure 4.11 in comparison to figure 3.8 that for T3 trigger we don't have full distribution for ^{10}B and ^{14}N peaks because T3 trigger cut most of them.

[12]Details can be found in appendix A
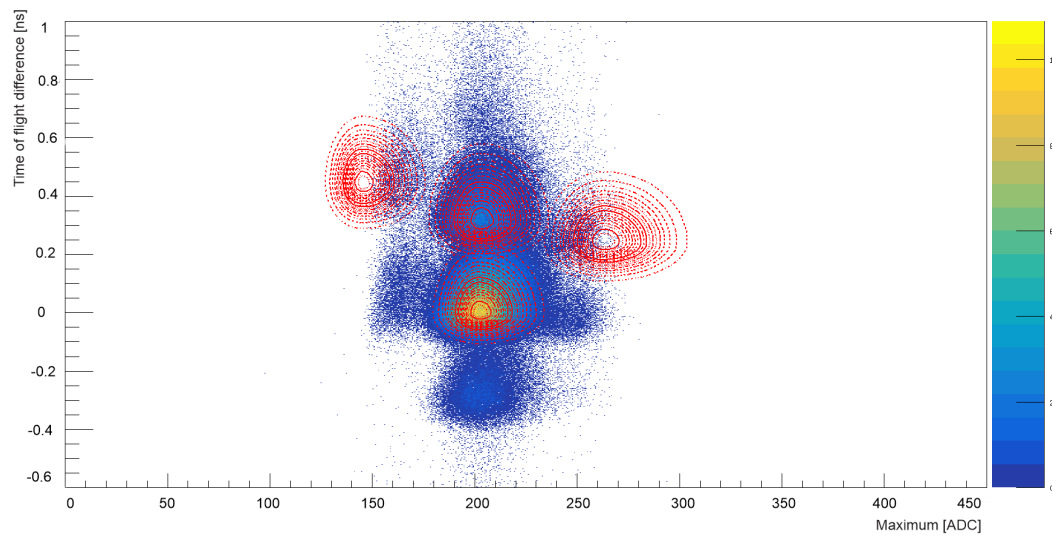
Figure 4.14: Fitted (^{12}C and ^{13}C) and estimated (^{11}B and ^{15}N) 2D Gaussian distributions for purity 4.23 and efficiency 4.22 calculations purpose.
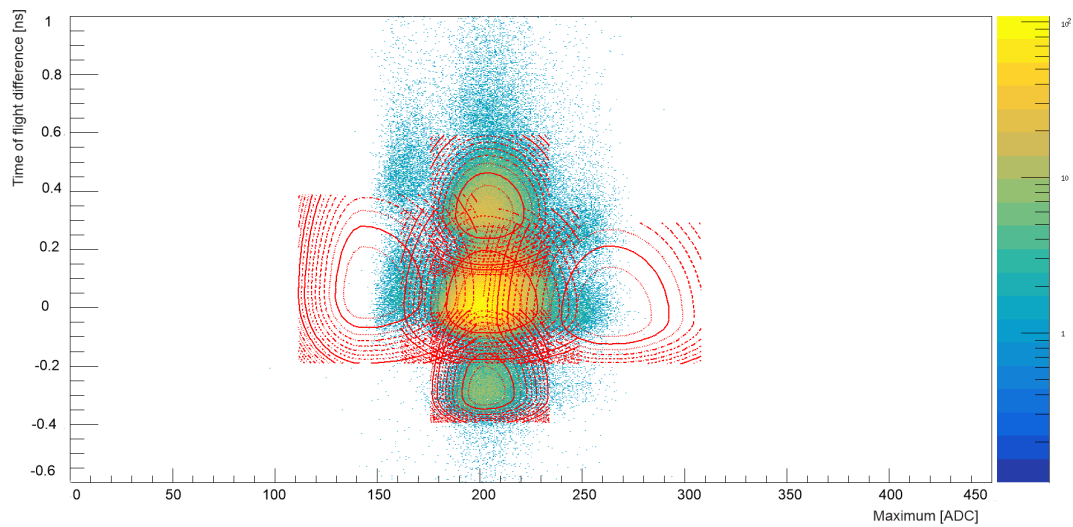
Figure 4.15: Fitted (^{12}C and ^{13}C) and estimated (^{10}B and ^{14}N) 2D Gaussian distributions for purity 4.23 and efficiency 4.22 calculations purpose. Logarithmic scale.
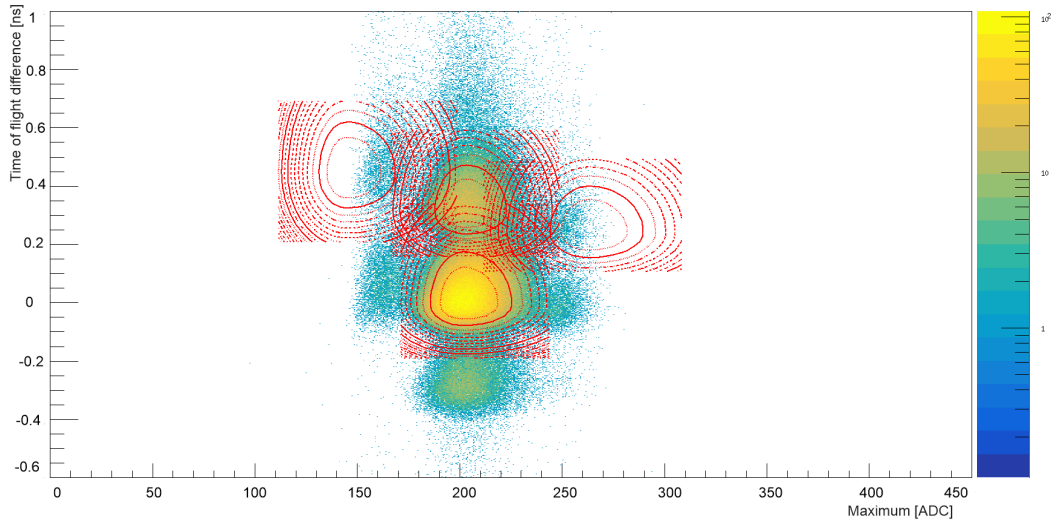
Figure 4.16: Fitted (^{12}C and ^{13}C) and estimated (^{11}B and ^{15}N) 2D Gaussian distributions for purity 4.23 and efficiency 4.22 calculations purpose. Logarithmic scale.

Efficiency and purity were calculated with the use of equations 4.22 and 4.23. Efficiency describes how much carbon we lose because of our cut. C_{cut} is the number of carbon particles in the cut range, and C_{all} describes the number of all carbon particles in a given peak[13]. Purity describes the ratio of wanted carbon particles C_{cut} in comparison to background particles from neighboring distributions B_{cut} in a given cut range[14].

$$\epsilon = \frac{C_{cut}}{C_{all}} \tag{4.22}$$

$$P = \frac{C_{cut}}{C_{cut} + B_{cut}} \tag{4.23}$$

Then, the product of purity and efficiency was plotted. The maximum of the function corresponded to minimal statistical uncertainty. Results of analysis can be seen in figure 4.17 for ^{12}C cut selection and in figure 4.18 for ^{13}C selection. On the x-axis is the checked cut value, and on the y-axis is the product of efficiency and purity.

For ^{12}C isotope function maximum corresponds to a cut value equal 3%, and this number was set as a cut. Contamination from neighboring isotopes for this value is lower than 4%. For ^{13}C isotope maximum of the function is for cut equal 6%, but because of big contamination from ^{12}C isotope purity is below 90% (p = 88%). That is why it was decided to shift the cut to value 10%, which corresponds to the area on

---

[13]Based on integrals from fitted distributions (step 1).

[14]Based on integrals from fitted distributions in a given range (step 3).

the graph 4.18 where the functions of purity and efficiency are crossing, and both are above 90% (e = 91%, p = 91%). The fraction of neighboring ions in the selected cut range can be found in table 4.4.
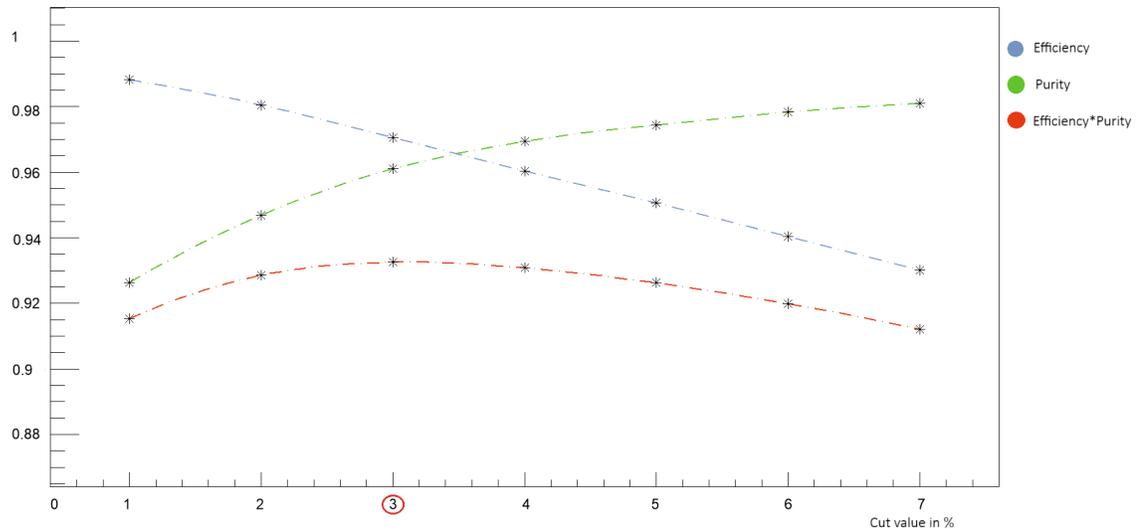
Figure 4.17: Checked cut values (x-axis) with the results of efficiency and purity calculation (y-axis), for ^{12}C selection.
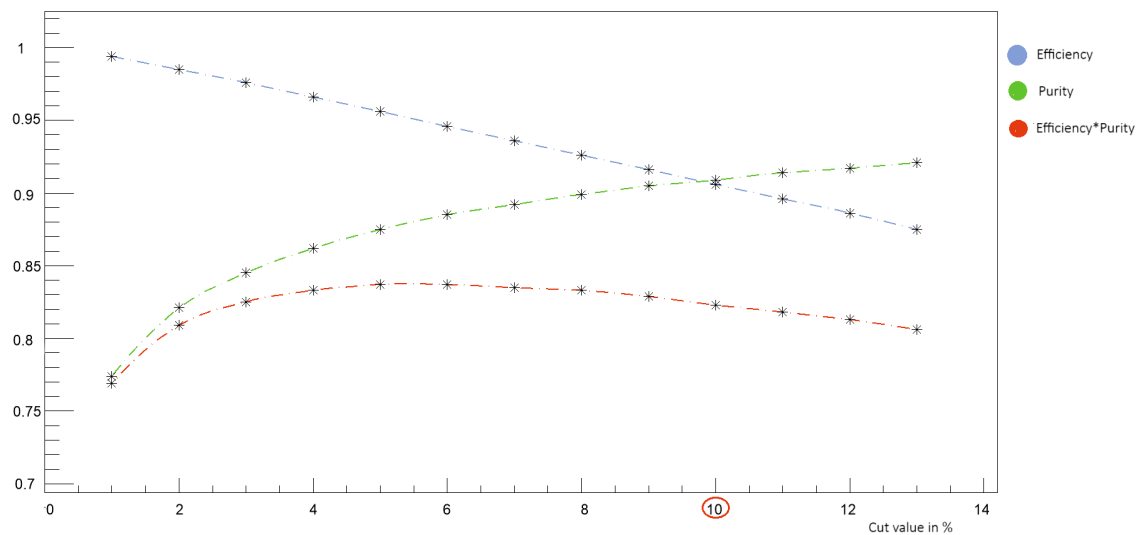
Figure 4.18: Checked cut values (x-axis) with the results of efficiency and purity calculation (y-axis), for ^{13}C selection.

2D Gauss function used for fits is described by the equation 4.24, where the method of setting the sigma value is described in equation 4.21:

$$f(x, y) = Ae^{\frac{1}{2}(\frac{x-\bar{x}}{\sigma_x})^2 - \frac{1}{2}(\frac{y-\bar{y}}{\sigma_y})^2}$$ (4.24)

Table 4.4: Relative fractions of the impurities from neighboring isotopes present in the upstream $^{12}C/^{13}C$ selection.

^{12}C selection	^{10}B: $2.5x10^{-3}$	^{14}N: $8.8x10^{-3}$	^{11}C: $1.2x10^{-2}$	^{13}C: $1.6x10^{-2}$
^{13}C selection	^{11}B: $4.6x10^{-4}$	^{15}N: $8.8x10^{-4}$	^{12}C: $8.9x10^{-2}$	

4.0.5 Upstream analysis - beam position detector alignment and cut on beam position

The (x, y) positions of the three BPD's are offset relative to each other, and the alignment procedure must be applied. To do this, the positions of BPD-1 and BPD-2 are fixed, and a linear extrapolation is performed to the position of BPD-3. Then, the position of BPD-3 is shifted according to this extrapolation. A schematic view of the procedure, as well as applied shift values in the x and y direction, can be seen in figure 4.19. Equations 4.25 and 4.26 show how position extrapolation is made, where the indexes at coordinates describe a number of BPD.

$$X_{BPD3}^{extr} = \frac{x_1 z_2 - z_1 x_2}{z_2 - z_1} + \frac{x_2 - x_1}{z_2 - z_1} z_3$$ (4.25)

$$y_{BPD3}^{extr} = \frac{y_1 z_2 - z_1 y_2}{z_2 - z_1} + \frac{y_2 - y_1}{z_2 - z_1} z_3$$ (4.26)
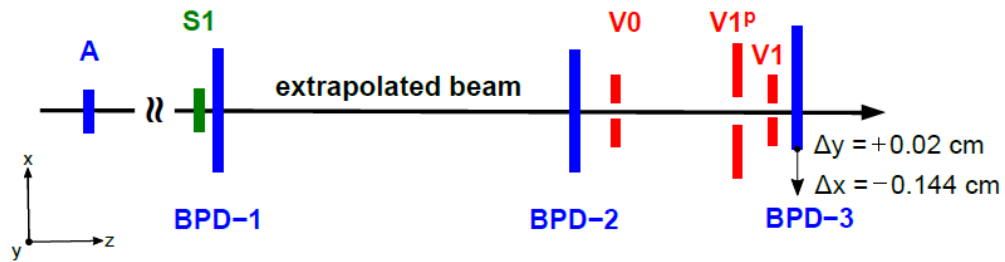
Figure 4.19: Beam position detectors alignment procedure - schematic view.

During beam position reconstruction, several statuses are assigned depending on the quality of the measurements. If, in at least two BPD's a good quality signal was presented and the fit procedure was performed with success, the beam fitted positive

status is set. Only events with this status are passed through for further analysis. Then, it needs to be checked if the beam hits the target; it could be done with the use of an x-y beam position in BPD3. The beam position measured by BPD3 can be seen in figure 4.20, as well with marked regions of the cut; all events registered out of this region are rejected. The formula used to check if the beam position is in the wanted region is shown in equation 4.27.

$$(x_{BPD3} - x_0)^2 + (y_{BPD3} - y_0)^2 < 0.8^2 \tag{4.27}$$
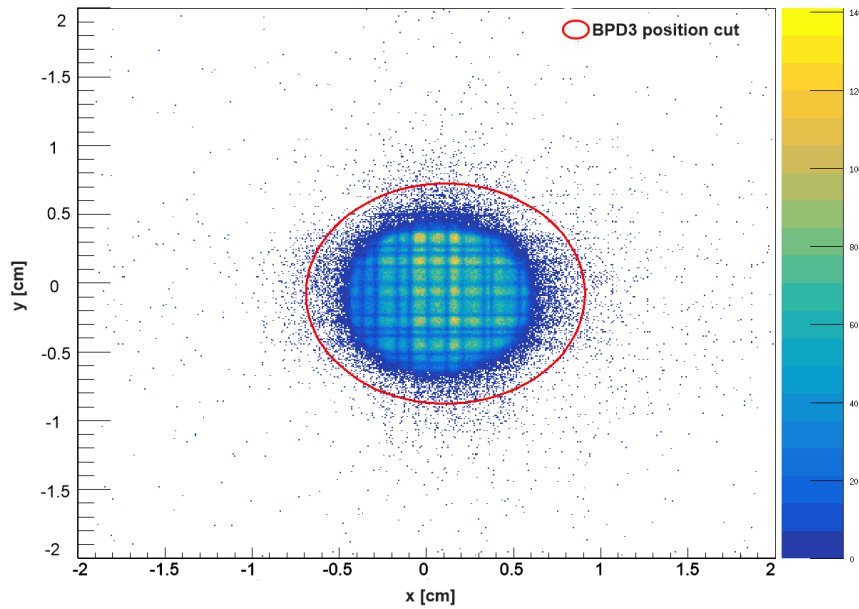
Figure 4.20: Beam position register on BPD3 - detector placed closest to the target.

4.0.6 Downstream Analysis - analysis of the products of beam interaction with the target

Time projection chambers calibration. The identification of particles in the Time Projection Chambers by their charge, momentum, and mass is carried out by measuring the energy deposited in the detector gas, which is proportional to the square of their charge, as well as by their trajectory under the influence of a magnetic field. Trajectory reconstruction involves identifying clusters in individual TPCs and then reconstructing particle flight paths from them. In the final step, paths are connected between all TPCs. During reconstruction, it is also necessary to identify whether the path comes from the interaction or whether it is detector noise or a poorly analyzed cluster. This is done by analyzing the reconstructed interaction vertex in the target.

The interaction vertex is estimated using BPDs. After reconstructing the beam tracks for each event and applying corrections from the alignment procedure, the position of the beam is extrapolated to the target, and based on this, the point of interaction is determined. Reconstructed tracks in TPCs are selected as proper fragment tracks if they have a sufficiently short distance to the main interaction vertex.

Then, the second phase of alignment is applied, which is alignment between all TPCs and extrapolated beam position. The diagram of this procedure, along with the values by which the track coordinates are shifted, is shown in figures 4.21 and 4.21.
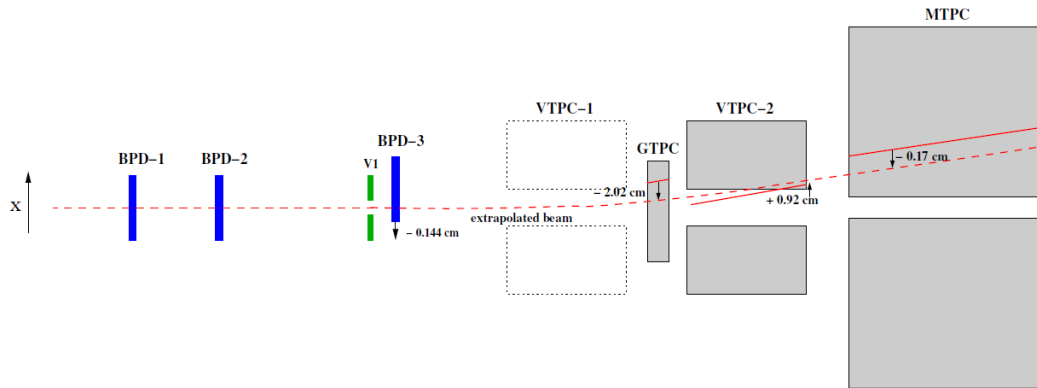
Figure 4.21: Schematic view on alignment procedure between TPC's and extrapolated beam for x-coordinates.

Charge reconstruction is made based on deposit energy measurements. Charged particles passing through the detector ionize the gas along their path. Read-out pads installed on each TPC chamber collect the stream of the free electrons drifting toward them. MTPC-L has 90 reading pads, VTPC-2 72, and GTPC 7. To gain the amplification of the signal, drifting electrons are amplified in additional electric fields, which cause electron avalanche production and intensification of the signal from each ionized electron. The solution used is based on the multi-wire proportional chambers
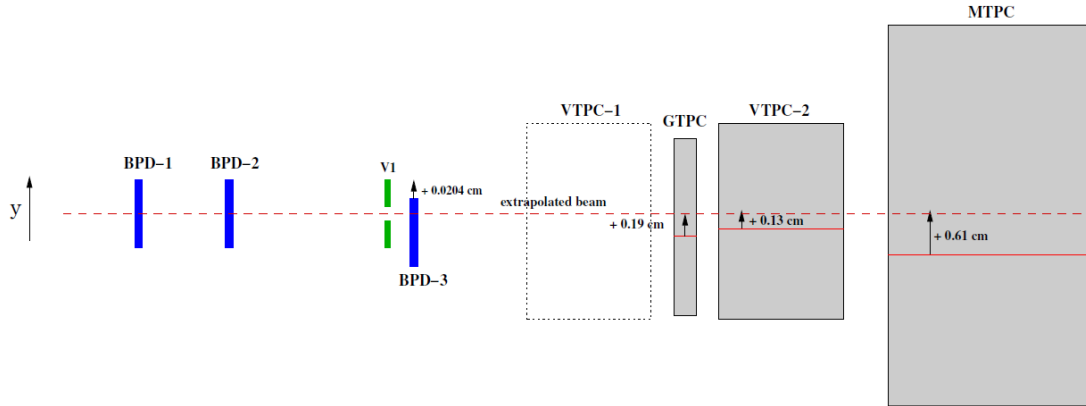
Figure 4.22: Schematic view on alignment procedure between TPC's and extrapolated beam for y-coordinates.

(MWPCs)[23]. Initially, the signal is saved in ADC units, and then during the off-line calibration process, it is calibrated to more intuitive values like energy loss in MeV/cm or the Z^2 value of the passing ion.

A histogram with particle energy loss in MTPC-L distribution is shown in figure 4.23, and an analogous histogram with energy loss values calibrated do square of the particle's charge is shown in figure 4.24. Figure 4.25 shows the 2D distribution of fragments derivation in a magnetic field (x-axis) versus Z^2 values. Derivation in a magnetic field is calibrated to utility, describing how fragments in centimeters are derived from extrapolated beam particles. All three histograms are shown for T1 trigger without a cut for the target and beam selection applied.
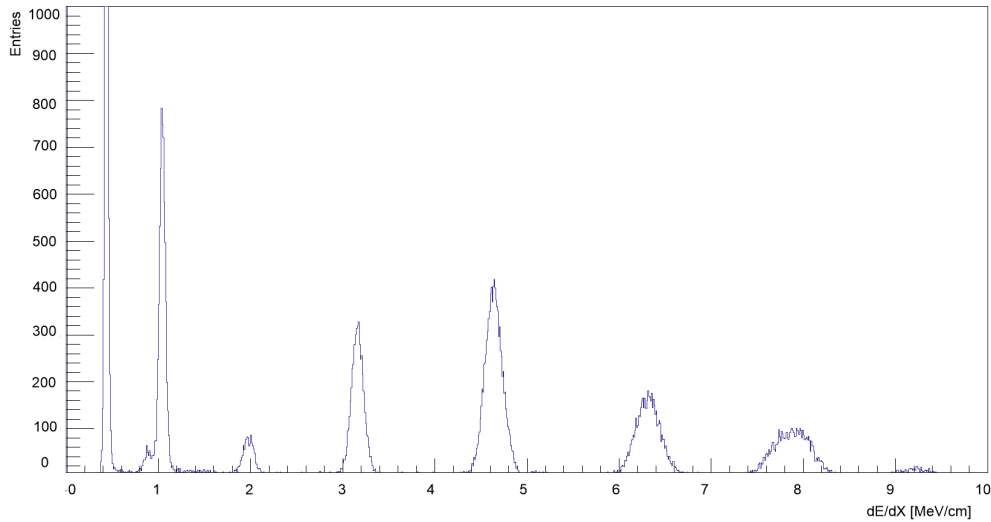
Figure 4.23: Histogram with particle energy loss in MTPC-L distribution.
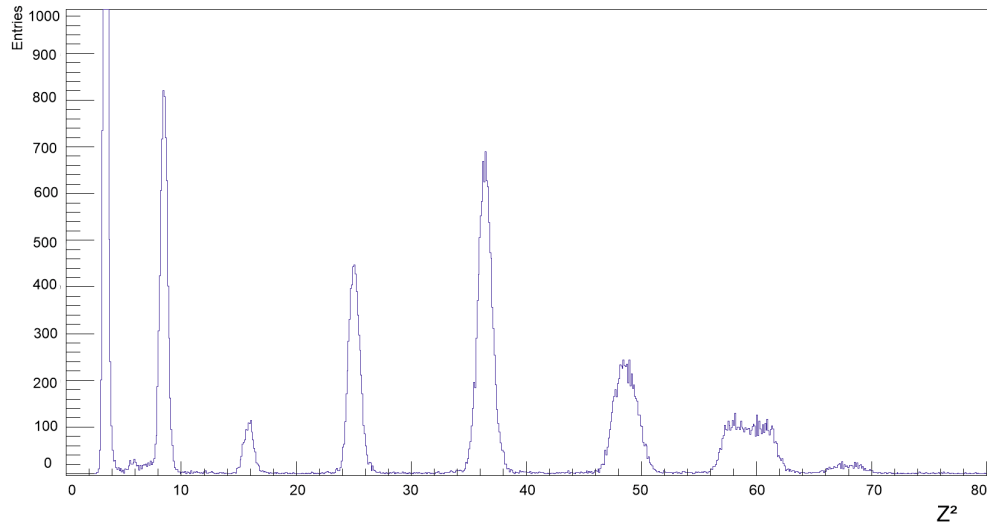
Figure 4.24: Histograms with particle energy loss in MTPC-L values calibrated to particle Z^2 value.
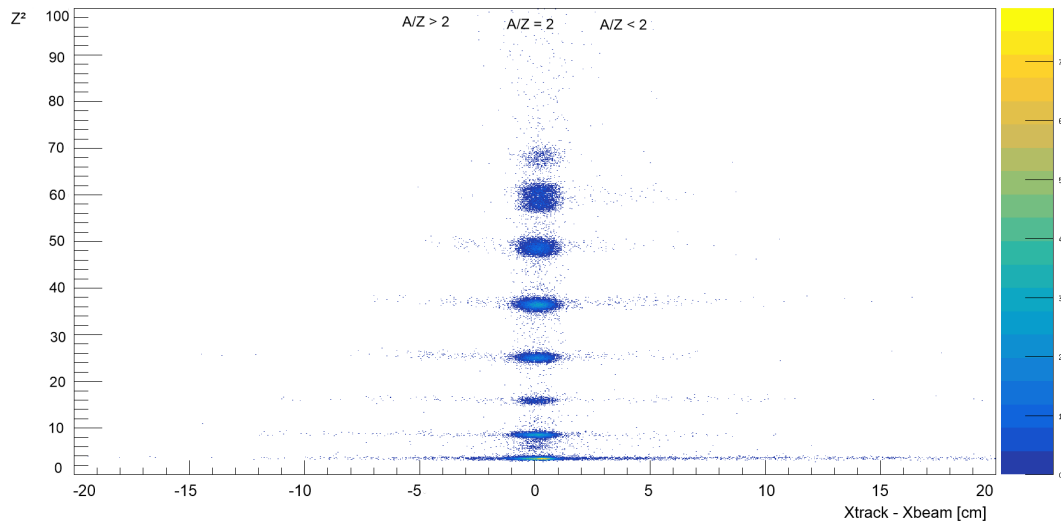
Figure 4.25: 2D distribution of particles register in MTPC-L. The x-axis represents derivation in a magnetic field; the y-axis represents Z^2 value.

Downstream analysis. Downstream analysis is meanly focused on the described quantity of beam particles leaving the target area without the interaction as is described in subsections 4.0.1 and 4.0.3. Because the calculated cross-sections are charge-changing cross-sections, no isotope separation was made in the downstream analysis. Cuts were chosen based on one-dimensional charge distribution in MTPC-L. The procedure for setting the cut value is as follows:

- beam cuts are applied to choose the beam ion for which we want to determine the cross-section for the change of charge,

- charge distribution of the produced fragments and non-interacting beam particles in MTPC-L is analyzed, and the Gaussian function is fitted to the peak corresponding to the Z^2 value of the projectile,

- sigma values are calculated, and 3σ cut is applied.

Fitted functions, as well as the chosen cut values, can be seen in figures 4.26, 4.27, 4.28 and 4.29. The type of reaction is marked on the top of each histogram. The used fitted function is the simplified Crystal Ball function [46], which is a Gaussian function with exponential tails sown in the equation 4.28. Sigma values were calculated with the use of equation 4.29, k_L and k_R are the decay constants of the exponential tails, and σ_{Gauss} is the sigma value of Gaussian core. Selected cut values and fit results are shown in table[15] 4.5.
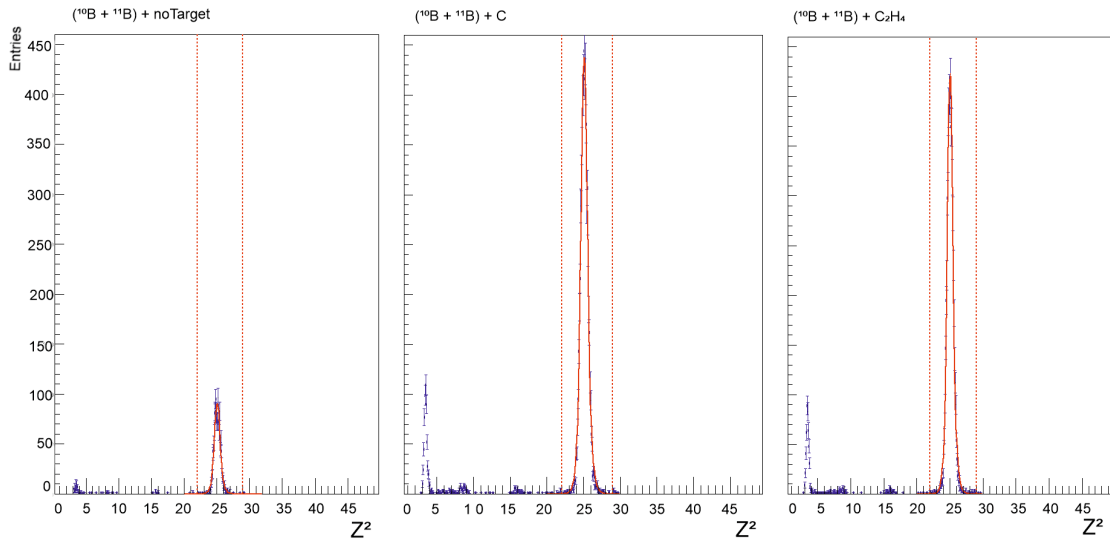
Figure 4.26: Register particles charge distribution in MTPC-L for the reaction of 13.5A GeV boron beam with the target.

---

[15]Because of the good resolution of MTPC, it was decided to broaden the 3 sigmas cut to an integer value.
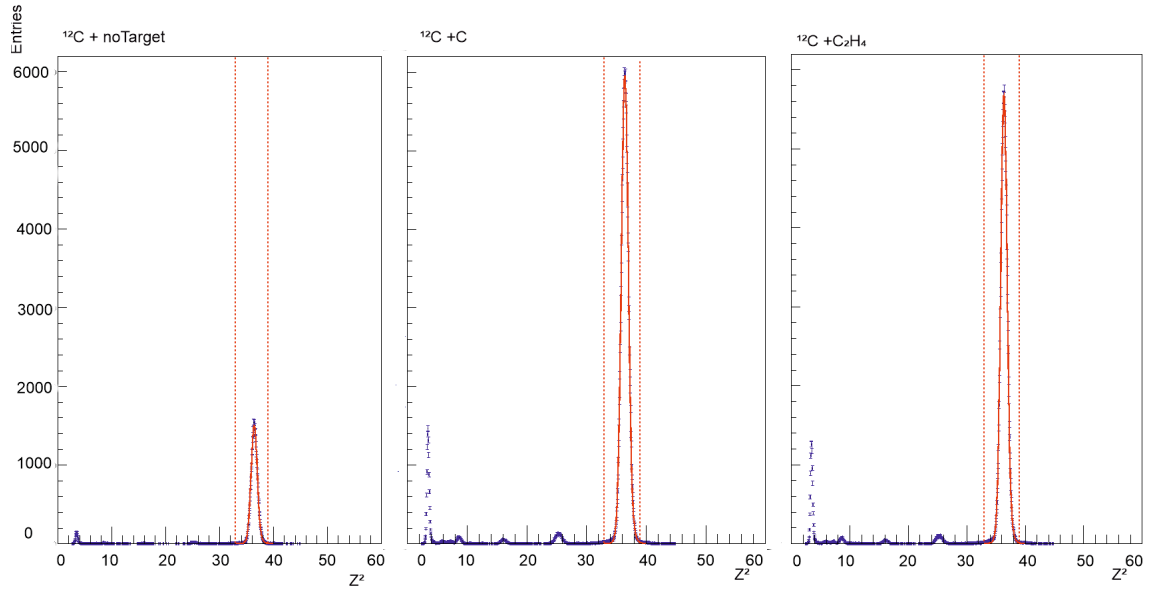
Figure 4.27: Register particles charge distribution in MTPC-L for the reaction of 13.5A GeV ^{12}C beam with the target.
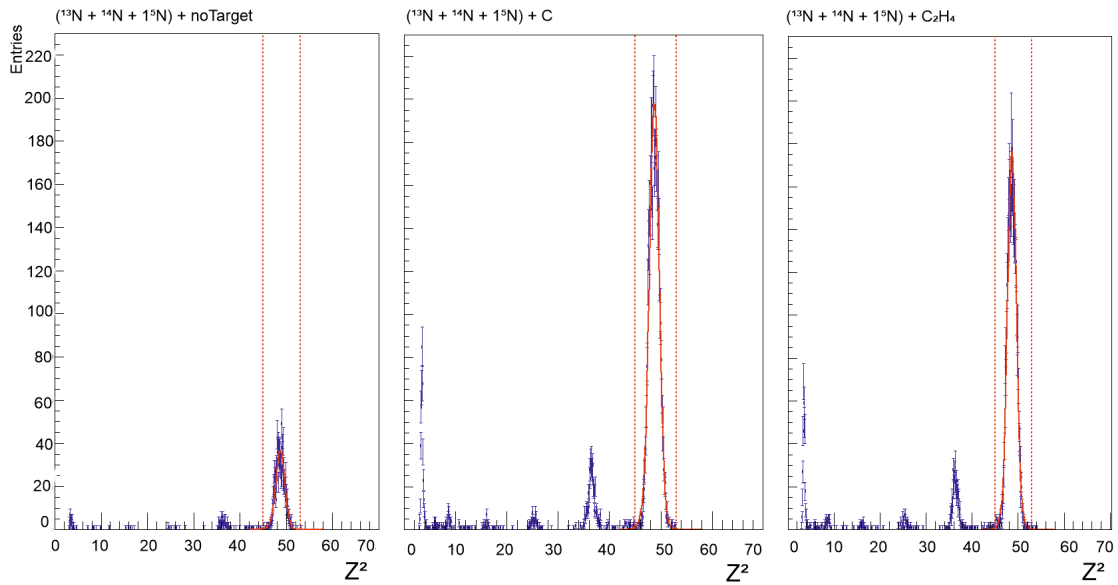
Figure 4.28: Register particles charge distribution in MTPC-L for the reaction of 13.5A GeV ^{13}C beam with the target.
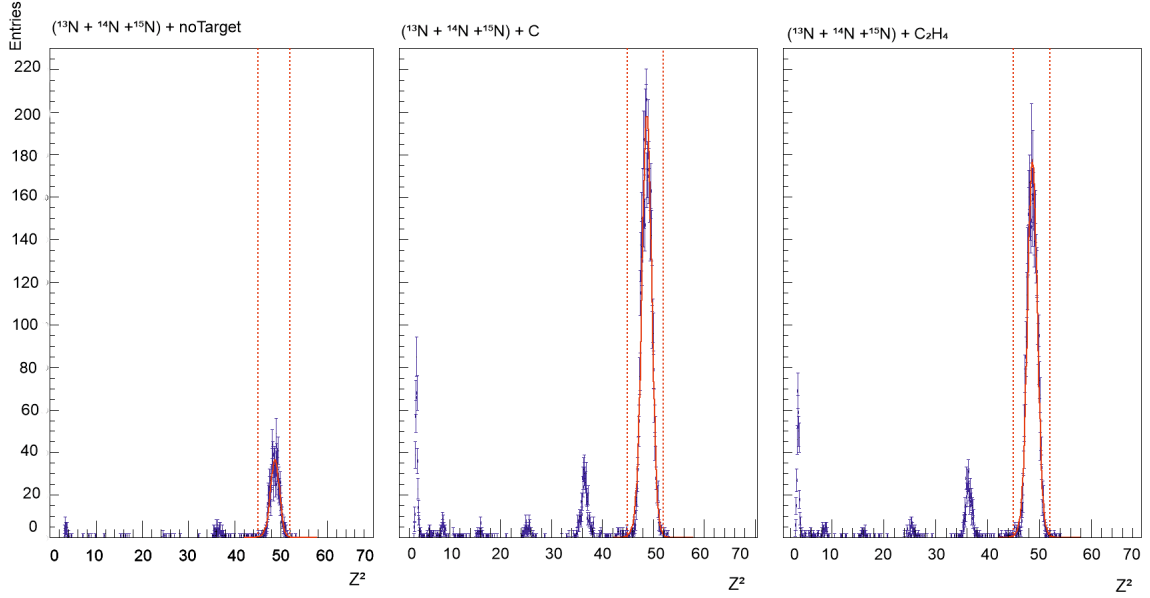
Figure 4.29: Register particles charge distribution in MTPC-L for the reaction of 13.5A GeV nitrogen beam with the target.

$$f(x; \bar{x}; \sigma; k_L; k_R) = e^{\frac{k_L^2}{2} + k_L \frac{x - \bar{x}}{\sigma}}, for \frac{x - \bar{x}}{\sigma} \leq -k_L$$

$$e^{-\frac{1}{2} \frac{x - \bar{x}}{\sigma}^2}, for -k_l < \frac{x - \bar{x}}{\sigma} \leq k_R$$

$$e^{\frac{k_R^2}{2} - k_R \frac{x - \bar{x}}{\sigma}}, for -k_R < \frac{x - \bar{x}}{\sigma} \quad (4.28)$$

$$\sigma_{left/right} = \sqrt{\sigma_{Gauss}^2 + \frac{1}{k_{L/R}^2}} \quad (4.29)$$

Table 4.5: Selected cuts values for Downstream ion selection.

Projectile	target	mean	σ_{Gauss}	k_l	k_r	σ_{left}	σ_{right}	$3\sigma_{left}$	$3\sigma_{right}$
B	out	25.05	0.44	1.39	1.28	0.84	0.90	20.87	28.90
B	C	25.08	0.46	1.38	1.21	0.85	0.94	20.93	28.71
B	C_2H_4	25.01	0.43	1.36	1.17	0.85	0.96	20.92	28.51
							cut	22	29
^{12}C	out	36.42	0.57	2.18	1.79	0.73	0.80	34.02	33.83
^{12}C	C	36.46	0.59	2.15	1.74	0.75	0.82	33.99	38.93
^{12}C	C_2H_4	36.39	0.55	2.04	1.68	0.74	0.81	33.95	38.83
							cut	33	39
^{13}C	out	36.18	0.58	2.25	1.85	0.73	0.79	33.79	38.56
^{13}C	C	36.22	0.59	2.11	1.61	0.76	0.86	33.65	38.80
^{13}C	C_2H_4	36.14	0.56	2.06	1.64	0.74	0.83	33.66	38.62
							cut	33	39
N	out	48.69	0.98	1.51	2.27	1.18	1.07	45.15	51.91
N	C	48.72	0.97	1.66	2.13	1.14	1.07	45.30	51.94
N	C_2H_4	48.63	0.95	1.74	1.96	1.11	1.08	45.30	51.87
							cut	45	53

2D distributions of register particles in MTPC-L derivation in a magnetic field (x-axis) versus Z^2 values for a given projectile fragmentation reaction with carbon, polyethylene, and no target insert are shown in figures: (4.30, 4.31, 4.32) for boron isotopes, (4.33, 4.34, 4.35) for ^{12}C isotope, (4.36, 4.37, 4.38) for ^{13}C isotope, (4.39, 4.40, 4.41) for nitrogen isotopes.

One additional upstream cut was made based on the analysis of particles charge distribution registered in MTPC-L. The analysis takes into account whether (after the beam selection cut is applied) the distribution of charge recorded in MTPC-L contains a peak with a charge higher than the charge of the selected beam ion. If so, it means that the beam in the selected cut range is contaminated with ions with a higher charge. Such cases were removed from the analysis by adding an additional condition that after applying the selected beam cut, it is checked whether the signal registered in MTPC-L does not correspond to the charge of the neighboring ion with a higher Z. These help to achieve the purest beam cut. Cuts as marked as horizontal red lines on 2D MTPC-L distributions.
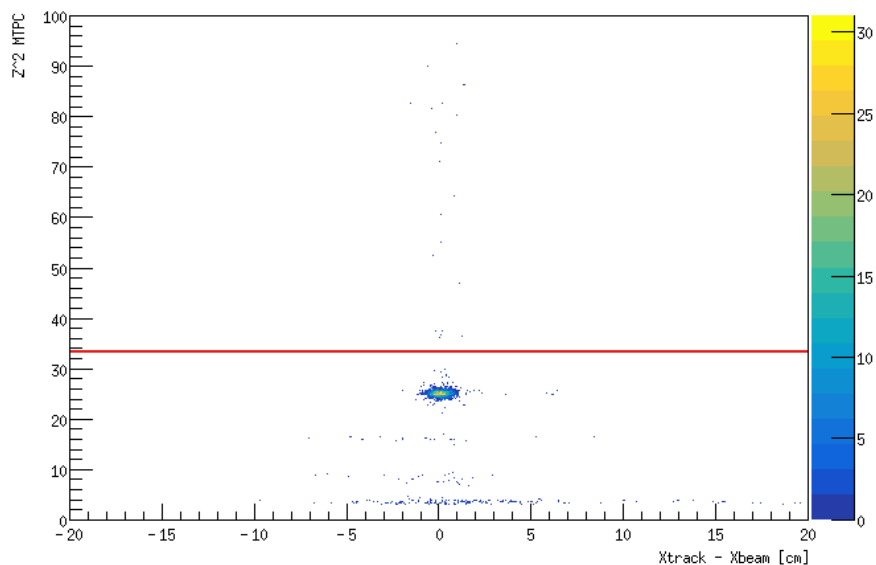
Figure 4.30: Two-dimensional distributions of particles charge versus deviation in magnetic filed register in MTPC-L after a $(^{10}B +^{11} B)$ fragmentation reaction on C target.
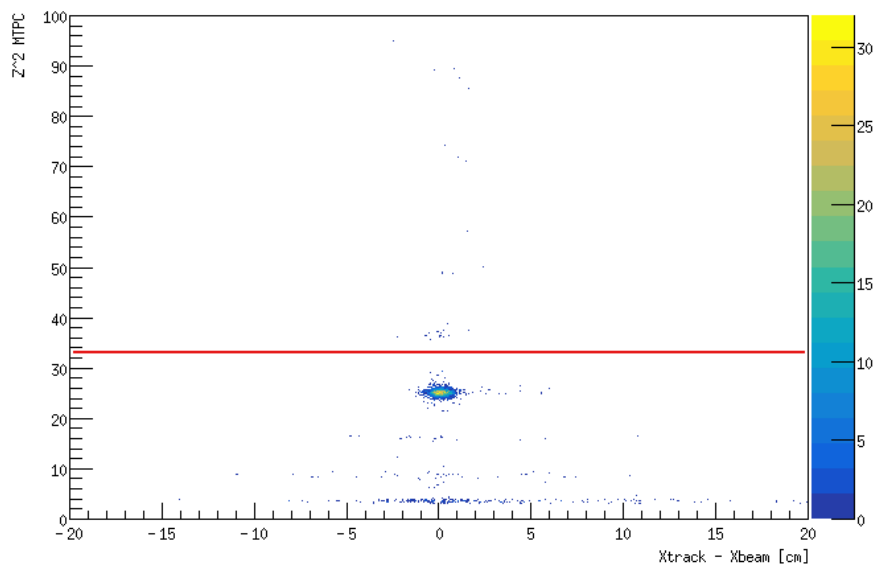
Figure 4.31: Two-dimensional distributions of particles charge versus deviation in magnetic filed register in MTPC-L after a $(^{10}B +^{11} B)$ fragmentation reaction on C_2H_4 target.
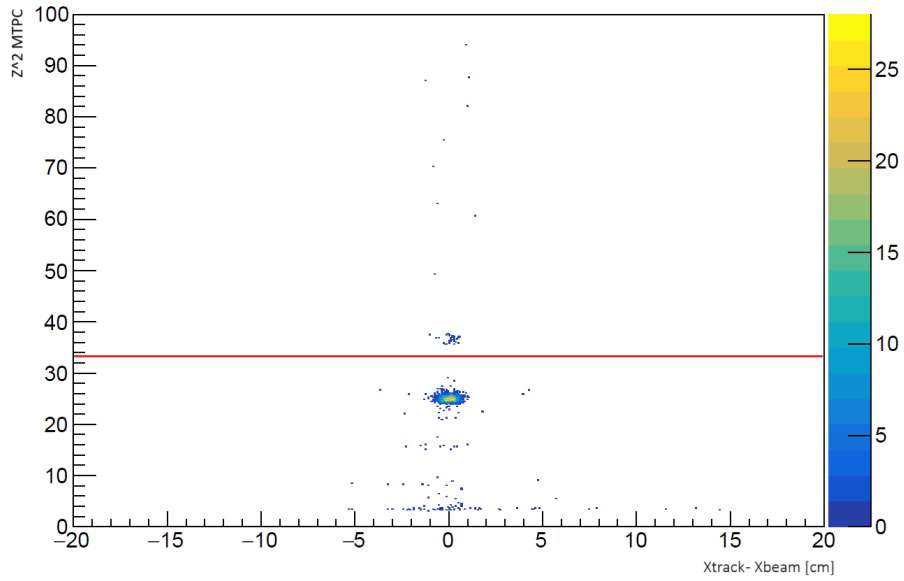
Figure 4.32: Two-dimensional distributions of particles charge versus deviation in magnetic filed register in MTPC-L for $(^{10}B + ^{11}B)$ selected as a projectile, without target insert.
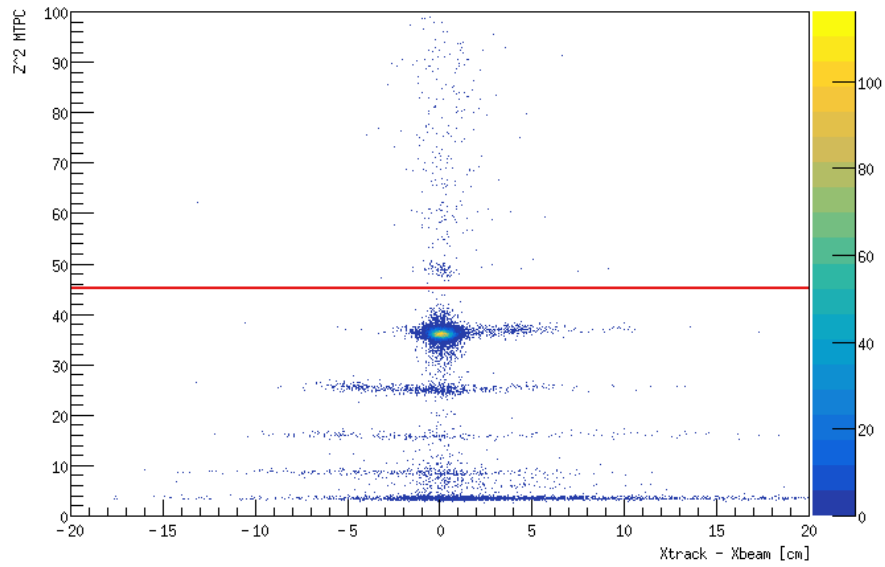
Figure 4.33: Two-dimensional distributions of particles charge versus deviation in magnetic filed register in MTPC-L after a $12C$ fragmentation reaction on C target.
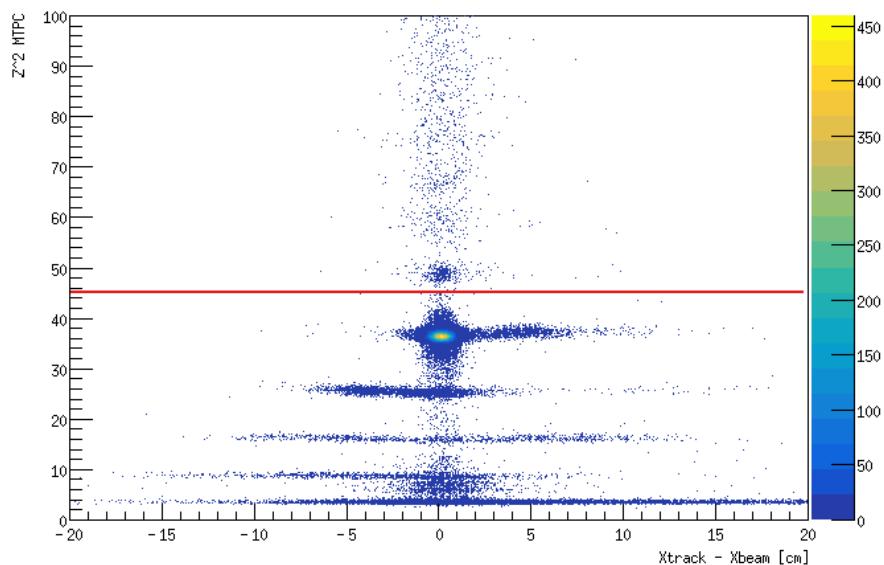
Figure 4.34: Two-dimensional distributions of particles charge versus deviation in the magnetic filed register in MTPC-L after a ^{12}C fragmentation reaction on C_2H_4 target.
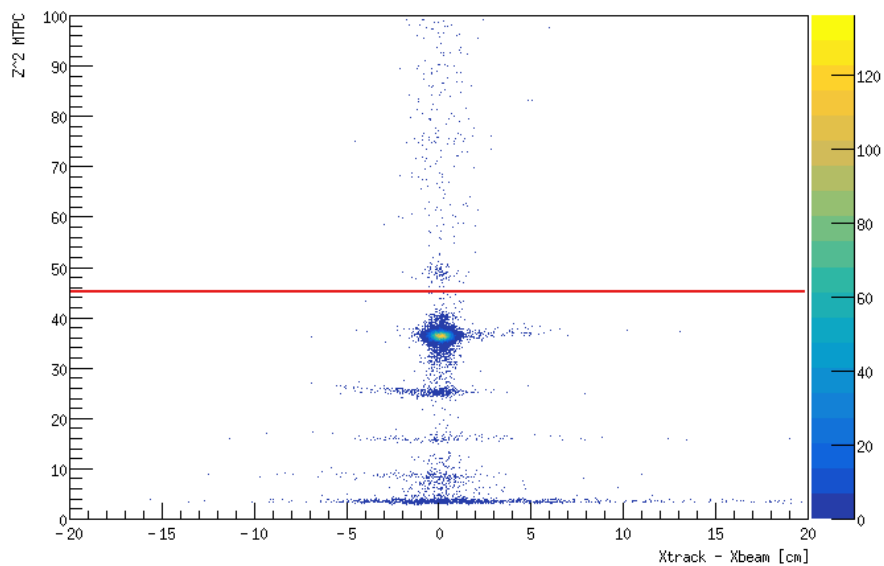
Figure 4.35: Two-dimensional distributions of particles charge versus deviation in the magnetic filed register in MTPC-L for ^{12}C selected as a projectile, without target insert.
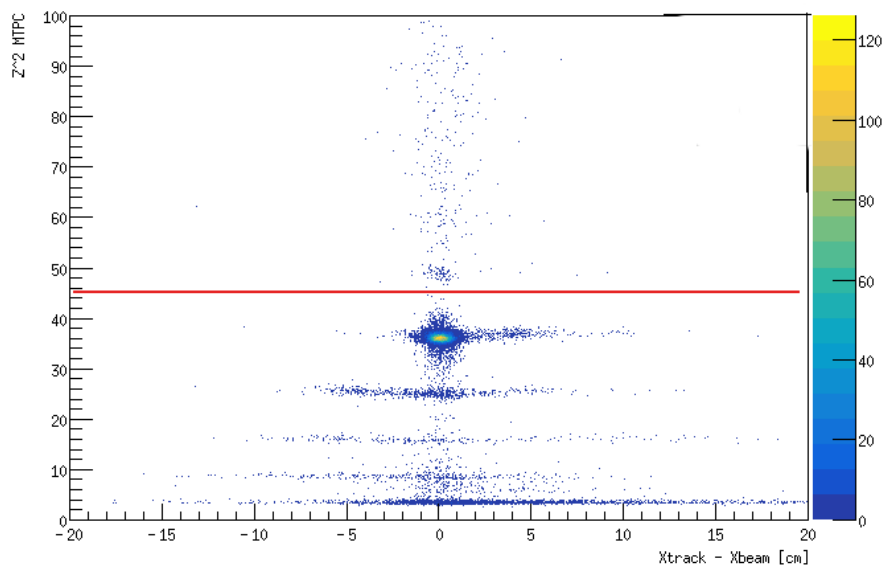
Figure 4.36: Two-dimensional distributions of particles charge versus deviation in the magnetic filed register in MTPC-L after a ^{13}C fragmentation reaction on C target.
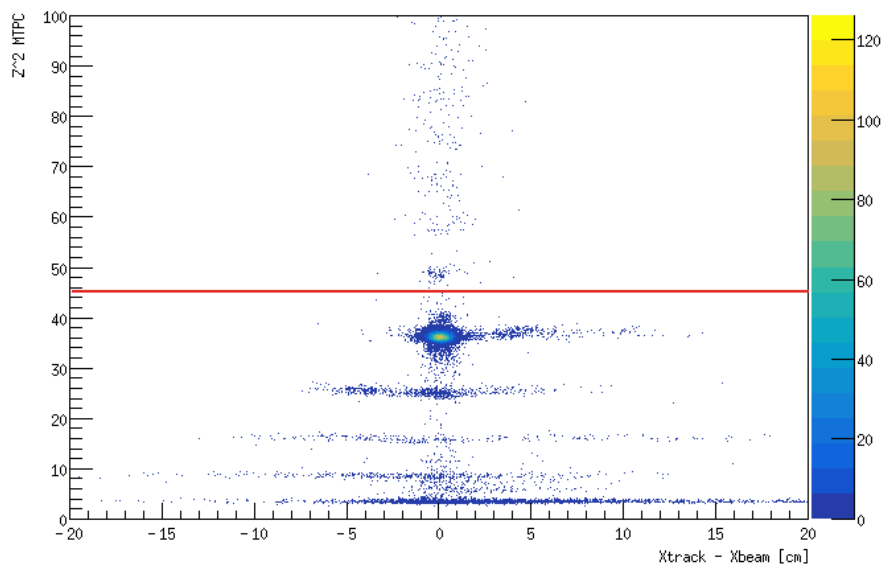
Figure 4.37: Two-dimensional distributions of particles charge versus deviation in the magnetic filed register in MTPC-L after a ^{13}C fragmentation reaction on C_2H_4 target
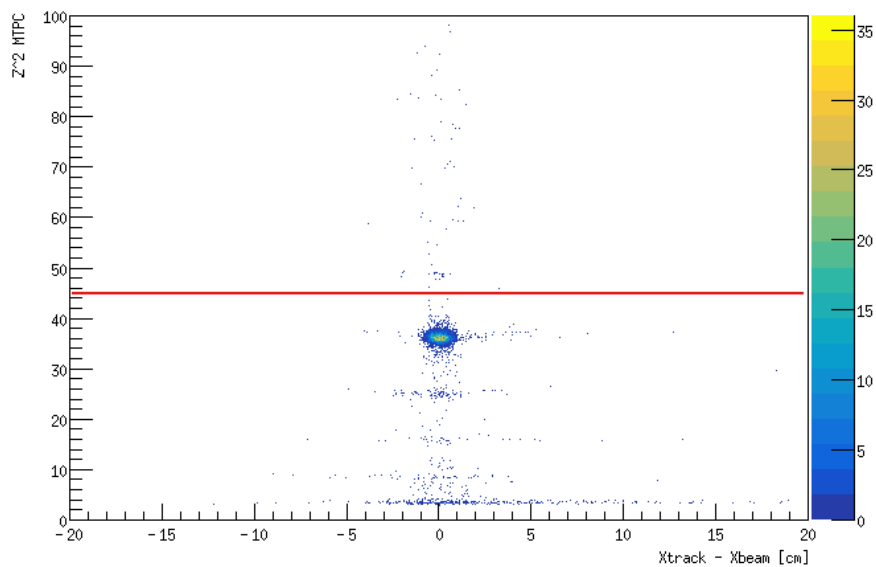
Figure 4.38: Two-dimensional distributions of particles charge versus deviation in the magnetic filed register in MTPC-L for ^{13}C selected as a projectile, without target insert.
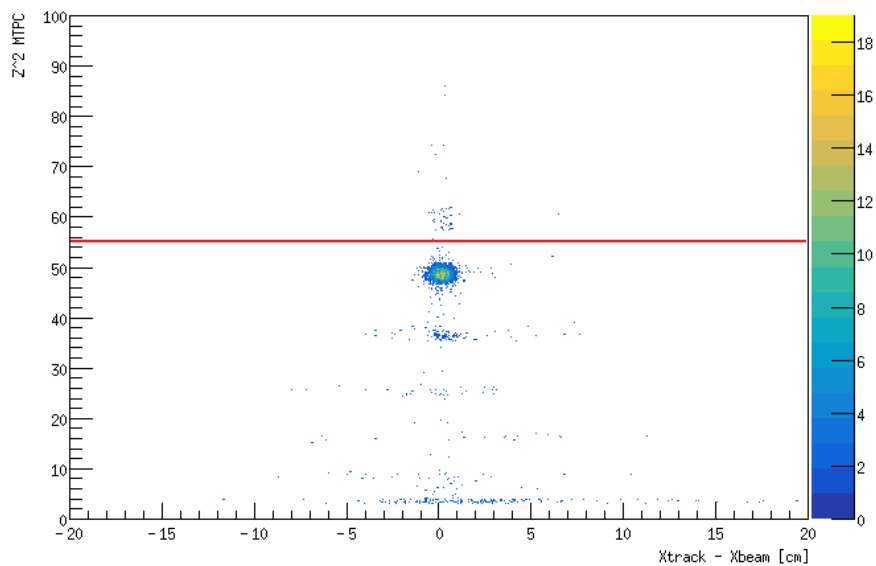
Figure 4.39: Two-dimensional distributions of particles charge versus deviation in the magnetic filed register in MTPC-L after a $\left(^{13}N +^{14}N +^{15}N\right)$ fragmentation reaction on C target.
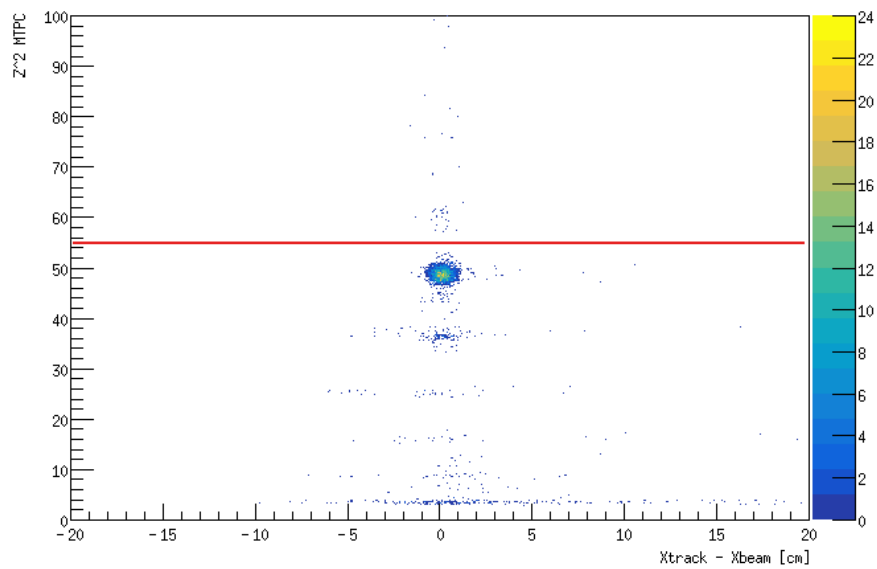
Figure 4.40: Two-dimensional distributions of particles charge versus deviation in the magnetic filed register in MTPC-L after a $^{13}N +^{14}N +^{15}N$ fragmentation reaction on C_2H_4 target
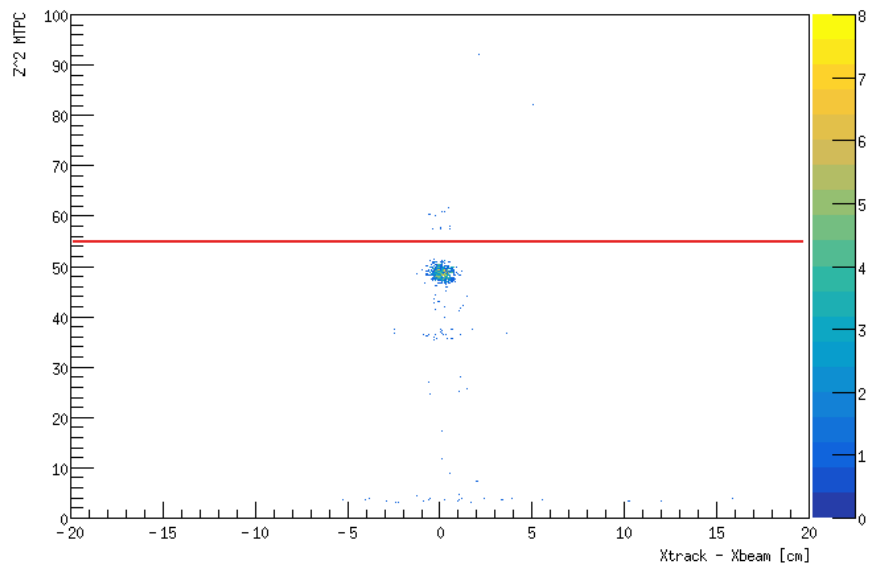
Figure 4.41: Two-dimensional distributions of particles charge versus deviation in magnetic filed register in MTPC-L for $\left(^{13}N +^{14}N +^{15}N\right)$ selected as a projectile, without target insert.

Summary of the upstream and downstream cuts:
Upstream cuts

- signal in S1 detector - charge identification,

- time of flight - isotope identification,

- beam position - positive status of the fitted track,

- beam position - check if the beam hit the target,

- off particle analysis - particles arriving closer in time than 2 µs are rejected[16],

- comparison of signal in S1 and MTPC-L if $Z^2_{MTPC-L} > Z^2_{S1}$ signal is rejected - contamination from neighboring ion.

Downstream cuts

- Z^2 in MTPC-L - charge identification,

- deflection in magnetic field - $\Delta x(x_{tack} - x_{beam}) < \pm 20 cm$[17],

- number of reconstructed clusters on track > 50, to reduce track with a small number of reconstructed clusters and track with wrongly reconstructed path,

- off particle analysis - $\Delta y(y_{tack} - y_{beam}) < \pm 5cm$ - particles arriving in different time window then readout time are rejected. Distinguish is made by time measurements of the drifting electrons along the y-direction.

A Histogram with the number of clusters on track reconstructed in MTPC-L distribution for each projectile can be seen in figure 4.42[18]

---

[16]Measured by Waveform Analyzer (WFA). Cut prevents counting beam particles arriving closer in time than 2μ, this can cause wrong track assignment in MTPC.

[17]x_{track} - reconstructed track, x_{beam} - extrapolated beam track.

[18]With no target cut applied.
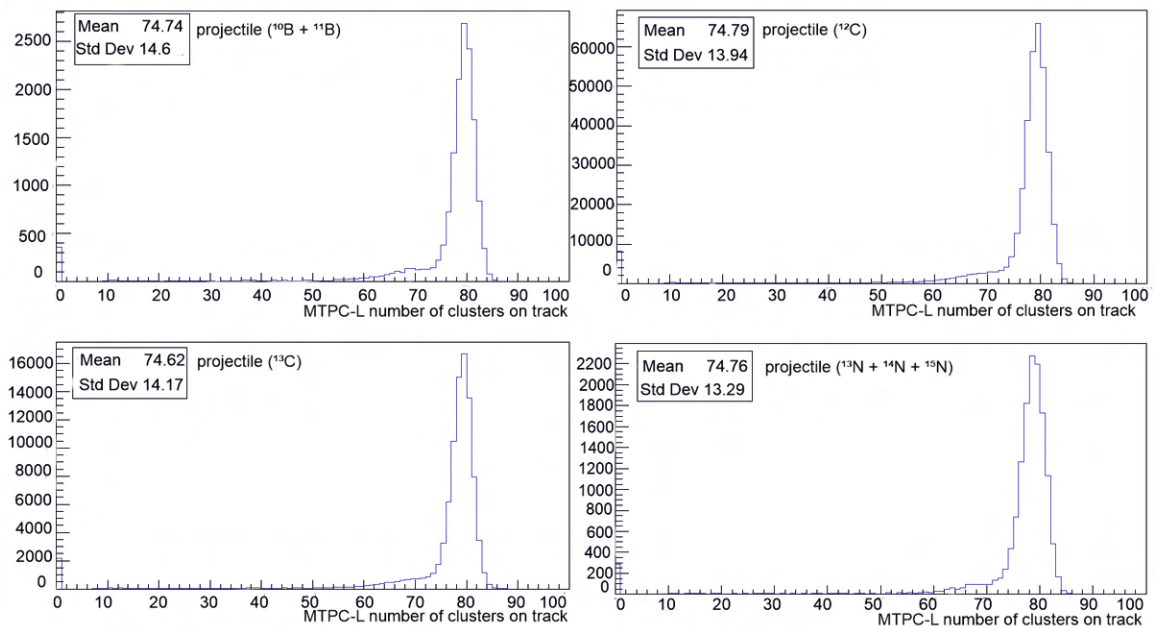
Figure 4.42: Number of clusters on track reconstructed in MTPC-L distributions for each projectile.

Chapter 5

Charge-changing cross-sections: results of the analysis

Charge-changing cross sections are calculated with the use of the formula 4.6. For each target, the formula is given by equations 5.1 (carbon target) and 5.2 (polyethylene target).

$$\sigma_{A+C->X} = -\frac{ln(1 - P_{A+C->X})}{n_C d_C} \tag{5.1}$$

$$\sigma_{A+C_2H_4->X} = -\frac{ln(1 - P_{A+C_2H_4->X})}{n_{C_2H_4} d_{C_2H_4}} \tag{5.2}$$

The charge-changing cross-section for the interaction with the proton is calculated from cross-section values for interaction with the carbon and polyethylene target 5.3. The first one is used as a source of ion-carbon interactions, and the second one is the main target for studying ion-proton interaction. Factor 2 in the denominator comes from the fact that the ratio in every polymer cell of the polyethylene target is equal to C:H=1:2.

$$\sigma_{A+p->X} = \frac{\sigma_{A+C_2H_4->X} - \sigma_{A+C->X}}{2} \tag{5.3}$$

Results of the calculation can be found in the table 5.1. For each reaction, the following steps were made:

- applying upstream cut for wanted ion selection,

- applying downstream cuts to calculate the number of beam particles that left the target area without the interaction,

- probability of interaction with the target calculation,

- calculation of the probability of interaction with detector material with the use of run without target insert (target-out),

55

61:1553302856

- calculates the probability of interaction corrected by target-out probability,

- cross-section calculations with use of formula 4.6.

The described procedure can be seen in the form of the iconography in figure 5.1.
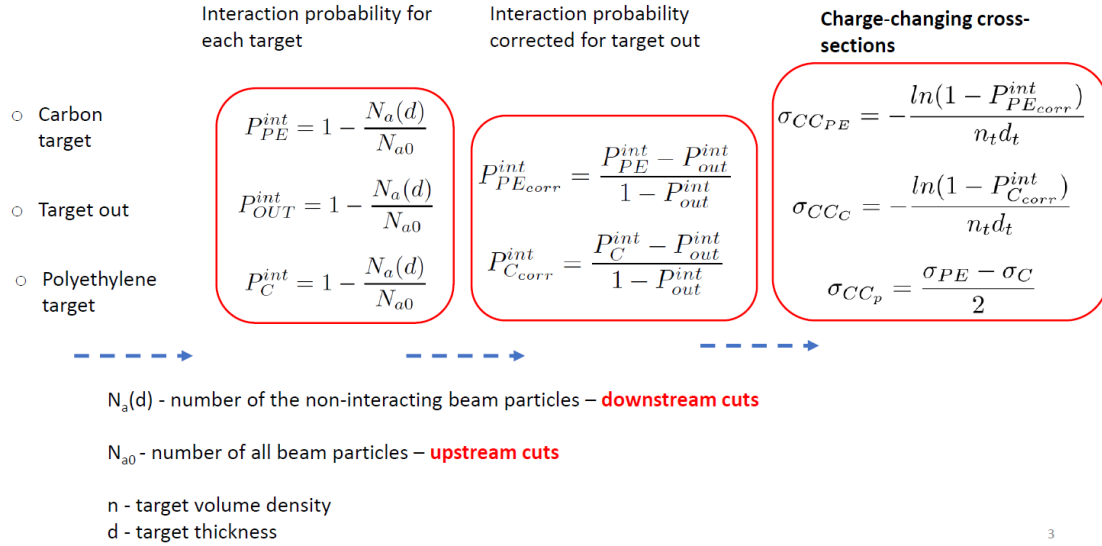
Figure 5.1: Workflow of the analysis. C is the carbon target, PE polyethylene target, and OUT corresponds to no target insert.

Figures 5.2, 5.3, 5.4 show the results of analysis. The title of the chart indicates which target the reaction relates to. The results of this analysis are marked as a blue dot; for each result, statistical error is also shown. Results are compared with two simulations Glissando[47] and Geant4[48]. The parameters used in the simulation can be found in the appendix B. Figure 5.5 shows charge-changing cross-sections for two isotopes of carbon (^{12}C and ^{13}C) and for the sum of all carbon isotopes present in beam ($^{11}C+^{12}C+^{13}C$) as above for three types of targets. Calculated charge-changing cross-section as well as statistical error for each cross-section are shown in the table 5.1. The number of beam events N_a and non-interacting particle $N_a(d)$ as well interaction probabilities for each projectile reaction with carbon/polyethylene target and no target data can be found in table 5.2[1].

Cross-section statistical errors were calculated with the use of the error propagation method: $\Delta\sigma_{A+p}$ is calculated with the use of equation 5.6, $\Delta\sigma_{A+C}$ is calculated with the use of equation 5.4 and $\Delta\sigma_{A+C_2H_4}$ with the use off 5.5. The uncertainty corrected for the target out data P_c^T in equations 5.4, 5.5 was calculated with the use of a formula 5.7. The uncertainty for each probability (target-in/target-out) $P_{int}^{T/OUT}$ in equation 5.6 and in equation 5.7 is calculated with the use of formula 4.13.

---

[1]The name of the projectile without specific mass number corresponds to beam without isotope separation.

$$\Delta\sigma_{A+C} = \sqrt{(\frac{\partial\sigma_{A+C}}{\partial P_c^C} * \delta P_c^C)^2} \qquad (5.4)$$

$$\Delta\sigma_{A+C_2H_4} = \sqrt{(\frac{\partial\sigma_{A+C_2H_4}}{\partial P_c^{C_2H_4}} * \delta P_c^{C_2H_4})^2} \qquad (5.5)$$

$$\Delta\sigma_{A+p} = \sqrt{(\frac{\partial\sigma_{A+p}}{\partial P_{int}^C} * \delta P_{int}^C)^2 + (\frac{\partial\sigma_{A+p}}{\partial P_{int}^{CH_2}} * \delta P_{int}^{C_2H_4})^2 + (\frac{\partial\sigma_{A+p}}{\partial P_{int}^{OUT}} * \delta P_{int}^{OUT})^2} \qquad (5.6)$$

$$\delta P_c^T = \sqrt{(\frac{\partial P_c^T}{\partial P_{int}^T} * \delta P_{int}^T)^2 + (\frac{\partial P_c^T}{\partial P_{int}^{OUT}} * \delta P_{int}^{OUT})^2} \qquad (5.7)$$
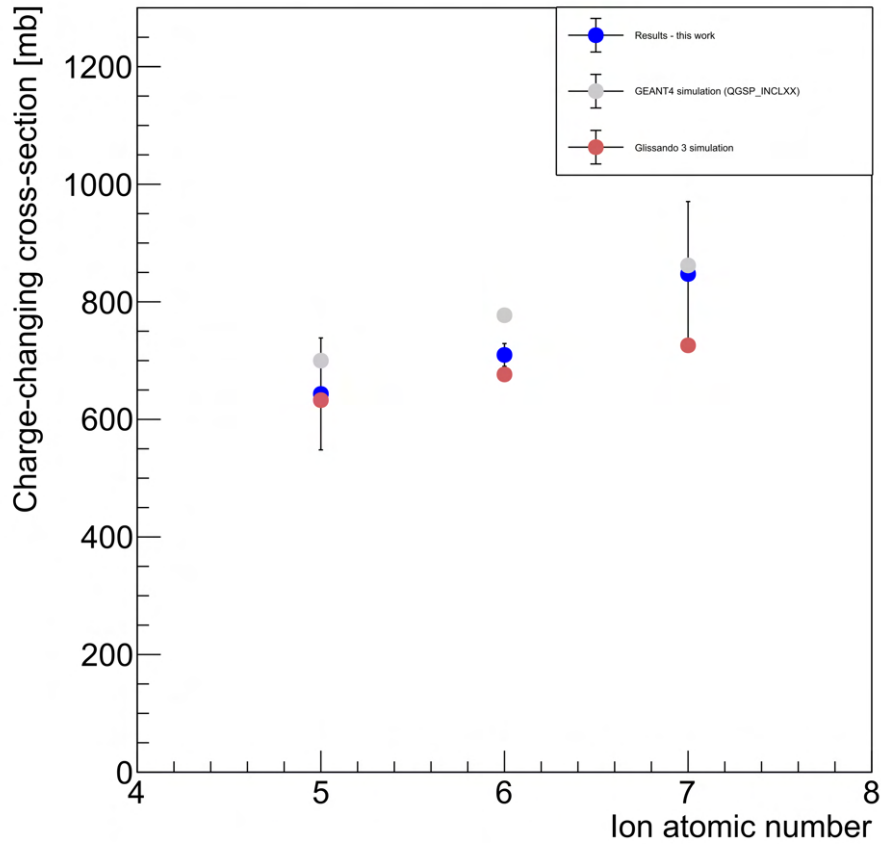
Figure 5.2: Charge-changing cross-section and statistical error values for fragmentation process of 13.4A GeV beam ions with a carbon target.
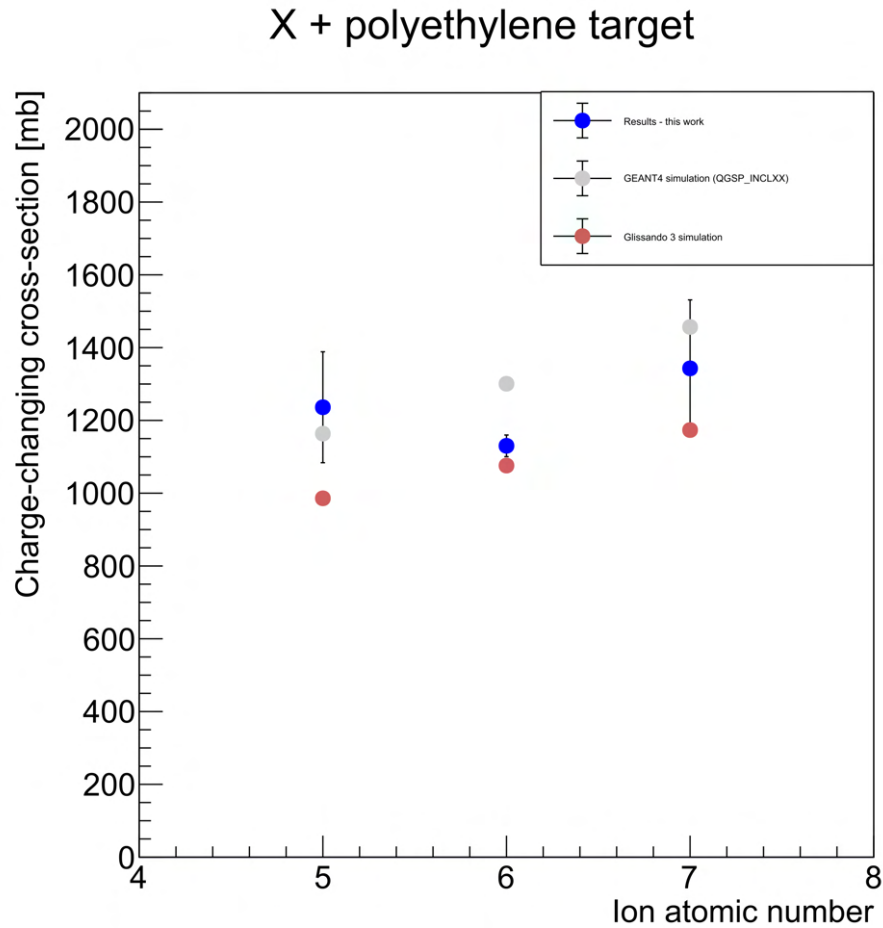
Figure 5.3: Charge-changing cross-section and statistical error values for fragmentation process of 13.4A GeV beam ions with polyethylene target.

Table 5.1: Charge-changing cross-section results of the analysis. If no mass number is specified, then the result is for the sum of all isotopes present in the beam.

beam ion	X + C σ [mb]	$\Delta\sigma$ [mb]	X + C_2H_4 σ [mb]	$\Delta\sigma$ [mb]	X + p σ [mb]	$\Delta\sigma$ [mb]
Boron	643.32	95.20	1236.14	152.39	296.41	58.54
Carbon	716.88	16.81	1149.88	25.76	216.50	9.62
Carbon (^{12}C)	709.65	19.38	1130.16	29.66	210.25	11.09
Carbon (^{13}C)	741.02	39.24	1191.22	60.19	225.10	22.39
Nitrogen	847.38	123.19	1342.97	188.16	247.80	70.30
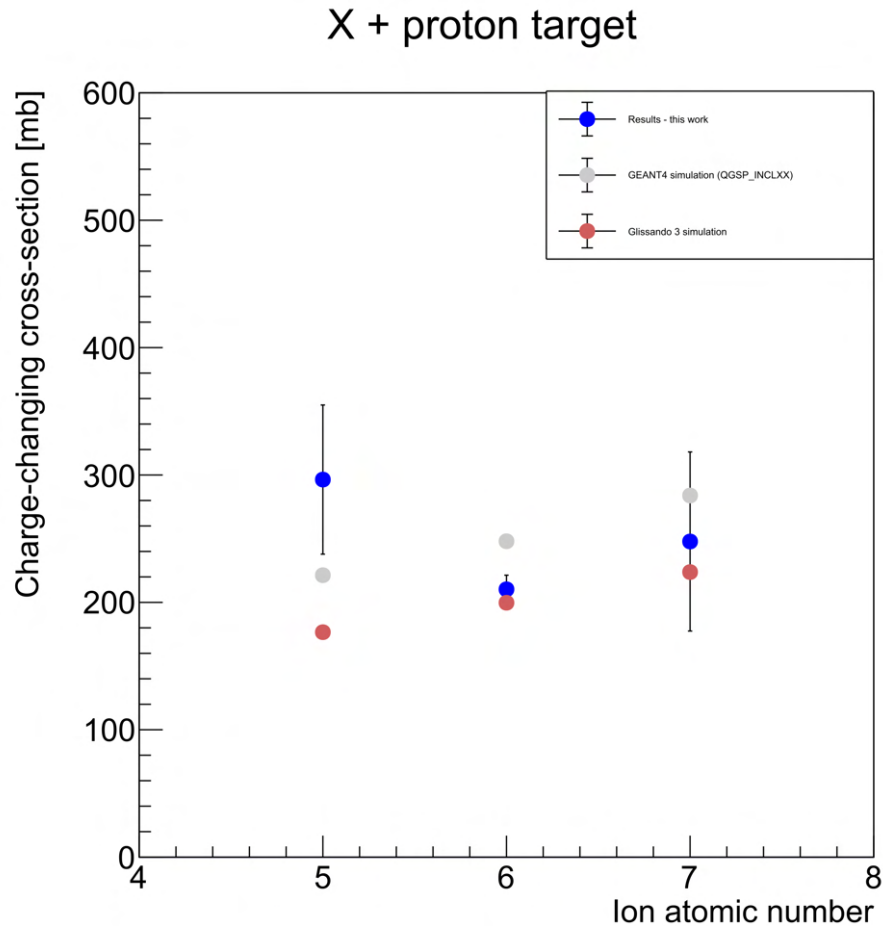
Figure 5.4: Charge-changing cross-section and statistical error values for fragmentation process of 13.4A GeV beam ions with proton target.

Figure 5.5: Charge-changing cross-section and statistical error values for carbon (^{12}C and ^{13}C) and for the sum of all carbon isotopes present in beam ($^{11}C+^{12}C+^{13}C$).

5.0.1 Discussion of the results.

The following section will discuss the results obtained and compare them with the outcomes of the GEANT4 and GLISSANDO 3 simulations. Additionally, the charge-changing cross-section for fragmentation of ^{12}C beam will be compared with an independent analysis of the same data set [28].

Results of this work are marked as blue dots on figures 5.6, 5.7, and 5.8, results from the independent analysis are marked as yellow triangles. Both calculations are in good agreement which confirms the use of a good data analysis method. As regards the simulation, the obtained results are in good agreement with both simulations within the limits of statistical error. The result for reaction

$\left(^{13}N+^{14}N+^{15}N\right)+\text{T}\rightarrow(\text{X}<7)^2$ are the most deviated from the rest of the data and from the growing trend of cross-section value along with increase with mass number of the projectile and slightly exceed the statistical error range; new measurements with higher statistic will allow for the correction of this value.

As mentioned, there is very limited data for measurements of charge-changing cross-sections at energies above 1A GeV; therefore, future measurements from the NA61/SHINE experiment can make a significant contribution to filling this gap. New measurements with high statistics will allow for a more accurate study of isospin-dependencies of the charge-changing cross-section of carbon isotopes. The results presented in this work proved that NA61/SHINE is able to carry out this type of measurement with high quality 5.5. A new high statistic study will allow for the collection of more data for the fragmentation process of ^{11}C and ^{13}C isotopes, which in case ^{13}C significantly reduce statistical error and in case ^{11}C allow for calculation of ^{11}C charge-changing cross-section, which wasn't done yet.

Table 5.2: The number of beam events N_a and non-interacting particle $N_a(d)$ as well interaction probabilities for each projectile reaction with carbon/polyethylene target and interaction probability with detector material (no target insert - OUT).

		C_2H_4	C	OUT	$P_{int}^{C_2H_4}$	P_{int}^{C}	P_{int}^{OUT}	$P_{C}^{C_2H_4}$	P_{C}^{C}
boron									
N_{a0}		6883	6185	1649	0.1515	0.1394	0.0867	0.0710	0.0576
$N_a(d)$		5840	5323	1506	±0.0047	±0.0044	±0.0069	±0.0084	±0.0083
carbon									
N_{a0}		237378	212969	54299	0.1504	0.1485	0.0902	0.0662	0.0640
$N_a(d)$		201668	181349	49400	±0.0007	±0.0008	±0.0012	±0.0014	±0.0015
nitrogen									
N_{a0}		6734	5877	1492	0.2055	0.2040	0.1394	0.0768	0.0751
$N_a(d)$		5350	4678	1284	±0.0049	±0.0053	±0.0090	±0.0104	±0.0105
^{12}C									
N_{a0}		172862	155069	39839	0.1464	0.1448	0.0869	0.0651	0.0634
$N_a(d)$		147559	132609	36375	±0.0009	±0.0009	±0.0014	±0.0017	±0.0017
^{13}C									
N_{a0}		43328	39139	9737	0.1495	0.1473	0.0870	0.0685	0.0661
$N_a(d)$		36850	33372	8890	±0.0017	±0.0018	±0.0029	±0.0033	±0.0034

---

[2]Where T is a target, comment refers to the reaction with polyethylene and proton.
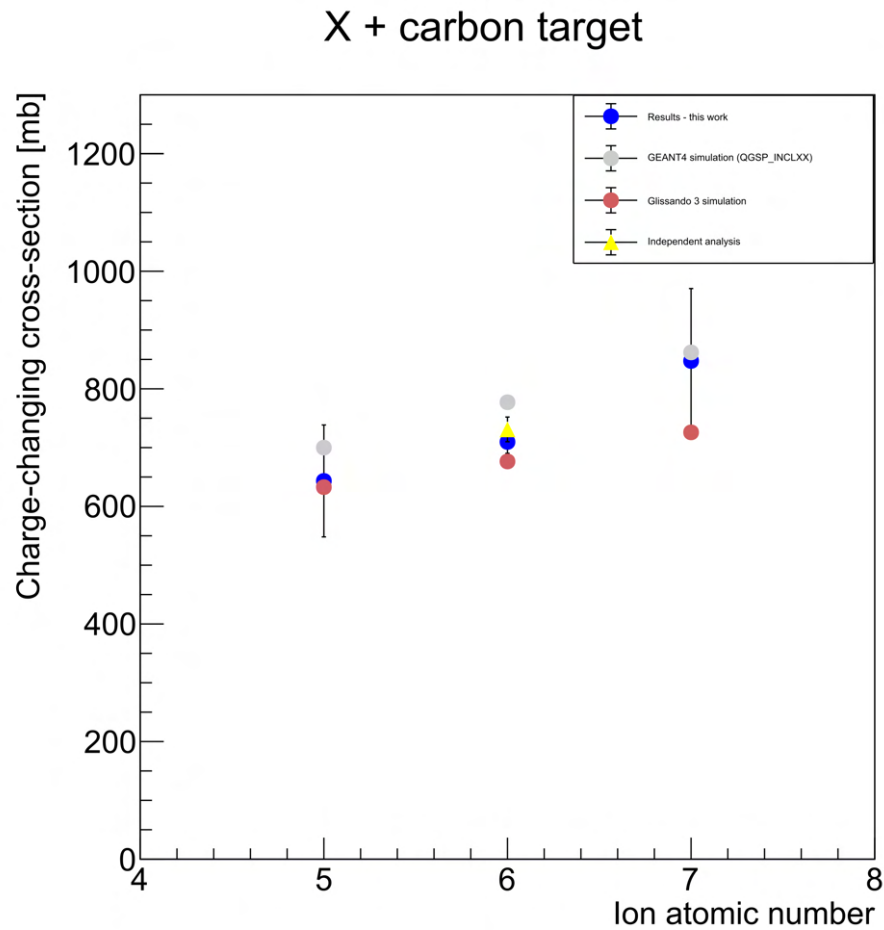
Figure 5.6: Charge-changing cross-section for fragmentation process of 13.4A GeV beam particles with a carbon target. Comparison with GEANT4 and GLISSANDO3 simulation and for ^{12}C with independent analysis [28].
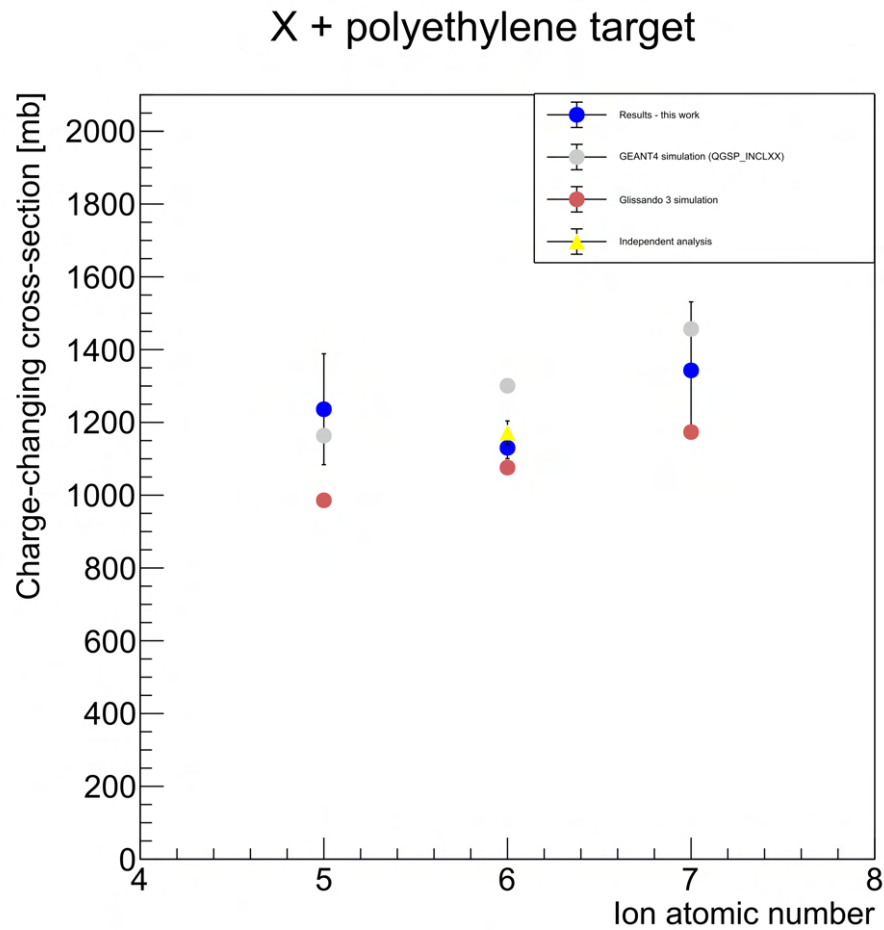
Figure 5.7: Charge-changing cross-section for fragmentation process of 13.4A GeV beam particle with polyethylene target. Comparison with GEANT4 and GLISSANDO3 simulation and for ^{12}C with independent analysis [28].
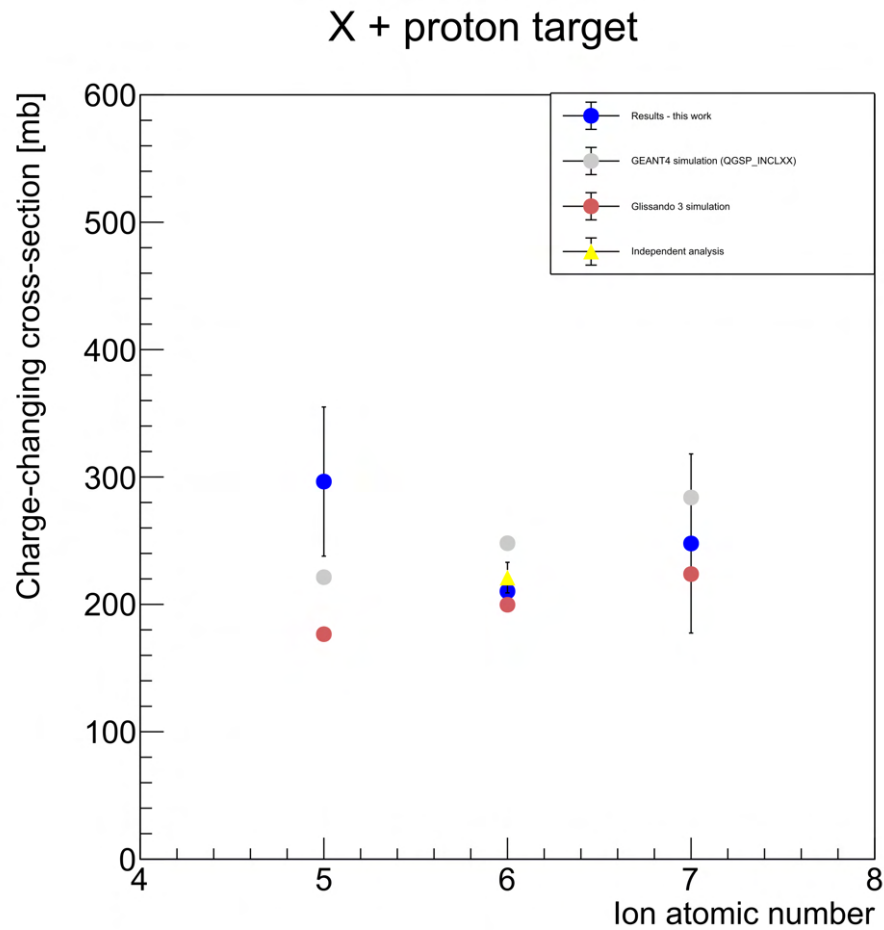
Figure 5.8: Charge-changing cross-section for fragmentation process of 13.4A GeV beam particle with proton target. Comparison with GEANT4 and GLISSANDO3 simulation and for ^{12}C with independent analysis [28].

Chapter 6

Systematic errors analysis

6.0.1 Systematic errors analysis

The procedure of systematic error analysis for charge-changing cross-section values for fragmentation of boron and nitrogen ions is as follows:

- upstream cuts - beam ion selection (ADC signals in S1) - first, the distance is calculated from mean peak value to upper and down cut, then cut boundaries were moved by 1% in both directions (loose and tight). Checked cut values can be seen in the figures 6.1, 6.8.

- upstream cuts - time of flight between A and S1 detector - cut was chosen based on 3σ value from Gauss fit 4.20, then cut boundaries were moved by 5% of 3σ value in both directions (loose and tight). Checked cut values can be seen in the figures 6.3, 6.10.

- downstream cuts - Z^2 in MTPC-L - cut value was choose as 3σ of fitted function 4.28[1], then cut boundaries were moved by 1% in both directions (loose and tight). Checked cut values can be seen in the figures 6.5, 6.12, 6.17 and 6.22.

- downstream cuts - number of clusters on track in MTPC-L - for all reactions, the cut was set to statement that the number of clusters on track must be greater than 50. In an examination of the influence of selecting this cut value on the results, the cut was moved in the range of 40-60.

A systematic error analysis for ^{12}C and ^{13}C for downstream cuts was made with the use of the same way as in the description above. For upstream cut, choosing the optimal cut was made with the use of the algorithm described in 4.0.4, then the cut was shifted (loose and tight) in the range from $1 - 9\%$ for ^{12}C and in the range from $1 - 14\%$ for ^{123}C. Checked cut values can be seen in the figures 6.15 and 6.20.

For each reaction, the description is organized as follows: first is a graphical description of the checked cut, then is a result of systematic error analysis, where

---

[1]Rounded to integer value.

70:8855329730

on the x-axis is the cut value and on the y-axis is the value in % how cross-section valued changed in comparison to main results of this thesis. For comparison reasons, each graph with results has a statistical error value on the top right. The order of the analyzed reactions is[2]:

- $(^{10}B +^{11} B) + T \rightarrow X(Z < 5)$

- $(^{13}N +^{14} N +^{15} N) + T \rightarrow X(Z < 7)$

- $^{12}C + T \rightarrow X(Z < 6)$

- $^{13}C + T \rightarrow X(Z < 6)$

Discussion of the results. Analysis was made for each minor cut; analysis focused on checking how stable the result is when the cut value is shifted. Because of the high statistics of collected data, the result for the charge-changing cross-section for ^{12}C is stable for each cut selection checked. The change in result in all cases is less than 2% for both cases when the cut is tighter and loose. For the charge-changing cross-section for ^{13}C statistic is lower, but the results are still quite stable and vary around 2%.

The charge-changing cross-section for the nitrogen and boron fragmentation process was measured with low statistics, which is why, in systematic error analysis, the influence of statistical fluctuations on the result can be seen. The most crucial cut is cut for beam selection because of the poorest resolution of distribution. For boron, results vary up to 8% and for nitrogen, up to 20%, taking into account high statistical error for charge-changing cross-section value for reaction $(^{13}N+^{14}N+^{15}N)+T \rightarrow (X<7)$ here the statistical fluctuations have big influence and detailed systematic error analysis can not be performed.

---

[2]Where T is a target.
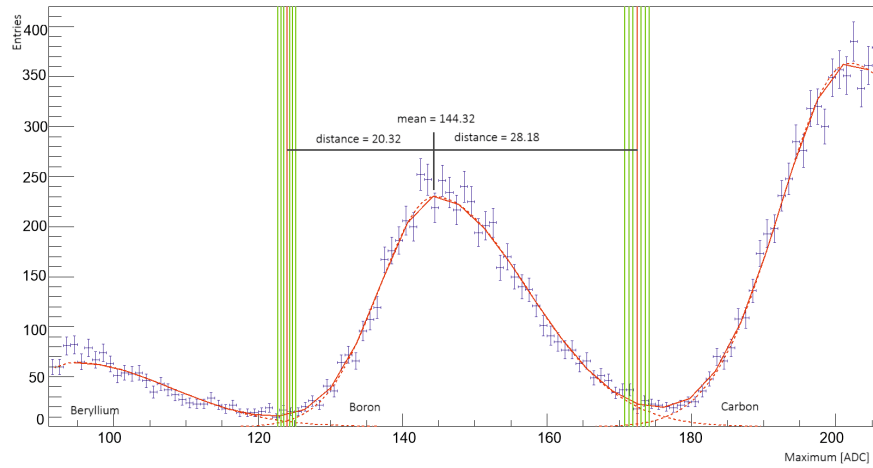
Figure 6.1: Systematic error analysis for S1 signal cut selection for reaction $(^{10}B+^{11}B)+T \rightarrow (X{<}5)$. Description of checked cuts.
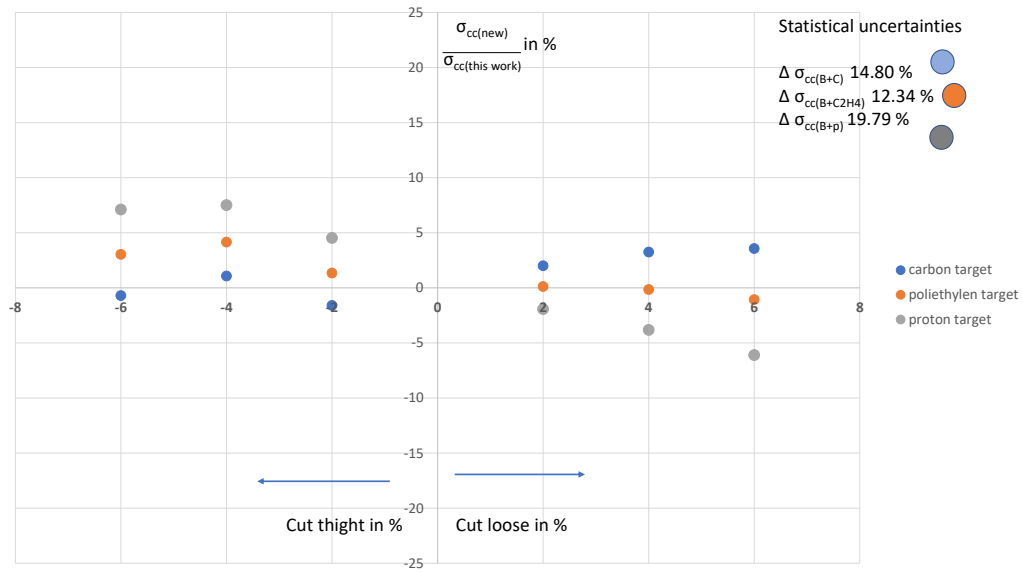
Figure 6.2: Systematic error analysis for S1 signal cut selection for reaction $(^{10}B+^{11}B)+T \rightarrow (X{<}5)$. Results of the analysis: on the x-axis is the cut value, and on the y-axis is the value in % how the cross-section value changed in comparison to the main results of this thesis.
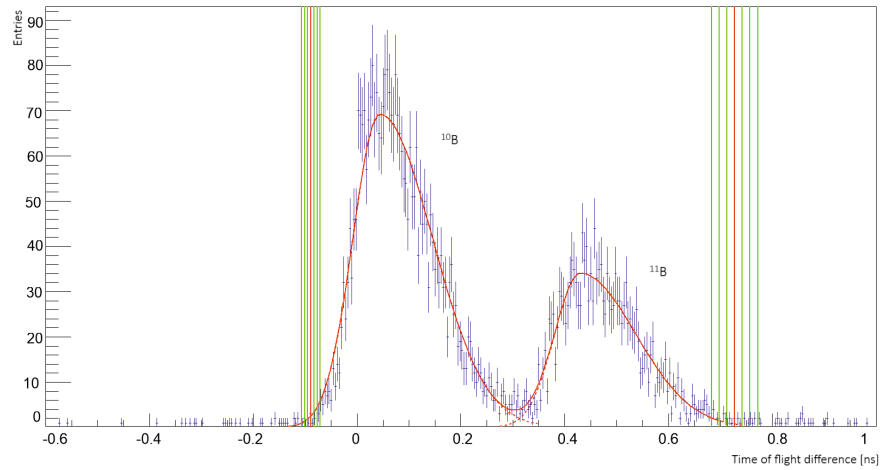
Figure 6.3: Systematic error analysis of ToF cut selection for reaction $(^{10}B+^{11}B)+T\rightarrow(X{<}5)$. Description of checked cuts.
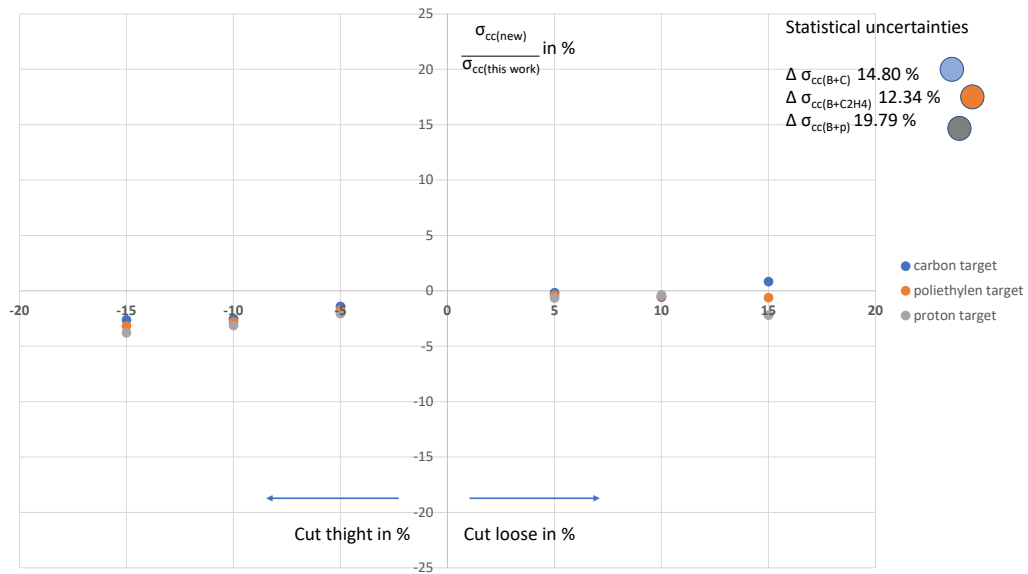
Figure 6.4: Systematic error analysis of ToF cut selection for reaction $(^{10}B+^{11}B)+T\rightarrow(X{<}5)$. Results of the analysis: on the x-axis is the cut value, and on the y-axis is the value in % how the cross-section value changed in comparison to the main results of this thesis.
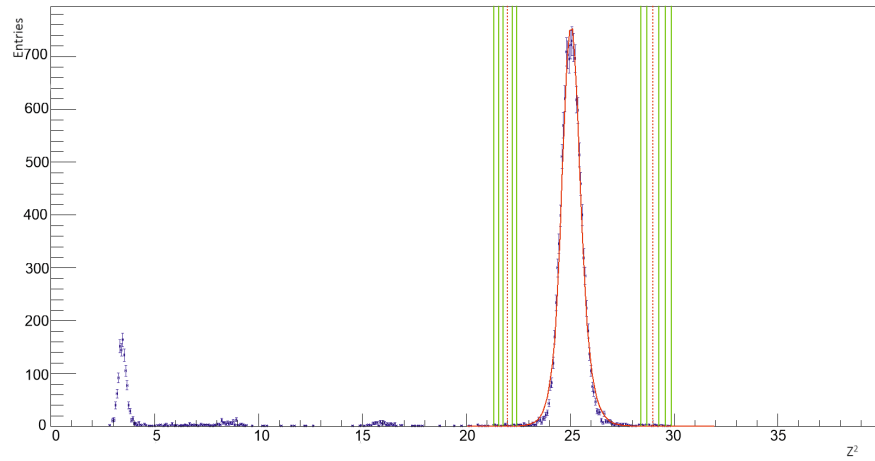
Figure 6.5: Systematic error analysis of Z^2 cut selection in MTPC-L for reaction $(^{10}B+^{11}B)+T\rightarrow(X<5)$. Description of checked cuts.
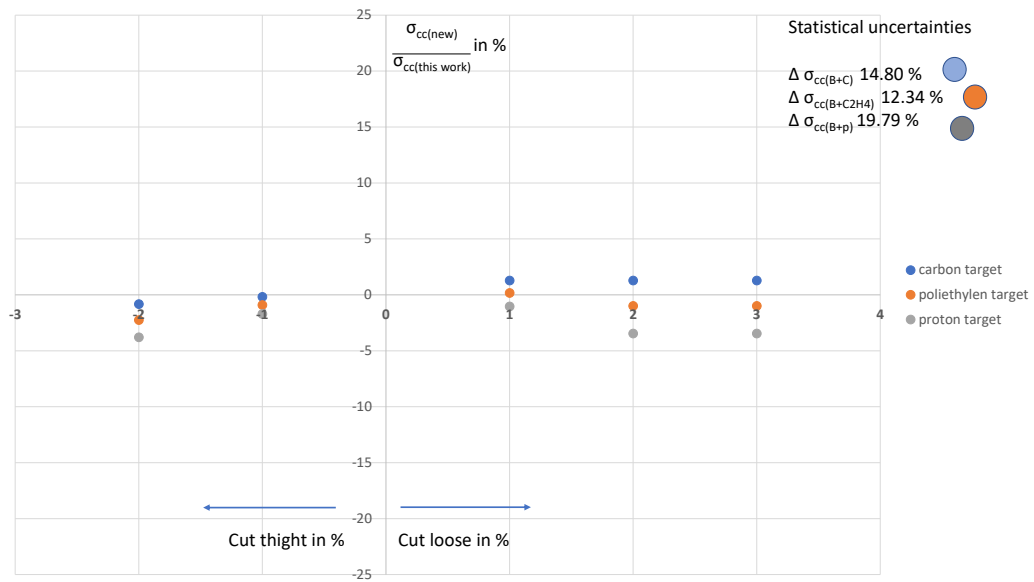
Figure 6.6: Systematic error analysis of Z^2 cut selection in MTPC-L for reaction $(^{10}B+^{11}B)+T\rightarrow(X<5)$. Results of the analysis: on the x-axis is the cut value, and on the y-axis is the value in % how the cross-section value changed in comparison to the main results of this thesis.
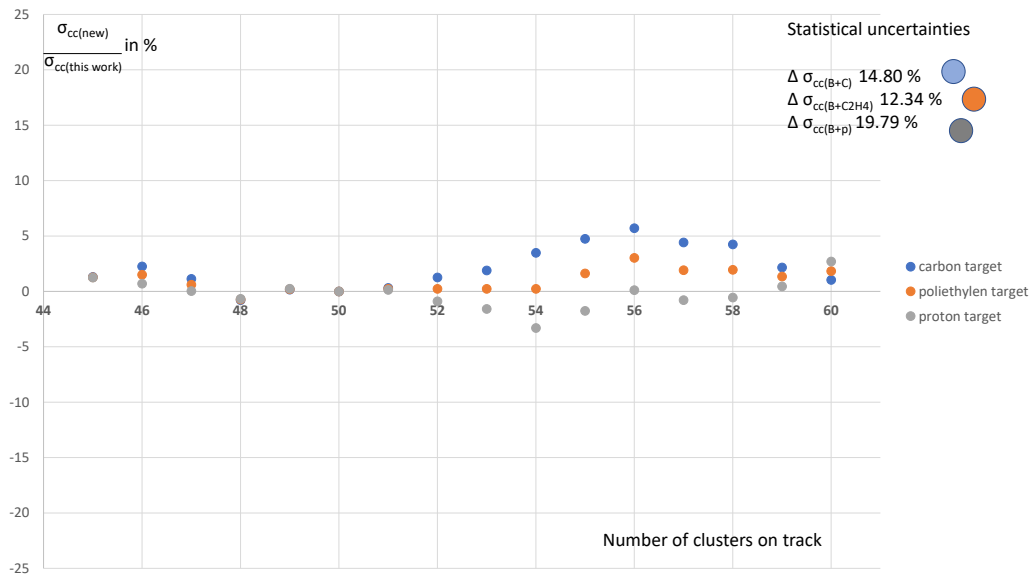
Figure 6.7: Systematic error analysis of a required number of clusters on a track cut selection in MTPC-L for reaction $(^{10}B+^{11}B)+T{\to}(X{<}5)$. Results of the analysis: on the x-axis is the cut value, and on the y-axis is the value in % how the cross-section value changed in comparison to the main results of this thesis.
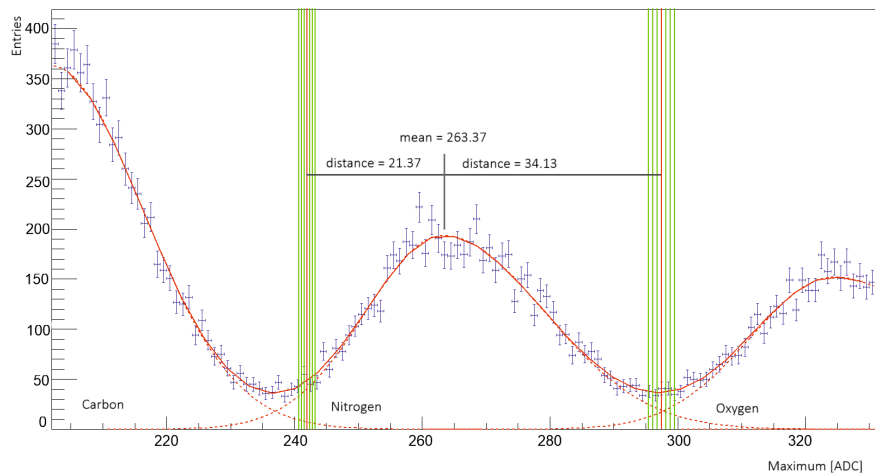
Figure 6.8: Systematic error analysis of S1 signal cut selection for reaction $(^{13}N+^{14}N+^{15}N)+T{\to}(X{<}7)$. Description of checked cuts.
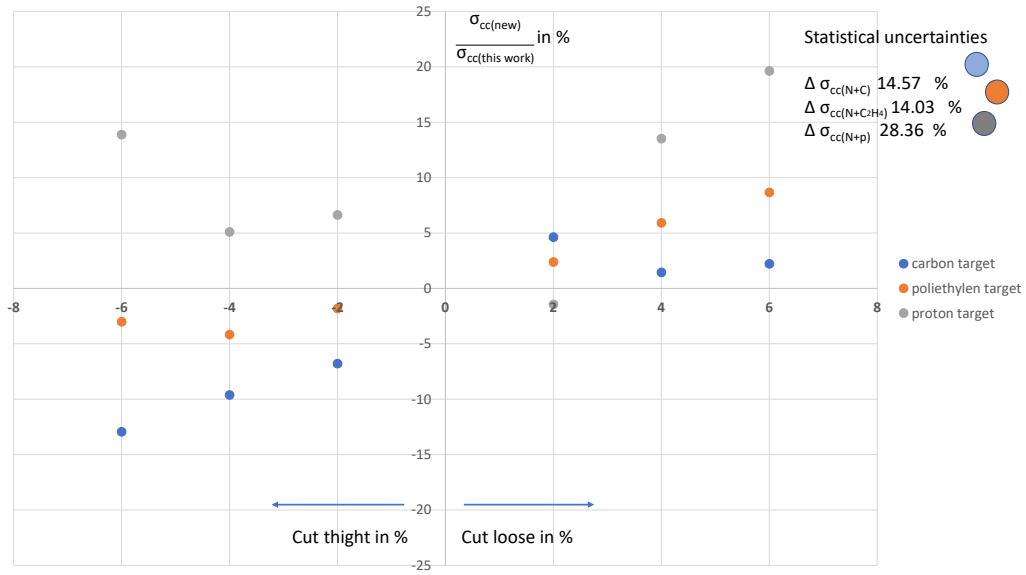
Figure 6.9: Systematic error analysis of S1 signal cut selection for reaction $(^{13}N+^{14}N+^{15}N)+T\rightarrow(X<7)$. Results of the analysis: on the x-axis is the cut value, and on the y-axis is the value in % how the cross-section value changed in comparison to the main results of this thesis.
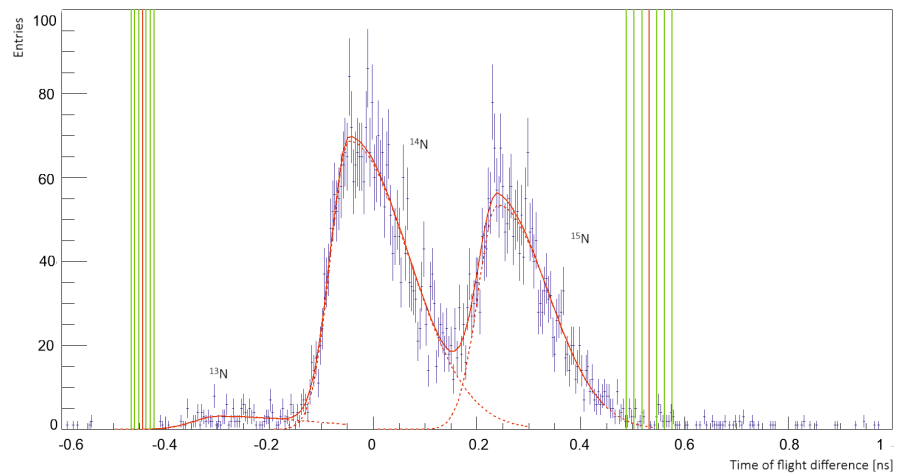
Figure 6.10: Systematic error analysis of ToF cut selection for reaction $(^{13}N+^{14}N+^{15}N)+T\rightarrow(X<7)$. Description of checked cuts.
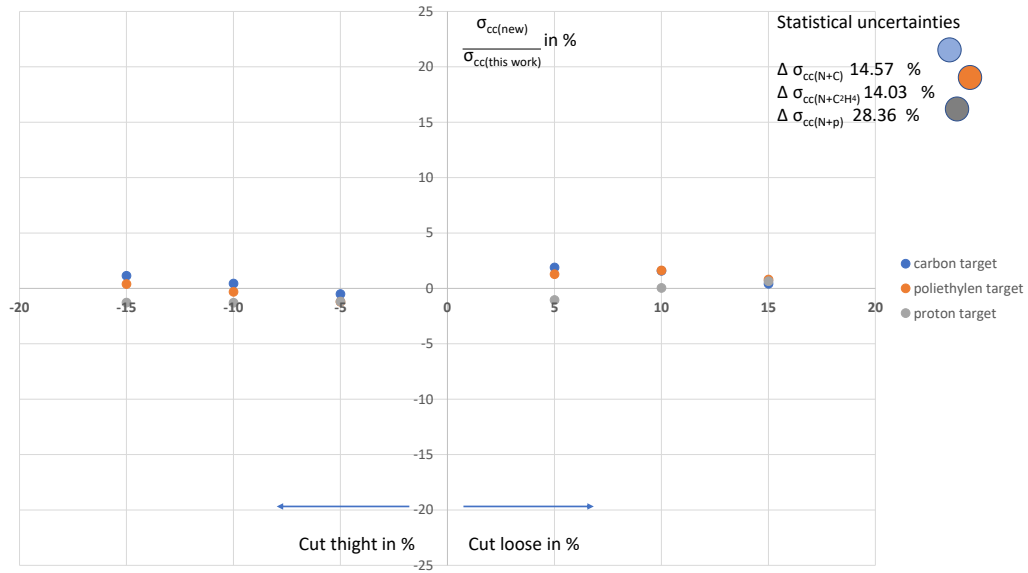
Figure 6.11: Systematic error analysis of ToF cut selection for reaction $(^{13}N+^{14}N+^{15}N)+T\rightarrow(X<7)$. Results of the analysis: on the x-axis is the cut value, and on the y-axis is the value in % how the cross-section value changed in comparison to the main results of this thesis.
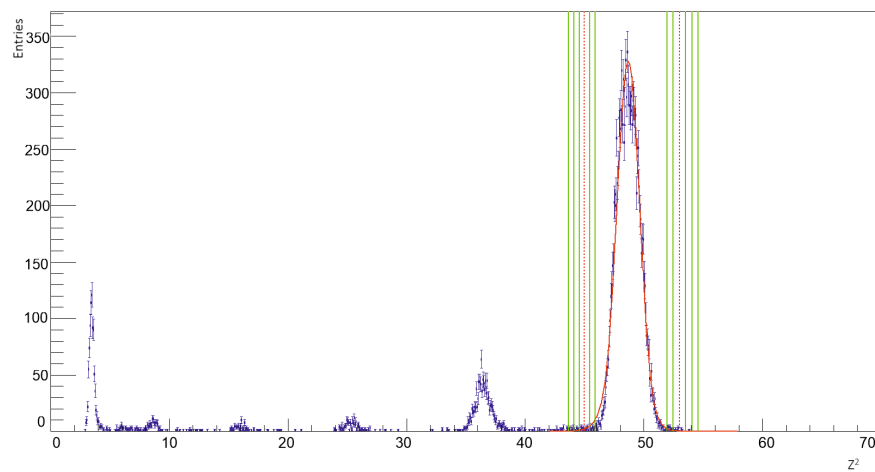
Figure 6.12: Systematic error analysis of Z^2 cut selection in MTPC-L for reaction $(^{13}N+^{14}N+^{15}N)+T\rightarrow(X<7)$. Description of checked cuts.
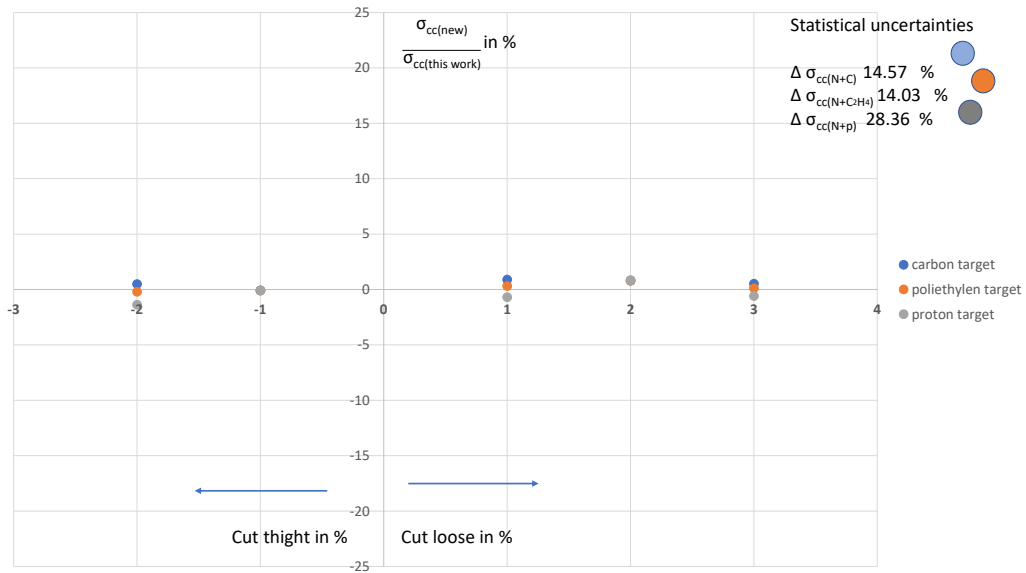
Figure 6.13: Systematic error analysis of Z^2 cut selection cut in MTPC-L for reaction $(^{13}N+^{14}N+^{15}N)+\text{T}\rightarrow(\text{X}<7)$. Results of the analysis: on the x-axis is the cut value, and on the y-axis is the value in % how the cross-section value changed in comparison to the main results of this thesis.
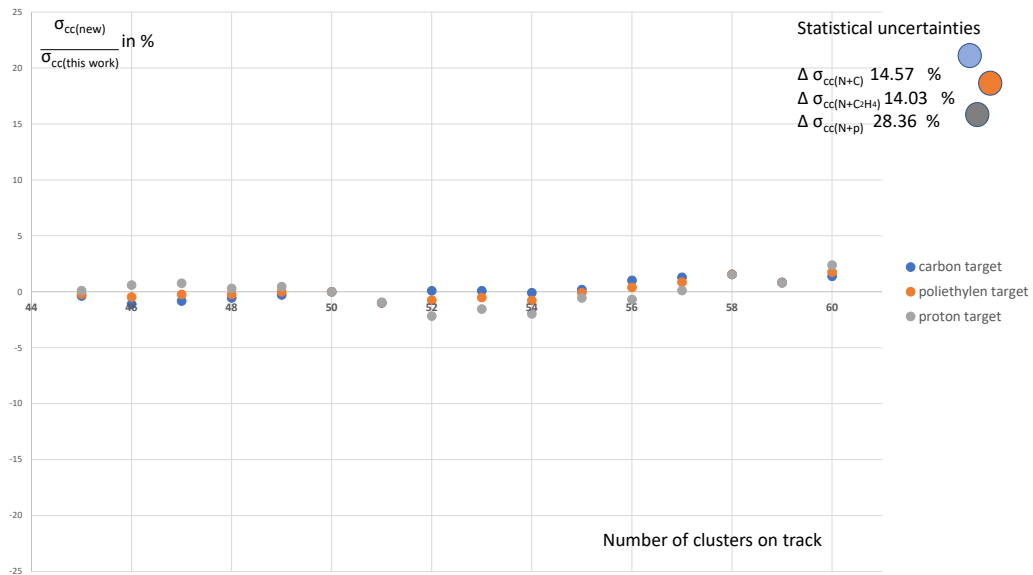
Figure 6.14: Systematic error analysis of a required number of clusters on a track selection cut in MTPC-L for reaction $(^{13}N+^{14}N+^{15}N)+\text{T}\rightarrow(\text{X}<7)$. Results of the analysis: on the x-axis is the cut value, and on the y-axis is the value in % how the cross-section value changed in comparison to the main results of this thesis.
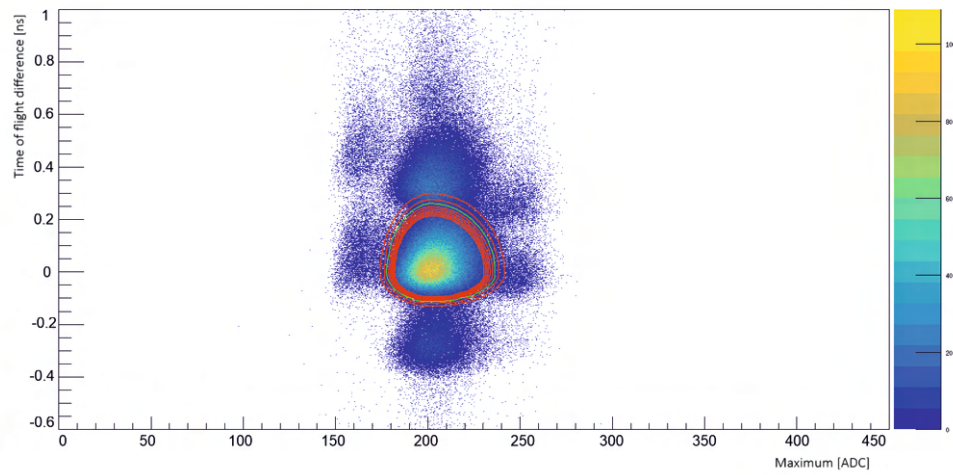
Figure 6.15: Systematic error analysis of beam isotope selection for reaction $^{12}C+$T$\rightarrow(X{<}6)$. Description of checked cuts.
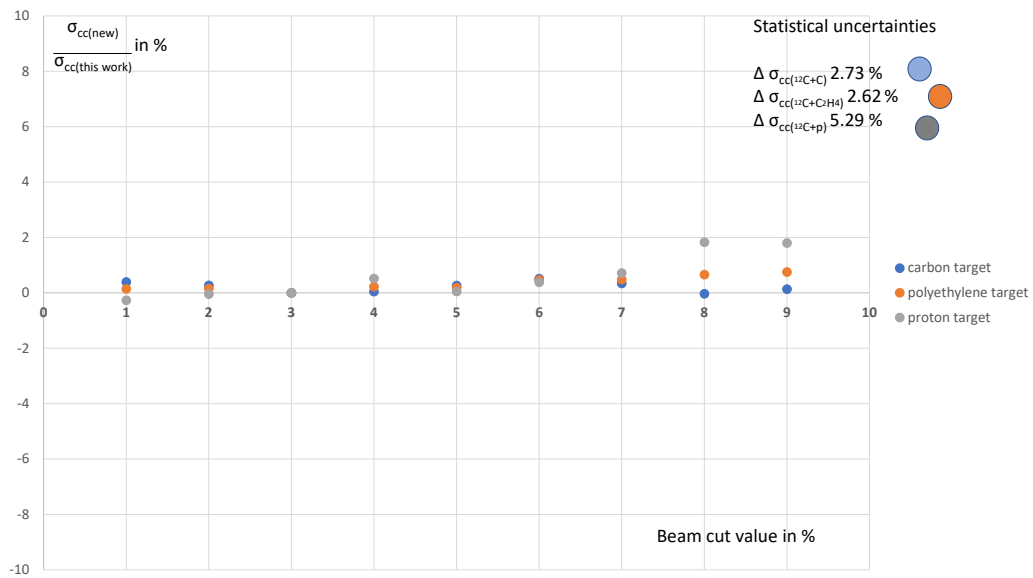
Figure 6.16: Systematic error analysis of beam isotope selection for reaction $^{12}C+$T$\rightarrow(X{<}6)$. Results of the analysis: on the x-axis is the cut value, and on the y-axis is the value in % how the cross-section value changed in comparison to the main results of this thesis.
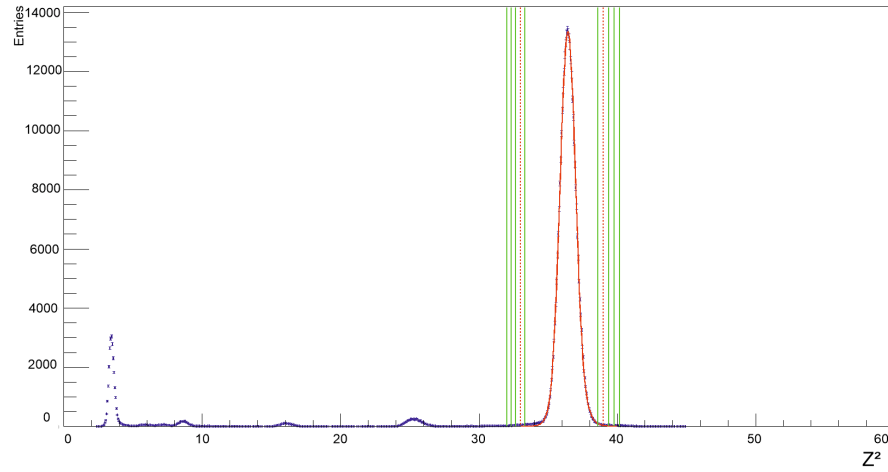
Figure 6.17: Systematic error analysis of Z^2 cut selection in MTPC-L for reaction $^{12}C+\mathrm{T}\to(X{<}6)$. Description of checked cuts.
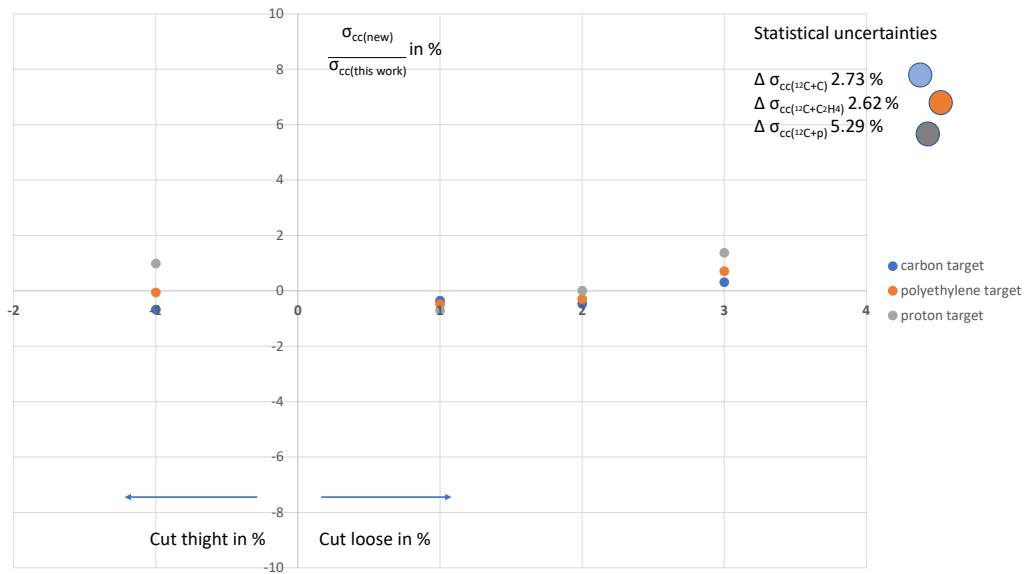
Figure 6.18: Systematic error analysis of Z^2 cut selection in MTPC-L for reaction $^{12}C+\mathrm{T}\to(X{<}6)$. Results of the analysis: on the x-axis is the cut value, and on the y-axis is the value in % how the cross-section value changed in comparison to the main results of this thesis.
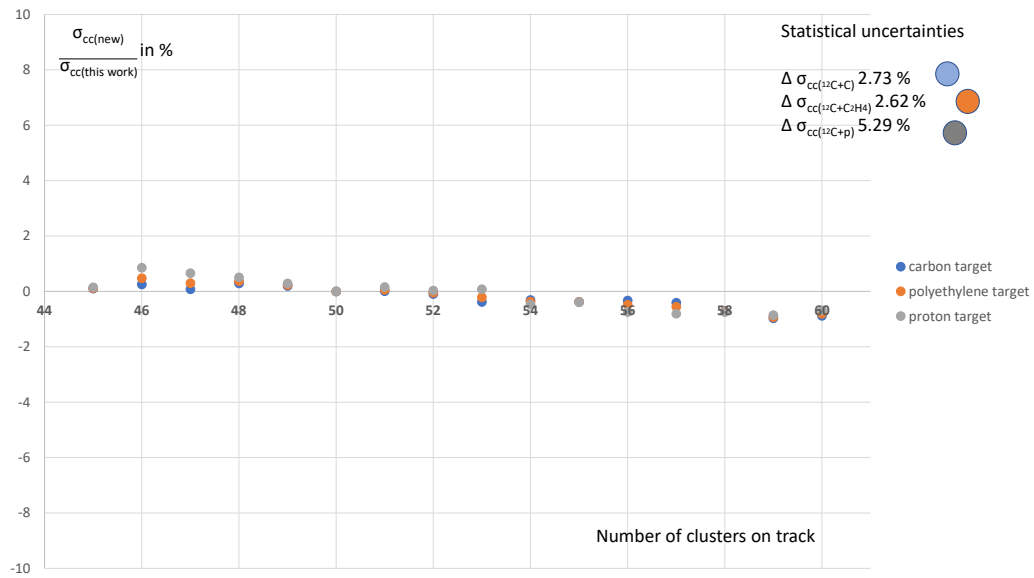
Figure 6.19: Systematic error analysis of a required number of clusters on a track cut selection in MTPC-L for reaction $^{12}C+$T$\rightarrow(X{<}6)$. Results of the analysis: on the x-axis is the cut value, and on the y-axis is the value in $\%$ how the cross-section value changed in comparison to the main results of this thesis.
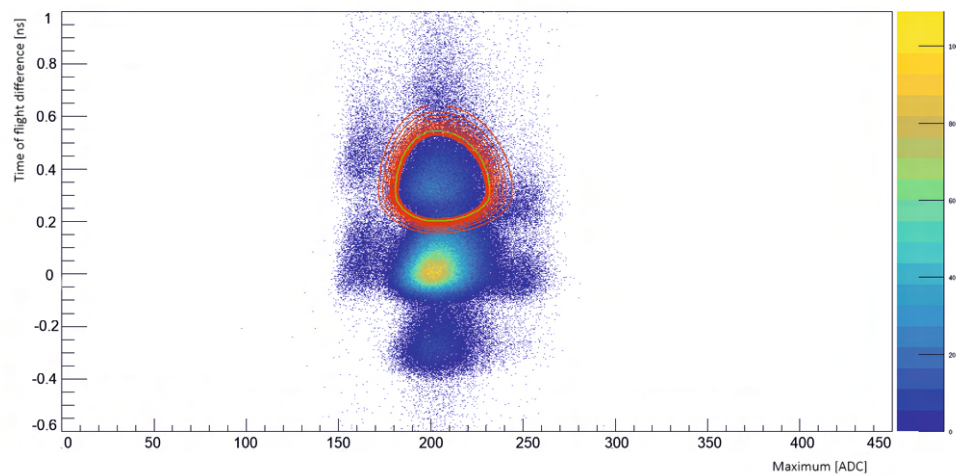
Figure 6.20: Systematic error analysis of beam isotope selection for reaction $^{13}C+$T$\rightarrow(X{<}6)$. Description of checked cuts.
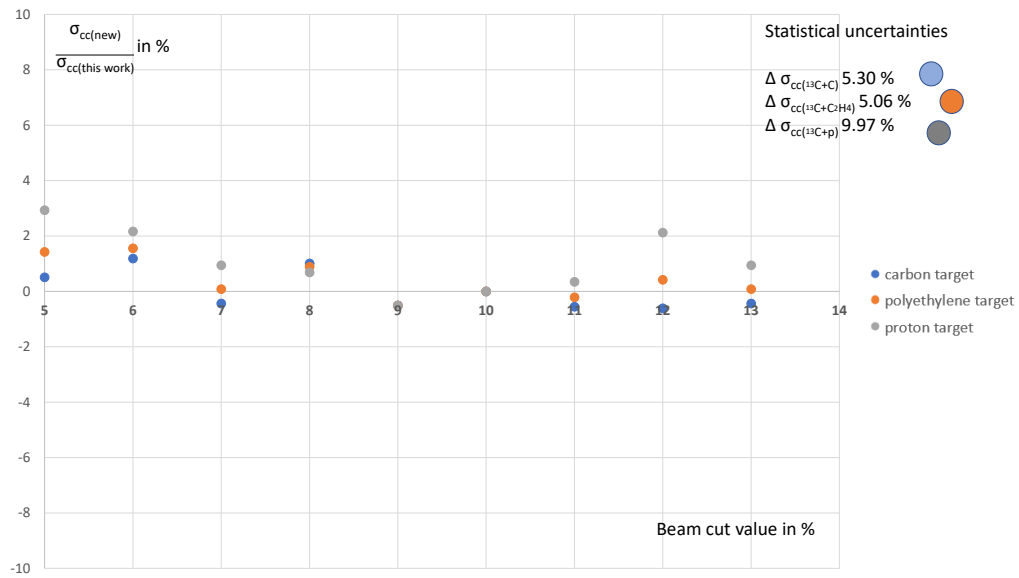
Figure 6.21: Systematic error analysis of beam isotope selection for reaction $^{13}C+\mathrm{T}\rightarrow(X{<}6)$. Results of the analysis: on the x-axis is the cut value, and on the y-axis is the value in % how the cross-section value changed in comparison to the main results of this thesis.
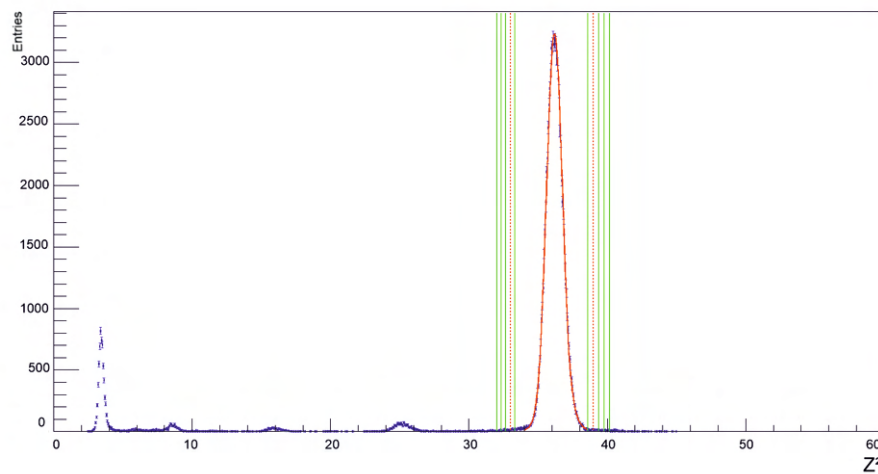
Figure 6.22: Systematic error analysis of Z^2 cut selection in MTPC-L for reaction $^{13}C+\mathrm{T}\rightarrow(X{<}6)$. Description of checked cuts.
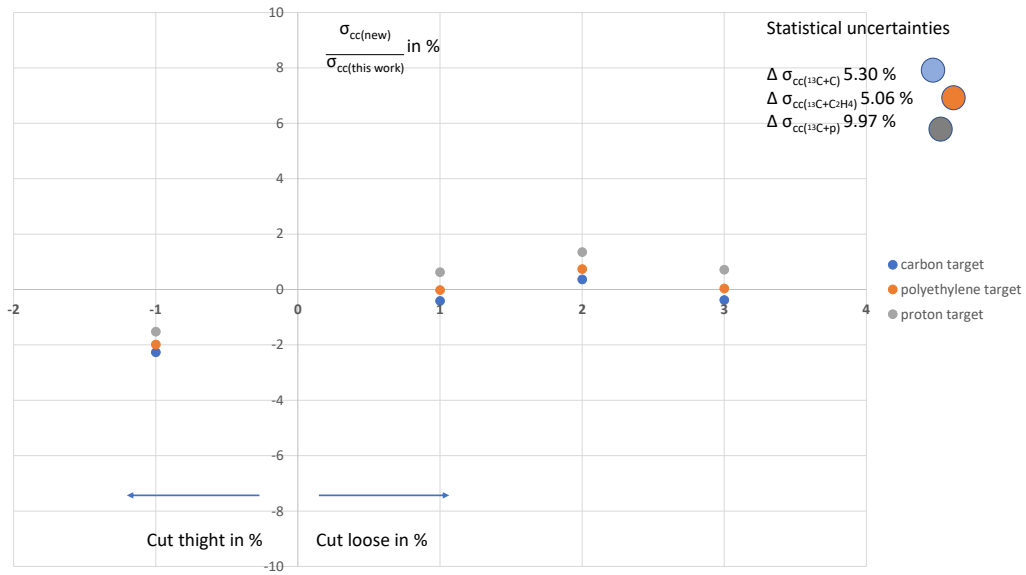
Figure 6.23: Systematic analysis of Z^2 cut selection in MTPC-L for reaction $^{13}C+$T$\rightarrow(X{<}6)$. Results of the analysis: on the x-axis is the cut value, and on the y-axis is the value in % how the cross-section value changed in comparison to the main results of this thesis.
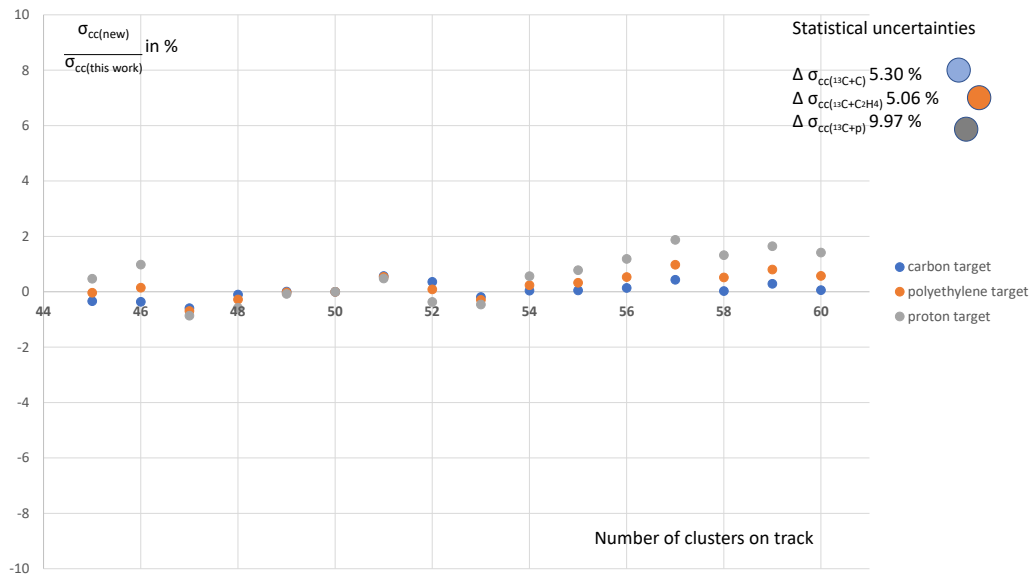
Figure 6.24: Systematic error analysis of a required number of clusters on a track cut selection in MTPC-L for reaction $^{13}C+$T$\rightarrow(X{<}6)$. Results of the analysis: on the x-axis is the cut value, and on the y-axis is the value in % how the cross-section value changed in comparison to the main results of this thesis.

Chapter 7

NA61/SHINE detector system upgrade

During Long Shutdown 2 (2018-2022), the NA61/SHINE detector system was upgraded [49][25]. The upgrade main purpose was to increase the data-taking rate for measurements planned after 2022 that include open charm measurements and measurements of nuclear fragmentation cross sections. The first physics data-taking after the upgrade took place in the summer of 2022.

The layout of the detector system after the upgrade is shown in figure 7.1. New detectors and systems which was upgraded or installed are:

- Vertex detector - new detector installed right after the target. Allows for the precise reconstruction of the interaction primary vertex and short-lived particles decay vertices[50].

- Beam position detectors - new detectors (silicon strip detectors) in replacement of old ones (proportional chambers) - discussed in more detail in section 7.1[51].

- Trigger and data acquisition system - new trigger system was designed to be flexible to handle the operation of various beams (protons, pions, kaons, ions) and targets to fulfill the requirements of the physics program after the Long Shutdown 2.

- TPC readout electronics - an increase in the data-taking rate up to 1 kHz, reduce noise level, and a better resolution in dE/dx measurement.

- Forward TPCs (FTPCs) - additional three forward TPCs (FTPCs) located on the beam line significant increase in the acceptance in the forward direction.

- PSD - second Forward Projectile Spectator Detector (PSD) was installed to increase radiation tolerance.

- Time of flight system - new detector (ToF-L) was installed, which is based on the Multigap Resistive Plate Chambers. The ToF-R wall will be installed in the future.

- Geometry Reference Chamber (GRC) - improved precision in drift velocity calibration.
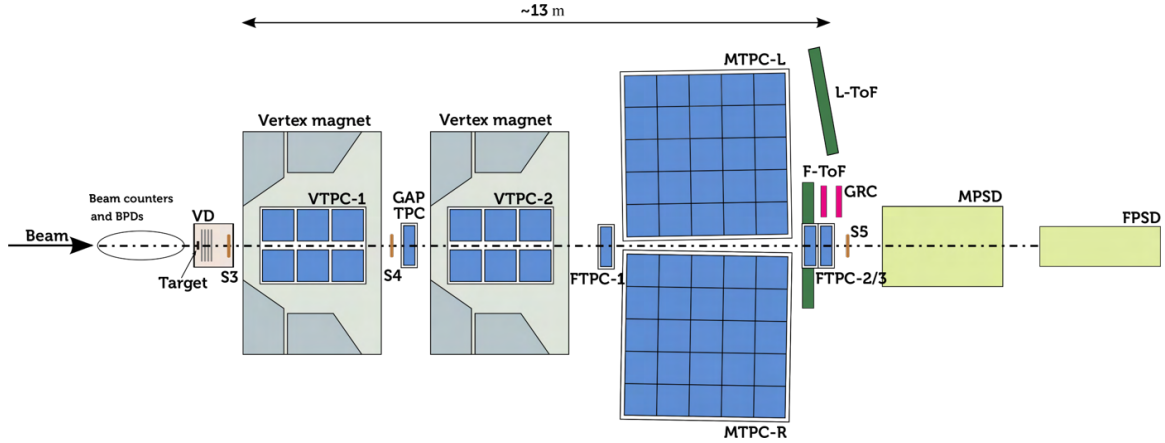
Figure 7.1: Layout of the NA61/SHINE detector system after upgrade.

According to fragmentation measurements, good beam identification and position measurements are crucial in working with the secondary beams. That way, during the Long Shutdown 2, attention was focused on creating a new beam position detector (BPD).

The BPDs that were used before the upgrade were constructed in 2009. These detectors were proportional chambers operated with Ar/CO_2 85/15 gas mixture. Detailed description may be found in chapter 3. During the past data campaigns, it was established that the gas detector system is suitable for proton beams but has limited efficiency with higher Z of the beam ions. Moreover, the electronic readout has not been updated for more than twenty years and cannot fulfill the requirements of the new fast TDAQ system. This was the main purpose for developing new beam position detectors.

7.1 New beam position detectors

Mechanical construction and readout electronics. New beam position detectors are based on silicon strip matrices made by Hamamatsu company (model S13804)[52]. Each matric is a silicon photo-diode with PN junctions arranged in the strip formation. The active area equals 97x97 mm^2 in size and 320 μm in thickness. The detector has 1024 stripes arranged in two rows. The pitch between the strips is 190 μm.

Two matrices are used to estimate the hit position in the x-y plane, one describing the x position and the second one rotated by 90° describing the y position. The schematic layout of the detector placed in the vacuum fitting and the detector photo are shown in figure 7.2. Detectors are placed on aluminum plates, which stabilize them and ensure they are in the correct position for the beam. The signal is extracted through ISO-K vacuum flanges with two high-density vacuum feed-through connectors

connected to the detectors by flexible PCB. The detector mounted on the beamline can be seen in figure 7.3.
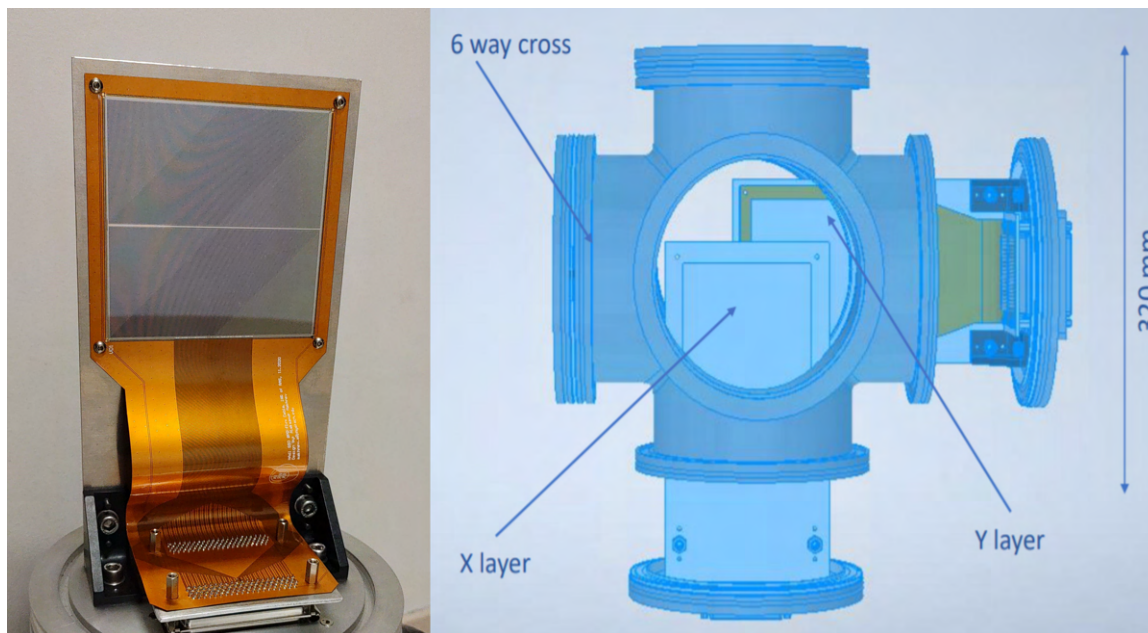
Figure 7.2: Silicon strip detector in 6-way vacuum fitting.

A dedicated readout electronics was designed and implemented. It consists of charge-sensitive amplifiers, intermediate amplifiers, and read-out buffers. The charge-sensitive amplifier is mounted directly on the vacuum cross. Its differential output signal is transmitted to the buffer through HDMI cables and an intermediate amplifier, which is an interface for the linear input of the buffer (DRS4 chip). A DRS4 chip converts the analog signal to digital data. It was chosen because it has a high sampling speed (up to 5 GHz) and allows for saving waveform for each strip, saved waveform can be seen in figure 7.5. The amplifier board design can be seen in figure 7.4.

Position reconstruction algorithm. Each BPD measures the position of the trigger-selected beam particle in two orthogonal directions independently. During measurements with a lead-ion beam in each strip plane, a charge distribution is induced with a width of about 10 strips.

The reconstruction algorithm first searches for a cluster in each plane. The cluster is defined as a set of adjacent strips with signal amplitudes above a threshold value. Then, an average of the strip positions weighted with the signal amplitudes on the strips is calculated for the cluster to estimate the position of the beam particle (the so-called centroid method). A 3-dimensional point measured by a given BPD is built from two transverse coordinates measured by the two-strip planes and the position of the BPD along the beamline. In order to reconstruct a beam particle track, the least squares fit of straight lines is performed to the positions measured by the three BPDs in X–Z and Y –Z planes independently.
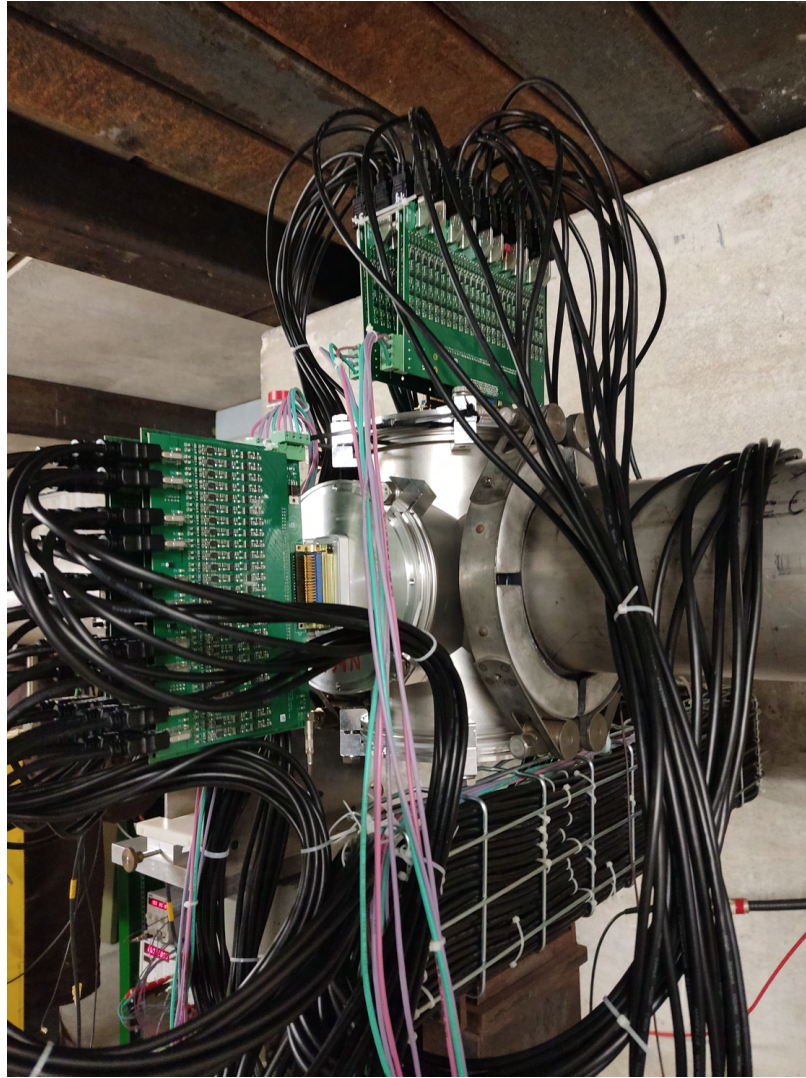
Figure 7.3: Detector mounted on the beam line.

An example of cluster and saturated and unsaturated (red) signal on Silicon Strip Detector induced by 150A GeV/c lead ion is shown in figure 7.5.

Beam monitoring. The new beam position detectors were successfully used to monitor beam parameters during three measurement campaigns with 150A GeV/c lead-ion beam. During measurements, the main beam parameters that are monitored are position, width, emittance, and the reconstructed main interaction vertex. All of these measurements are also saved and used during the reconstruction and analysis of the collected data after the measurement campaign is completed. The plots of the beam profiles are presented in figure 7.6. The reconstructed beam tracks in XZ and YZ planes are shown in figure 7.7 and in figure 7.8.
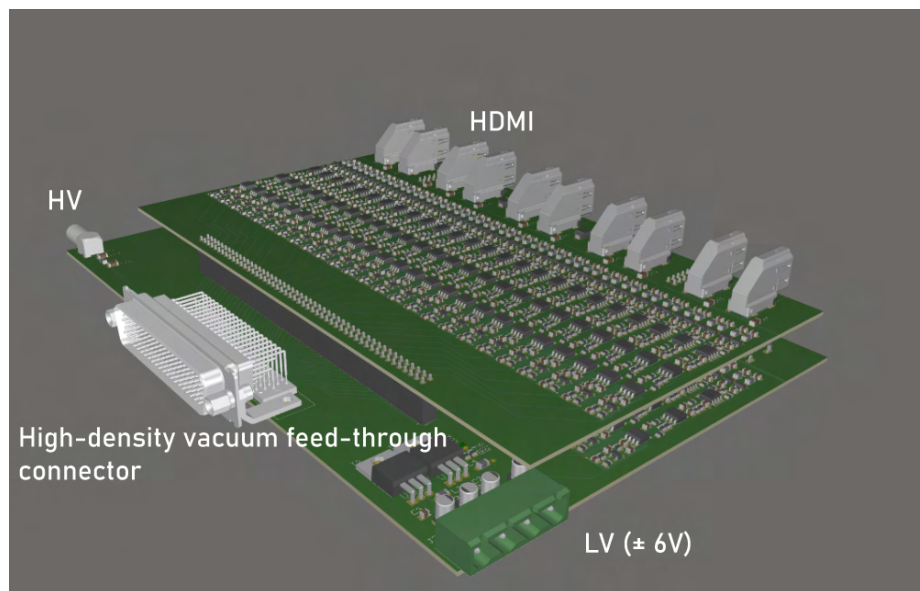
Figure 7.4: Amplifier board design.
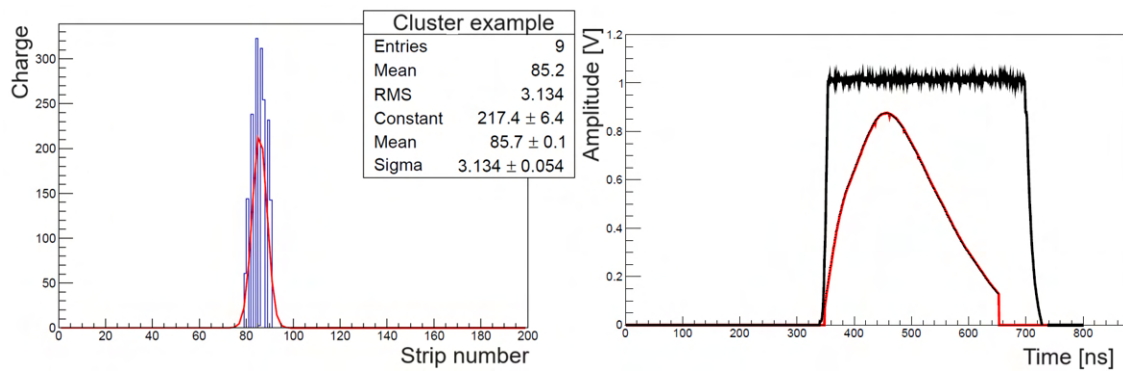
Figure 7.5: Example of cluster and saturated and unsaturated (red) signal on Silicon Strip Detector induced by 150A GeV/c lead ion.
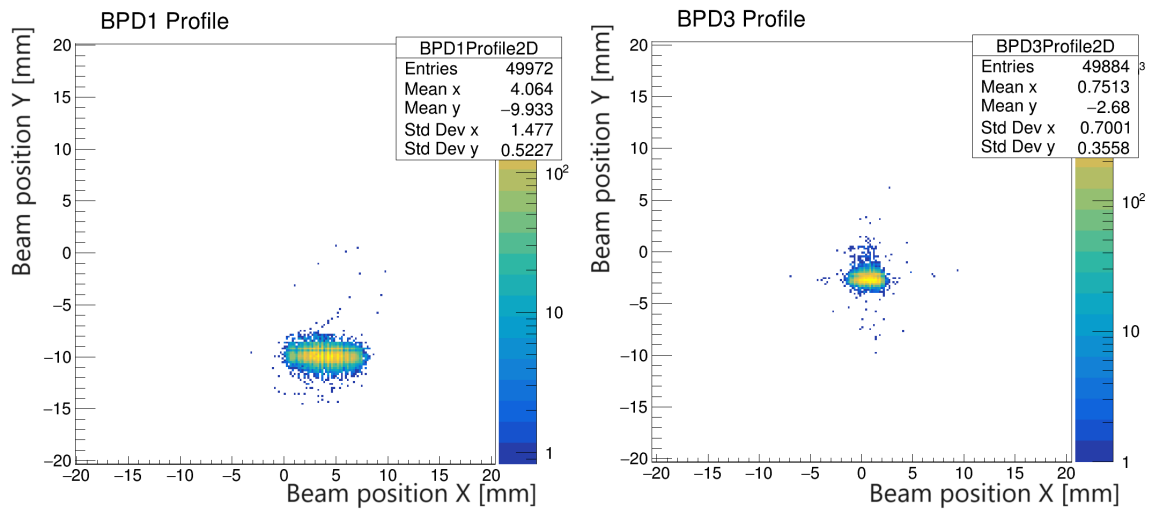
Figure 7.6: Histogram of beam position on BPD1 and BPD3.
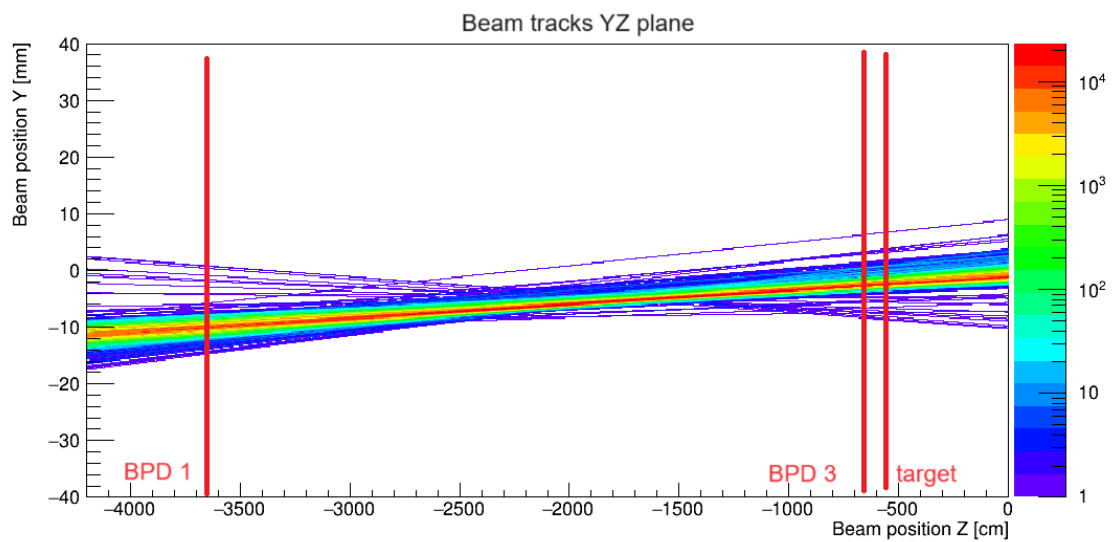
Figure 7.7: Reconstructed beam track in XZ plane.
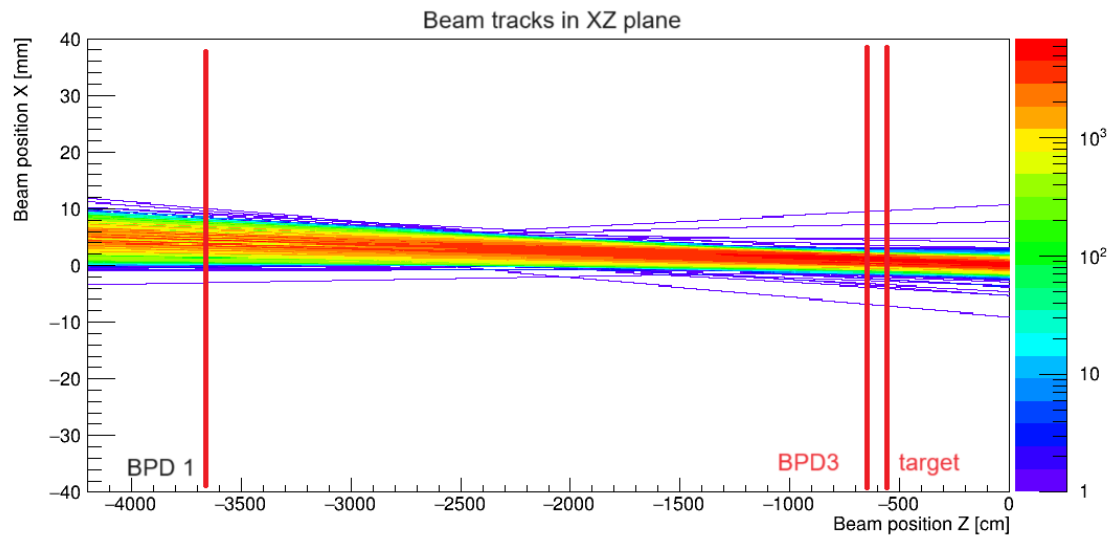
Figure 7.8: Reconstructed beam track in YZ plane.

Chapter 8

Preparation for the second campaign of nuclear fragmentation measurements after detector system upgrade

In this chapter, preparations and plans for measurements of nuclear fragmentation cross-sections planned for autumn 2024 will be discussed. Measurements will be carried out by the NA61/SHINE experiment. A detailed description of the motivation can be found in chapter 2.

Pilot studies were conducted in 2018, and the results of the analysis of collected data are presented in this thesis[1]. Data analysis was performed in parallel by several members of the NA61/SHINE collaboration. The analyses focused on determining various types of cross-sections for the fragmentation processes, and sometimes, they overlapped, which further improved the quality of the analysis. Results were described in chapters 3 and 5. Pilot studies proved that the NA61/SHINE facility is able to make these types of measurements with a high-quality detection system that consists of precise identification of secondary beam composition (including isotope separation) and very good resolving power of the main tracking device of produced fragments (system of time projection chambers). Pilot measurements, as long as a detailed analysis prepared by Genolini et al. [21, 22] allow us to determine the necessary statistics for every type of reaction so that the statistical errors of the measured production cross-sections for given isotope (Li, Be, B, C, N)[2] is reduced to required minimum described in chapter 2. The list of reactions that will be measured was also selected in accordance with the analyses contained in the mentioned works. The above-mentioned publications provide a comprehensive study of the importance of listed reactions on the production of given isotopes. This is important from the point of view of modeling the propagation of cosmic rays through the Galaxy. The

---

[1]Calculation of charge-changing cross-sections for the fragmentation process.

[2]Important from the point of view of modeling the propagation of cosmic rays through the Galaxy.

required number of interactions is presented in the table 8.1. New measurements not only provide new data for production cross-sections relevant to cosmic rays studies but also can provide data for charge-changing cross-sections, which are the subject of this work. Charge-changing cross-sections are important as test parameters for different models in cosmic rays propagation studies but are also important parameters in many other studies like estimating rms proton radii [53], visualization nuclei halo structure [54], and improvement of spacecraft shields [55, 56]. The analysis presented in this work allowed for the development of the methodology needed to analyze data from future high-statistic measurements.

A number of preparations were also made on the hardware side. During the Long Shutdown 2, the detector system was upgraded, which will allow the highest rate of data collection in 2024. An upgrade of the detector system was conducted to increase the taking rate tenfold up to 1 kHz. Additionally, increasing the data-taking rate allows us to register reactions for a broader range of the beam ions spectrum. A new beam position detector was installed to fulfill the requirements of high-rate data taking. More details about detector system upgrade can be found in chapter 7, together with a compressive description of the new Beam Position Detectors due to the author's direct involvement in their development. The setup of planned measurements can be found below:

- time slot: one week,

- secondary ion beam: nuclear fragments from SPS, Pb on primary Be target, p = 13.5A GeV/c,

- target: polyethylene(C_2H_4), carbon, and a small fraction of runs without any target, then cross-section for reaction with the proton, will be derivative from formula described in 4.0.3,

- beam identification: charge identification - scintillating detector,

- beam identification: isotope separation based on the time of flight measurements,

- produced fragment identification: charge identification - based on energy deposit measurements in Time Projection Chambers,

- produced fragment identification: isotope separation - measurements of fragments bending in the magnetic field.

Because two targets will be used as well as the measurement without the target, the effective number of interactions presented in table 8.1 will be at least four times larger. Taking into account the statistics collected during previous measurements in 2023 and 2024 after the upgrade, the measurement goal will be achieved within the assumed beam time of one week.

Table 8.1: Required number of interactions of different nuclei with protons to be recorded [22].

Reaction	N_{int}	Reaction	N_{int}
^{16}O+p	60k	^{28}Si+p	50k
^{12}C+p	50k	^{24}Mg+p	50k
^{11}B+p	10K	^{20}Ne+p	50k
^{15}N+p	10k	^{22}Ne+p	20k
^{14}N+p	10k	^{27}Al+p	10k
^{10}B+p	5k	^{26}Mg+p	10k
^{13}C+p	5k	^{23}Na+p	10k
^{7}Li+p	5k	^{25}Mg+p	10k
		^{21}Ne+p	10k
		^{32}S+p	5k
		^{29}Si+p	5k
$\sum N_{int}$=3x10^5			

Chapter 9

Summary

The thesis presents the results of the analysis of the charge-changing cross-sections for the fragmentation process. Cross-sections calculated in this work are charge-changing cross-sections for three beam ions: boron, nitrogen, and carbon at a beam momentum of 13.5A GeV/c. Cross-sections were calculated for interaction with two types of target carbon and polyethylene, and from the results, the cross-section for interaction with proton was calculated. Cross-section values for boron and nitrogen were calculated without isotope separation, and the cross-sections for the fragmentation process of carbon isotopes were calculated separately for ^{12}C and ^{13}C.

To calculate the charge-changing cross-sections, the interaction probabilities were first estimated for both targets. With the help of data collected without the target on, the probability of interaction with the detector material was also determined, enabling the correction of the results for the influence of beam interactions outside the target. To calculate the probability of interaction, two quantities were estimated: the number of beam ions that hit the target and the number of beam ions that left the target area without the interaction. To obtain these values, analysis was divided into two steps: beam composition analysis before the target and analysis of beam composition after the target. In the first steps, two measurements were used: ion charge was estimated based on the signal in the scintillating detector, and isotope separation was made based on time of flight measurements. Analysis of the product of the interaction with the target was made with the use of a time projection chamber. Ion separation is made in this detector based on energy loss by particles in a detector's active material.

The results of the analysis were compared with the results of the two simulations made with the use of GEANT4 (Physics list - QGSP INCLXX) and GLISSANDO 3. Results are in good agreement with both simulations within the limits of statistical error. The result for reaction $(^{10}B +^{11} B) + T \rightarrow X(Z < 5)$[1] are the most deviated from the rest of the data and from the growing trend of cross-section value along with an increase with the mass number of the ion and slightly exceeding the statistical error range; new measurements will allow for the correction of this value.

---

[1]Where T is a target, comment refers to the reaction with polyethylene and proton.

Currently, results are dominated by high statistical errors. The second measurements campaign scheduled for autumn of 2024 will allow for collecting higher statistics and what this involves, reducing statistical errors. New measurements with high statistics will allow for more accurate measurements of the isospin dependence when examining charge-changing cross-sections of carbon isotopes. The study of these relationships is currently an important topic and arouses great interest in the scientific community.

The second part of the thesis describes the author's commitment to the upgrade of the detector system during Long Shutdown 2, whose main purpose was to increase the efficiency of data collection. Data collection efficiency increased tenfold after the upgrade. All detectors had to adapt or change to meet these requirements, including the beam position detector, in the construction of which the author was directly involved. New beam position detectors are based on the single-sided silicon strip detector (SSD). Si strips produced by Hamamatsu (S13804) were used, where the pitch has a width equal to 190 μm. New detectors replaced the old ones: proportional chambers operated with an Ar/CO_2 85/15 gas mixture. During previous measurements, it was established that the old gas detectors are suitable for proton beams but has limited efficiency with higher Z of the beam ions. Moreover, the electronic readout has not been updated for more than twenty years and cannot fulfill the requirements of the new fast TDAQ system. The new beam position detectors were successfully used to monitor beam parameters during three measurement campaigns with a 150A GeV/c lead-ion beam.

There is very limited data for measurements of charge-changing cross-sections at energies above 1A GeV, therefore, past and future measurements from the NA61/SHINE experiment can make a significant contribution to filling this gap. The results obtained in this work show that the experiment's detector system is able to measure charge-changing cross-sections at high energies for a wide range of ion charges, including very good identification of individual isotopes. Both tasks described in the thesis made significant contributions to the preparation for the second fragmentation measurements campaign. Framework to the analysis of the collected data presented in this work will allow for the analysis of newly collected data in a more efficient and accurate way.

Appendix A

Analysis of contamination from ^{10}B, ^{11}B, ^{14}N and ^{15}N isotopes

This appendix contains a detailed description of the procedure of estimation parameters of the full ^{10}B, ^{11}B, ^{14}N, and ^{15}N distribution for T3 trigger. Estimation is a necessary step to calculate the purity of the $^{12}C/^{13}C$ selection. To calculate purity, contamination from neighboring ions needs to be analyzed in a selected cut range. It is clearly visible in figure 4.10 that even with pre-carbon selection in the T3 trigger, signals from neighboring ions are also present in the selected beam.

However, the register distributions of ^{10}B, ^{11}B, ^{14}N and ^{15}N are not full because the discriminator cut most of them; the parameters of full distribution must be estimated. Estimation is made based on data from the T1 trigger; the assumption is that regardless of the used trigger (T1 or T3), sigma and mean values would be the same for each ion in the S1 signal spectrum[1]; the same assumption is made for isotopes time of flight spectrum. An additional assumption is that ratios between maxima should be the same for T1 and T3 trigger[2] and it is used in estimation maximum for full distribution of ^{10}B, ^{11}B, ^{14}N, and ^{15}N for T3 trigger data. Fit results, as well as the estimate parameters, can be found in table A.1. The procedure is as follows:

- fit 2D Gauss 4.24 function to ^{10}B, ^{11}B, ^{14}N, ^{15}N peaks in S1 vs. ToF distribution register with T1 trigger A.1 (step 1),

- analyzed ratios between maxima of carbon and neighboring ions A.2 on S1 signals spectrum register with T1 trigger (step 2),

- estimate scaling factor for ^{10}B, ^{11}B, ^{14}N, ^{15}N for T3 trigger, based on step 2 (step 3),

- fitting 2D Gauss function to $^{12}C/^{13}C$ peaks in S1 vs. ToF distribution (4.10 - register with T3 trigger) and calculate the maximum (step 4),

---

[1] In case discriminator didn't cut most of the signals. Only the statistic will be different.

[2] Graphical description can be found in figure A.2.

- construct full 2D distribution for T3 trigger for wanted isotope with sigma and mean value from step 1 and constant value based on scaling factor calculated in steps 2 and 3 multiplied by a maximum of $^{12}C/^{13}C$ form step 4. Results can be seen in figures 4.13 and 4.14.
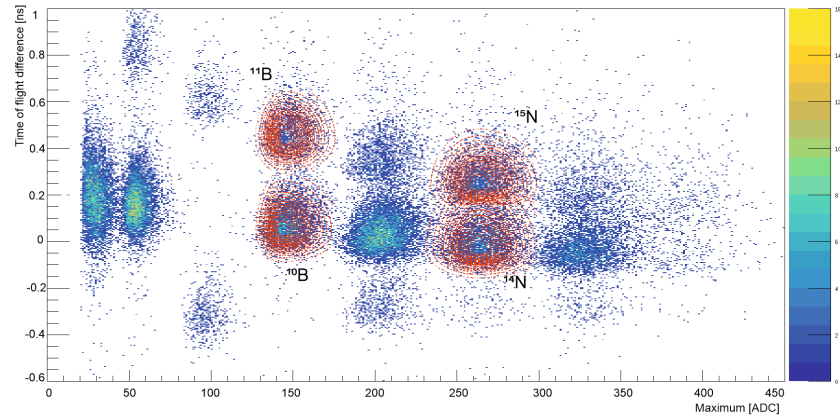
Figure A.1: Result of the fit two-dimensional Gauss 4.24 to ^{10}B, ^{11}B, ^{14}N, ^{15}N peaks in S1 vs. ToF distribution register with T1 trigger.
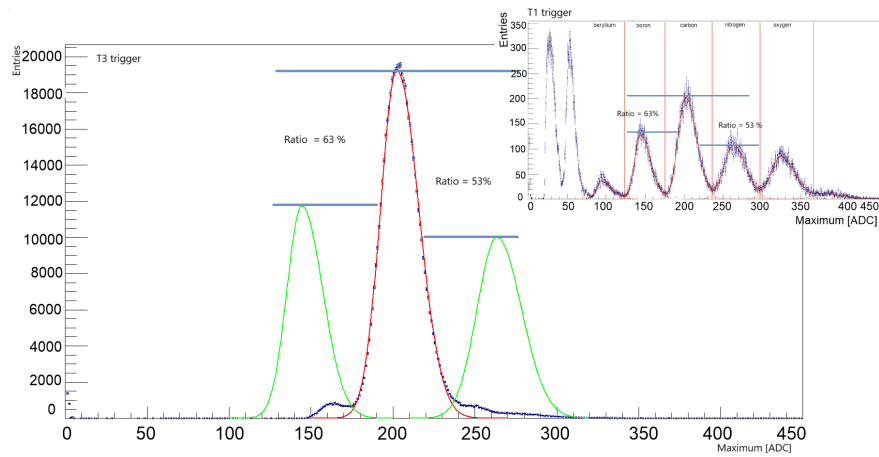
Figure A.2: Graphical description of scaling factor estimation. The scaling factor describes the ratio in % between carbon and neighboring ions (boron and nitrogen) for the T1 trigger. Then the same ratio is kept for estimated ^{10}B, ^{11}B, ^{14}N, ^{15}N distributions for T3 trigger.

Table A.1: Result of the fit two-dimensional Gauss 4.24 to ^{10}B, ^{11}B, ^{14}N, ^{15}N peaks in S1 vs. ToF distribution register with T1 trigger A.1. Based on the parameters included in the table, parameters of the full distribution of peaks ^{10}B, ^{11}B, ^{14}N, ^{15}N for the T3 trigger are estimated.

Projectile	scaling factor %	mean S1 [ADC]	σ_L	σ_R	mean ToF [ns]	σ_L	σ_R
^{10}B	0.63	142.49	6.09	14.46	0.04	0.05	0.10
^{11}B	0.63	144.75	7.17	12.64	0.44	0.06	0.09
^{14}N	0.53	263.39	12.91	15.93	-0.04	0.05	0.14
^{15}N	0.53	262.91	11.69	16.62	0.24	0.05	0.09

Appendix B

GEANT4 and GLISSANDO 3 simulation

Analysis results were compared with results of the two simulations made with use GEANT4 and GLISSANDO 3. This appendix contains detailed information on simulation parameters.

Glissando - version 3 is a Monte-Carlo generator for Glauber-like models of the initial stages of ultra-relativistic heavy-ion collisions[47]. Used parameters, model, and statistics:

- statistic - 1000000 events,

- model - wounded quark with a mixture of binary collisions,

- Gaussian wounding applied,

- collision energy $\sqrt{s_{NN}} = 5.2$ GeV.

The simulation was made for two targets: proton target and carbon target. Cross-sections for polyethylene target were estimated with the use of equation 5.3. The output of the simulation is a total inelastic reaction cross-section. That's why, according to knowledge described in 4.0.2 charge-changing cross-sections σ_{cc} are less by 10% of the total reaction cross-section σ_{rc}, values have been recalculated according to formula $\sigma_{cc} = \sigma_{rc} * 0.9$. Results can be found in table B.1.

Second simulation was made with use of GEANT4 and NA61/SHINE framework, NA61/SHINE framework provide detailed model of NA61/SHINE detector system setup. Used parameters and versions:

- statistic - 1000000 events,

- GEANT 4 version - v10.7.0.,

- SHINE software version - v1r21p3,

- physics list - QGSP_INCLXX.

The simulation was made for three types of target carbon, proton, and polyethylene. Results can be found in table B.2.

Table B.1: GLISSANDO3 simulation results.

projectile	proton target $\sigma_{cc}[mb]$	carbon target $\sigma_{cc}[mb]$	polyethylene target $\sigma_{cc}[mb]$
^{10}B	176.59	632.75	985.93
^{12}C	199.71	676.44	1075.87
^{14}N	223.78	725.93	1173.49

Table B.2: GEANT4 simulation results.

projectile	proton target $\sigma_{cc}[mb]$	carbon target $\sigma_{cc}[mb]$	polyethylene target $\sigma_{cc}[mb]$
^{10}B	221.34	699.97	1163.62
^{12}C	247.98	777.17	1300.69
^{14}N	283.90	861.92	1456.74

Bibliography

[1] M. Urbaniak, Y. Balkova, S. Kowalski, S. Puławski, and K. Wójcik (????).

[2] T. K. Gaisser, R. Engel, and E. Resconi, *Cosmic Rays and Particle Physics* (Cambridge University Press, 2016), 2nd ed.

[3] *Ams-02*, https://https://ams02.space/, accessed: 2024-07-29.

[4] *Calet*, https://calet.phys.lsu.edu/, accessed: 2024-07-29.

[5] *Dampe*, https://dpnc.unige.ch/dampe/, accessed: 2024-07-29.

[6] *Na61/shine*, https://shine.web.cern.ch/, accessed: 2024-07-29.

[7] A. Korejwo, T. Dzikowski, M. Giller, J. Wdowczyk, V. Perelygin, and A. Zarubin, Journal of Physics G: Nuclear and Particle Physics **26** (2000).

[8] I. V. Moskalenko and S. G. Mashnik, *Evaluation of production cross sections of li, be, b in cr* (2003), astro-ph/0306367, URL https://arxiv.org/abs/astro-ph/0306367.

[9] V. Ptuskin, Astroparticle Physics **39-40**, 44 (2012), ISSN 0927-6505, cosmic Rays Topical Issue, URL https://www.sciencedirect.com/science/article/pii/S0927650511002039.

[10] R. A. Mewaldt, M. Miller, J. R. Jokipii, M. A. Lee, T. H. Zurbuchen, and E. Mobius, eds., *Acceleration and transport of energetic particles observed in the heliosphere. Proceedings, Symposium, ACE 2000, Indian Wells, USA, January 5-8, 2000*, vol. 528 (2000).

[11] J. J. Engelmann, P. Ferrando, A. Soutoul, P. Goret, E. Juliusson, L. Koch-Miramond, N. Lund, P. Masse, B. Peters, N. Petrou, et al., Astronomy and Astrophysics **233**, 96 (1990).

[12] M. A. DuVernois, J. A. Simpson, and M. R. Thayer, Astronomy and Astrophysics **316**, 555 (1996).

[13] A. Lukasiak, F. McDonald, W. Webber, and P. Ferrando, Advances in Space Research **19**, 747 (1997), ISSN 0273-1177, cosmic radiation: Spectra and Composition, URL https://www.sciencedirect.com/science/article/pii/S0273117796001391.

[14] S. A. Stephens and R. E. Streitmatter, The Astrophysical Journal **505**, 266 (1998), URL https://dx.doi.org/10.1086/306142.

[15] T. A. Porter, R. P. Johnson, and P. W. Graham, Annual Review of Astronomy and Astrophysics **49**, 155–194 (2011), ISSN 1545-4282, URL http://dx.doi.org/10.1146/annurev-astro-081710-102528.

[16] J. Lavalle and P. Salati, Comptes Rendus. Physique **13**, 740–782 (2012), ISSN 1878-1535, URL http://dx.doi.org/10.1016/j.crhy.2012.05.001.

[17] P. v. Doetinchem, K. Perez, T. Aramaki, S. Baker, S. Barwick, R. Bird, M. Boezio, S. Boggs, M. Cui, A. Datta, et al., Journal of Cosmology and Astroparticle Physics **2020**, 035–035 (2020), ISSN 1475-7516, URL http://dx.doi.org/10.1088/1475-7516/2020/08/035.

[18] D. Collaboration, Science Bulletin **67**, 2162–2166 (2022), ISSN 2095-9273, URL http://dx.doi.org/10.1016/j.scib.2022.10.002.

[19] M. Aguilar, L. Ali Cavasonza, G. Ambrosi, L. Arruda, N. Attig, S. Aupetit, P. Azzarello, A. Bachlechner, F. Barao, A. Barrau, et al. (AMS Collaboration), Phys. Rev. Lett. **117**, 231102 (2016), URL https://link.aps.org/doi/10.1103/PhysRevLett.117.231102.

[20] O. Adriani, Y. Akaike, K. Asano, Y. Asaoka, E. Berti, G. Bigongiari, W. R. Binns, M. Bongi, P. Brogi, A. Bruno, et al. (CALET Collaboration), Phys. Rev. Lett. **129**, 251103 (2022), URL https://link.aps.org/doi/10.1103/PhysRevLett.129.251103.

[21] Y. Génolini, D. Maurin, I. V. Moskalenko, and M. Unger, Physical Review C **98** (2018), ISSN 2469-9993, URL http://dx.doi.org/10.1103/PhysRevC.98.034611.

[22] Y. Génolini, D. Maurin, I. V. Moskalenko, and M. Unger, Physical Review C **109** (2024), ISSN 2469-9993, URL http://dx.doi.org/10.1103/PhysRevC.109.064914.

[23] N. Abgrall, O. Andreeva, A. Aduszkiewicz, Y. Ali, T. Anticic, N. Antoniou, B. Baatar, F. Bay, A. Blondel, J. Blumer, et al., Journal of Instrumentation **9**, P06005–P06005 (2014), ISSN 1748-0221, URL http://dx.doi.org/10.1088/1748-0221/9/06/P06005.

[24] M. Unger and N. Collaboration, *New results from the cosmic-ray program of the na61/shine facility at the cern sps* (2019), 1909.07136, URL https://arxiv.org/abs/1909.07136.

[25] P. Podlaski, *Na61/shine overview* (2024), 2402.10973, URL https://arxiv.org/abs/2402.10973.

[26] D. Larsen and A. Merzlaya, Journal of Physics: Conference Series **1137**, 012048 (2018), ISSN 1742-6596, URL http://dx.doi.org/10.1088/1742-6596/1137/1/012048.

[27] M. Buénerd and I. Efthymiopoulos, Tech. Rep., CERN, Geneva (2003), URL https://cds.cern.ch/record/622246.

[28] S. Collaboration, *Measurement of the mass-changing, charge-changing and production cross sections of ^{11}c, ^{11}b and ^{10}b nuclei in $^{12}c+p$ interactions at 13.5 gev/c per nucleon* (2024), 2410.18273, URL https://arxiv.org/abs/2410.18273.

[29] A. Aduszkiewicz, E. V. Andronov, T. Antićić, V. Babkin, M. Baszczyk, S. Bhosale, A. Blondel, M. Bogomilov, A. Brandin, A. Bravar, et al. (NA61/SHINE Collaboration), Phys. Rev. D **100**, 112001 (2019), URL https://link.aps.org/doi/10.1103/PhysRevD.100.112001.

[30] N. Abgrall, A. Aduszkiewicz, Y. Ali, E. Andronov, T. Antićić, N. Antoniou, B. Baatar, F. Bay, A. Blondel, J. Blümer, et al., The European Physical Journal C **76** (2016), ISSN 1434-6052, URL http://dx.doi.org/10.1140/epjc/s10052-016-3898-y.

[31] B. Povh, K. Rith, C. Scholz, and F. Zetsche, *Particles and nuclei: an introduction to the physical concepts; 4th ed.* (Springer, Berlin, 2004), URL https://cds.cern.ch/record/706817.

[32] J. D. Bowman, W. J. Swiatecki, and C. F. Tsang (1973), URL https://www.osti.gov/biblio/4259977.

[33] J. Wilson, J. Shinn, L. Townsend, R. Tripathi, F. Badavi, and S. Chun, Nuclear Instruments and Methods in Physics Research Section B: Beam Interactions with Materials and Atoms **94**, 95 (1994), ISSN 0168-583X, URL https://www.sciencedirect.com/science/article/pii/0168583X94956626.

[34] A. Adamczyk, R. Norman, S. Sriprisan, L. Townsend, J. Norbury, S. Blattnig, and T. Slaba, Nuclear Instruments and Methods in Physics Research Section A: Accelerators, Spectrometers, Detectors and Associated Equipment **678**, 21 (2012), ISSN 0168-9002, URL https://www.sciencedirect.com/science/article/pii/S0168900212001842.

[35] J.-J. Gaimard and K.-H. Schmidt, Nuclear Physics A **531**, 709 (1991), ISSN 0375-9474, URL https://www.sciencedirect.com/science/article/pii/037594749190748U.

[36] J. W. Wilson, L. W. Townsend, and F. F. Badavi, Radiation Research **109**, 173 (1987), ISSN 00337587, 19385404, URL http://www.jstor.org/stable/3576944.

[37] T. Yamaguchi, M. Fukuda, S. Fukuda, G. W. Fan, I. Hachiuma, M. Kanazawa, A. Kitagawa, T. Kuboki, M. Lantz, M. Mihara, et al., Phys. Rev. C **82**, 014609 (2010), URL https://link.aps.org/doi/10.1103/PhysRevC.82.014609.

[38] A. Bhagwat and Y. K. Gambhir, Phys. Rev. C **69**, 014315 (2004), URL https://link.aps.org/doi/10.1103/PhysRevC.69.014315.

[39] J. Zhao, B.-H. Sun, I. Tanihata, S. Terashima, A. Prochazka, J. Xu, L. Zhu, J. Meng, J. Su, K. Zhang, et al., Physics Letters B **847**, 138269 (2023), ISSN 0370-2693, URL https://www.sciencedirect.com/science/article/pii/S0370269323006032.

[40] H. L. Bradt and B. Peters, Phys. Rev. **77**, 54 (1950), URL https://link.aps.org/doi/10.1103/PhysRev.77.54.

[41] L. Sihver, M. Lantz, M. Takechi, A. Kohama, A. Ferrari, F. Cerutti, and T. Sato, Advances in Space Research **49**, 812 (2012), ISSN 0273-1177, URL https://www.sciencedirect.com/science/article/pii/S0273117711007897.

[42] R. Tripathi, F. A. Cucinotta, and J. W. Wilson, Nuclear Instruments and Methods in Physics Research Section B: Beam Interactions with Materials and Atoms **117**, 347 (1996), ISSN 0168-583X, URL https://www.sciencedirect.com/science/article/pii/0168583X9600331X.

[43] V. Andersen, F. Ballarini, G. Battistoni, M. Campanella, M. Carboni, F. Cerutti, A. Empl, A. Fassò, A. Ferrari, E. Gadioli, et al., Advances in Space Research **34**, 1302 (2004), ISSN 0273-1177, space Life Sciences: Radiation Risk Assessment and Radiation Measurements in Low Earth Orbit, URL https://www.sciencedirect.com/science/article/pii/S0273117704002054.

[44] M. Takechi, M. Fukuda, M. Mihara, K. Tanaka, T. Chinda, T. Matsumasa, M. Nishimoto, R. Matsumiya, Y. Nakashima, H. Matsubara, et al., Phys. Rev. C **79**, 061601 (2009), URL https://link.aps.org/doi/10.1103/PhysRevC.79.061601.

[45] *Fluka*, https://http://www.fluka.org/fluka.php?id=about&mm2=1, accessed: 2024-07-22.

[46] S. Das, *A simple alternative to the crystal ball function* (2016), 1603.08591, URL https://arxiv.org/abs/1603.08591.

[47] P. Bożek, W. Broniowski, M. Rybczyński, and G. Stefanek, Computer Physics Communications **245**, 106850 (2019), ISSN 0010-4655, URL http://dx.doi.org/10.1016/j.cpc.2019.07.014.

[48] *Geant4*, https://geant4.web.cern.ch/, accessed: 2024-07-29.

[49] D. Larsen (NA61/SHINE), Universe **5**, 24 (2019), URL https://cds.cern.ch/record/2658250.

[50] A. Aduszkiewicz, M. Bajda, M. Baszczyk, W. Bryliński, J. Brzychczyk, M. Deveaux, P. Dorosz, S. Di Luise, G. Feofilov, M. Gazdzicki, et al., Eur. Phys. J. C **83**, 471 (2023), 13 pages, 21 figures, Fixed Acknowledgment, 2302.00563, URL https://cds.cern.ch/record/2856537.

[51] M. Urbaniak, Y. Balkova, S. Kowalski, S. Puławski, and K. Wójcik, Acta Physica Polonica B Proceedings Supplement **17** (2024), URL https://www.actaphys.uj.edu.pl/fulltext?series=Sup&vol=17&aid=3-A16.

[52] HAMAMATSU, *Si strip detector datasheet*, https://www.hamamatsu.com/content/dam/hamamatsu-photonics/sites/documents/99_SALES_LIBRARY/ssd/s13804_kmpd1210e.pdf, accessed: 2024-07-22.

[53] J. Zhang, B. Sun, I. Tanihata, R. Kanungo, C. Scheidenberger, S. Terashima, F. Wang, F. Ameil, J. Atkinson, Y. Ayyad, et al., Science Bulletin **69**, 1647–1652 (2024), ISSN 2095-9273, URL http://dx.doi.org/10.1016/j.scib.2024.03.051.

[54] I. Tanihata, H. Savajols, and R. Kanungo, Progress in Particle and Nuclear Physics **68**, 215 (2013), ISSN 0146-6410, URL https://www.sciencedirect.com/science/article/pii/S0146641012001081.

[55] N. technology transfer program, *Hzetrn2020*, https://software.nasa.gov/software/LAR-19979-1, accessed: 2024-07-29.

[56] J. L. Shinn, F. A. Cucinotta, R. C. Singleterry, J. W. Wilson, F. F. Badavi, G. D. Badhwa, C. Z. J. Miller, L. Heilbronn, R. K. Tripathi, M. S. Clowdsley, et al., *A radiation shielding code for spacecraft and its validation*, https://ntrs.nasa.gov/api/citations/20040086952/downloads/20040086952.pdf, accessed: 2024-07-29.